



A Daimler Truck & Volvo Group Company

---

Master thesis

---

**Influence of processing on performance and durability of a reversal tolerant anode for a Proton Exchange Membrane Fuel Cell (PEMFC)**

*December 13, 2021*

DELFT UNIVERSITY OF TECHNOLOGY  
FACULTY OF 3ME  
MATERIALS SCIENCE & ENGINEERING

*Author:*

S.J.T. Homan

*Supervisor:*

K. Aylar

*Graduation Committee:*

Dr. P. Taheri

Dr. H. Bazyar

Dr. P. Gonugunta



## Abstract

When no hydrogen is able to reach the Pt/C catalyst in the anode of an operating Proton-Exchange-Membrane Fuel Cell (PEMFC), the potentials of the cathode and anode will be reversed. During this fuel cell reversal, the potential of the anode rises and the Oxygen Evolution Reaction (OER) and Carbon Oxidation Reaction (COR) will occur. Applying an OER catalyst to the anode prevents the COR to destroy the anode. Therefore, a reversal tolerant anode (RTA) is created. In this research, the RTA was made by the introduction of an OER catalyst ( $\text{IrO}_x$  supported on  $\text{TiO}_x$ ) to the anode. Electrochemical investigations on the RTA were done with a Rotating Disc Electrode (RDE), which allowed applying potentials on the RTA that occur during fuel cell reversal. However, these potentials on an OER catalyst with a RDE set-up is known to be troublesome. This can be devoted to the formation of oxygen bubbles, which are hard to evacuate in a RDE set-up and block reactant. Therefore, a special accelerated stress test (AST) has been developed in this research to diminish the effects of oxygen bubbles. This AST was used to investigate the effects of different processing techniques on the RTA performance and durability at fuel cell reversal potentials. Pt/C and  $\text{IrO}_x/\text{TiO}_x$  particles could be differentiated into bigger and smaller particles on the micrometer scale based on different ball milling times used during processing. This was confirmed by laser diffraction measurements, which supplied information on the particle size distribution (PSD). Besides, differences in the catalyst layer structure were confirmed by a laser microscope. In the AST, it was found that the activity towards the OER was higher for smaller particles, which could be explained by the increased surface area. It was found for all samples in the AST that there was loss of OER activity and Electrochemical Surface Area (ECSA) of Pt. Impedance spectroscopy, XPS and SEM/EDS showed that these losses could highly probable be devoted to the decrease of the ionomer content. Finally, to mimic real fuel cell reversal conditions in a RDE set-up, adjusted chronopotentiometry measurements were developed and applied. It was found that the higher OER active smaller particles had a worse tolerance against fuel cell reversal than the bigger particles.

# Contents

<b>1</b>	<b>Introduction</b>	<b>1</b>
<b>2</b>	<b>Theory</b>	<b>4</b>
2.1	Components & Principles of a PEMFC . . . . .	4
2.1.1	Fuel Cell components . . . . .	5
2.1.2	Kinetics & Mechanisms . . . . .	8
2.2	Fuel Cell Reversal . . . . .	15
2.2.1	Consequences . . . . .	16
2.2.2	Mitigation strategies . . . . .	18
2.3	Platinum on carbon support . . . . .	19
2.3.1	Porosity . . . . .	20
2.3.2	Graphitic content . . . . .	21
2.3.3	Wettability . . . . .	22
2.4	OER catalyst . . . . .	23
2.4.1	OER catalysts in the anode . . . . .	24
2.4.2	Problems with Iridium Oxide . . . . .	27
2.4.3	Problems with measuring OER catalyst <i>ex situ</i> . . . . .	28
<b>3</b>	<b>Methods</b>	<b>30</b>
3.1	Rotating Disc Electrode (RDE) . . . . .	31
3.1.1	Tafel Slope . . . . .	31
3.1.2	Electrochemical Surface Area (ECSA) . . . . .	33
3.1.3	Oxygen Evolution Reaction . . . . .	34
3.1.4	Electrical Impedance Spectroscopy (EIS) . . . . .	35
3.2	Material Characterization . . . . .	37
3.2.1	Particle size . . . . .	37
3.2.2	Surface roughness . . . . .	38
3.2.3	X-Ray Photoelectron Spectroscopy . . . . .	39
3.2.4	SEM/EDS Analysis . . . . .	40
<b>4</b>	<b>Experimental</b>	<b>42</b>
4.1	Ink preparation . . . . .	42
4.2	Electrode preparation . . . . .	43
4.3	Electrochemical protocol . . . . .	44

<b>5</b>	<b>Results &amp; Discussion</b>	<b>46</b>
5.1	Begin of life characterization . . . . .	46
5.1.1	Particle Size Distribution (PSD) . . . . .	46
5.1.2	X Ray Fluorescence (XRF) . . . . .	47
5.1.3	Surface Roughness . . . . .	48
5.1.4	Electrochemical Surface Area (ECSA) . . . . .	49
5.2	Accelerated Stress Tests (AST) . . . . .	51
5.2.1	Activity . . . . .	52
5.2.2	ECSA . . . . .	55
5.2.3	EIS . . . . .	56
5.2.4	Material Characterization . . . . .	57
5.2.5	Degradation phenomenon . . . . .	59
5.3	Reversal test . . . . .	61
<b>6</b>	<b>Conclusion</b>	<b>63</b>
<b>A</b>	<b>Roughness Determination</b>	<b>64</b>
<b>B</b>	<b>EIS Fitting</b>	<b>65</b>
<b>C</b>	<b>RDE reversal test at 50 mA/cm<sup>2</sup></b>	<b>66</b>
	<b>Bibliography</b>	<b>67</b>

# List of Figures

2.1	Schematic representation of the MEA's working principle and its components . . . . .	5
2.2	A schematic overview of a PEM Fuel Cell Stack . . . . .	5
2.3	The rise of a network of hydrated regions with the amount of water adsorbed. The value of $\lambda$ reflects the total number of water molecules adsorbed per sulphonate group. . . . .	6
2.4	A schematic representation of the anode catalyst layer, where the hydrogen oxidation reaction (HOR) is taking place on a Pt/C catalyst layer . . . . .	8
2.5	A SEM image of a Pt/C catalyst layer viewed from top (A,B & C) and from the side on a membrane (D) . . . . .	8
2.6	A chemical reaction between a reactant and product with the corresponding Gibbs energies $G_r$ and $G_p$ , respectively . . . . .	9
2.7	Volcano plot of the HOR . . . . .	11
2.8	Volcano plot of the OER . . . . .	11
2.9	Overview of different proposed Oxygen Evolution Reaction mechanisms . . . . .	12
2.10	The mechanism of the Lattice Oxygen Evolution Mechanism (LOER) . . . . .	13
2.11	Reactions occurring during partial hydrogen starvation in a PEMFC . . . . .	15
2.12	Anode, cathode and cell potential over time during a cell reversal caused by complete fuel starvation . . . . .	16
2.13	The corrosion rate of Pt/C plotted against the time at which the potentials are hold . . . . .	16
2.14	I. A cross section with a HAADF-STEM, where the cathode Pt/C catalyst layer has been subjected to 1.2 V with the different times indicated and II. represent binary TEM images of the same catalyst layer, where black represents the carbon and white the pores . . . . .	17
2.15	Results of an <i>in situ</i> fuel cell reversal test, where the O <sub>2</sub> and CO <sub>2</sub> generated are plotted as a function of time the MEA is completely fuel starved a) Pt loaded Ketjen black (KB) carbon) and b) and c) are loaded additionally with the amount of IrO <sub>2</sub> indicated . . . . .	18
2.16	Structures of various carbon allotropes: a) diamond b) graphene c) graphite d) carbon nanotube e) amorphous carbon . . . . .	19
2.17	Schematic representation of the different microstructures of carbon with also an indication of the different pore sizes in the microstructures above the arrows . . . . .	20
2.18	Schematic view of carbon black versus its graphitized counter part . . . . .	21

2.19	The image on top shows an overview of the different OER catalyst materials in acidic conditions, where the vertical axis indicates the overpotentials. Below, an overview of the catalyst materials and their noble metal content compared against RuO <sub>2</sub> (red) and IrO <sub>2</sub> (blue) . . . . .	23
2.20	The anode, cathode and total cell potential in a MEA, when complete fuel starvation is occurring . . . . .	24
2.21	MEA where the upper arrow indicates the reaction under operating conditions and the lower arrow the reaction under fuel starvation with a) Pt/C anode and b) Pt/C mixed with IrO <sub>2</sub> anode . . . . .	24
2.22	Complete fuel starvation test on the right with 3 different anode design shown on the left (MEA-1, MEA-2 & MEA-3) . . . . .	25
2.23	An <i>ex situ</i> MEA reversal test with different I/C in the anode catalyst layer, the current density is kept at 0,2 A/cm <sup>2</sup> and the anode is completely starved	26
2.24	The OER reaction on IrO <sub>2</sub> schematically shown in a RTA . . . . .	26
2.25	Two possible deactivation mechanisms of IrO <sub>2</sub> during a fuel cell reversal test, where a) represents a detachment of IrO <sub>2</sub> from the carbon support and b) deactivation of IrO <sub>2</sub> by COR products . . . . .	27
2.26	<i>ex situ</i> RDE test with an IrO <sub>2</sub> , where the potential is cycled between 1.2 - 1.7 V . . . . .	29
2.27	<i>in situ</i> MEA test, which is subjected to a potential hold of 1.53 V . . . . .	29
3.1	A schematic drawing of a RDE set-up for half cell testing . . . . .	30
3.2	Tafel slope analysis executed for the OER activity during an AST . . . . .	32
3.3	A cyclic voltammetry measurement of a PEMFC catalyst on a RDE set-up cycled between 50 and 1200 mV with the yellow, red and grey areas indicating the desorption, adsorption and DLC region, respectively. . . . .	33
3.4	The transmission line model (TLM) in a region of non-faradaic processes for a porous electrode . . . . .	36
3.5	A Nyquist plot of an EoL sample of a RTA catalyst layer obtained by EIS in a RDE set-up . . . . .	36
3.6	A schematic representation of the laser diffraction meter with its components . . . . .	37
3.7	The physical meaning of Equation 3.2.1 in order to calculate R <sub>a</sub> . . . . .	39
3.8	An SEM image of BoL anode catalyst layer used in a RDE set-up, the purple squares indicate the areas used for EDX elemental analysis . . . . .	40
3.9	An EDX elemental analysis of square 3 from Figure 3.8 . . . . .	41
4.1	An image of the changeable working electrode used in this research with its components . . . . .	44
4.2	PSD differences between ultrasonicated and non-ultrasonicated particles . . . . .	44
4.3	The different lines indicate the different cycles during the initial conditioning of Pt . . . . .	45
4.4	The different lines indicate the 15 <sup>th</sup> conditioning cycle at that specific step in the AST, whereas the dots indicate the minima or maxima of the peaks . . . . .	45

5.1	Particle size distribution (D90 in $\mu\text{m}$ ) over the ball milling time for the different inks, where the light shaded colours in <b>(b)</b> refer to the standard deviations measured (data from the HOR & OER particles only inks were obtained from previous measurements by K. Aylar) . . . . .	47
5.2	The average surface roughness results from the coated catalyst layers on the working electrode . . . . .	48
5.3	Height images of the catalyst layers made from different particle sizes, the legend on the right indicates the height with the corresponding colour . . .	48
5.4	Schematic proposed explanation about the differences in ECSA obtained .	50
5.5	1 step with 10 OER cycles, where only the oxidation sweep is shown . . . .	52
5.6	ECSA development without OER stress (yellow line) and average relative ECSA (blue) . . . . .	52
5.7	OER activity measurement (10 cycles 1.2 - 1.6V) of a step (blue) and the regeneration of the activity for the next step (orange) after relaxation time and an ECSA measurement . . . . .	52
5.8	Activity measurement at 1.60 V of the indicated cycle versus each step of the AST. The dark coloured line indicates the average value, whereas the associated shaded area color indicates the standard deviation . . . . .	53
5.9	Schematic proposed explanation about increase of OER activity due to ball milling . . . . .	54
5.10	ECSA development in AST relative to its initial value, averaged over all AST's executed in this research . . . . .	55
5.11	Schematic representation of the big particle catalyst layer coating not well electrical connected (left) and well connected (right) . . . . .	56
5.12	XPS Survey of the BoL and EoL samples . . . . .	57
5.13	XPS on the regions of interest . . . . .	57
5.14	Catalyst layer where black represents the Pt/C particles, orange the OER catalyst, green the concentration of protons and the green lines the proton diffusion path and the red line indicates the path of the electrons . . . . .	61
5.15	Results of the 10 mA/cm <sup>2</sup> current hold tests with big particles (blue) and small particles (red) with the light shaded colour indicating the corresponding standard deviations measured . . . . .	62
A.1	The results of a roughness measurements obtained from the laser microscope, where the light blue squares on the picture on top indicate the segments (Seg). Seg. 1 indicates the left square and increases till Seg.9 on the right square. . . . .	64
B.1	An example of the EIS fitting based on the Transmission Line Model, this model was implemented by A. Jurjevic. The blue dots indicate the BoL sample (0c) and the green dots the EoL sample (75c). The red line indicates the fitted $R_{ion}$ and the blue line the divergence from the $R_{ion}$ . For this test a $R_{ele}$ of 4,62 $\Omega$ and 4,60 $\Omega$ was obtained for BoL and EoL, respectively. Whereas for the $R_{ion}$ 1,64 $\Omega$ and 3,7 $\Omega$ was obtained for BoL and EoL, respectively . . . . .	65

C.1 Results of the 50 mA/cm<sup>2</sup> current hold tests with big particles (blue) and small particles (red) with the light shaded colour indicating the corresponding standard deviations measured, showing the big and overlapping standard deviations measured. It contains the average for HIC and LIC, since no difference could be found between the two inks . . . . . 66

# List of Tables

5.1	XRF of Low I/C in g/L . . . . .	47
5.2	XRF of High I/C in g/L . . . . .	47
5.3	Results of all the BoL ECSA's in m <sup>2</sup> /g of the catalyst coatings . . . . .	49
5.4	Results of the Tafel Slope determinations in mV/dec, the averages shown include OER activity from cycle 2 at step 3 and step 75 of the AST . . . . .	54
5.5	Electrical ( $R_{ele}$ ) and ionic ( $R_{ion}$ ) resistance differences between the BoL and EoL catalyst layers . . . . .	56
5.6	Results of the SEM/EDS Analysis with the different ratio's between carbon (C), fluorine (F) and platinum/irridium (Pt/Ir) of the BoL and EoL samples	58

# List of Abbreviations

<i>AEM</i>	Adsorbate evolution mechanism
<i>AST</i>	Accelerated Stress Test
<i>BoL</i>	Begin of Life
<i>COR</i>	Carbon Oxidation Reaction
<i>CV</i>	Cyclic Voltammetry
<i>DFT</i>	Density-functional theory
<i>DLC</i>	Double Layer Capacitance
<i>ECSA</i>	Electrochemical surface area
<i>EIS</i>	Electrical Impedance Spectroscopy
<i>EoL</i>	End of Life
<i>FCEV</i>	Fuel Cell Electric Vehicle
<i>GDL</i>	Gas Diffusion Layer
<i>HFR</i>	High Frequency Resistance
<i>HIC</i>	High I/C, refers to 1.0 I/C in this report
<i>HOR</i>	Hydrogen Oxidation Reaction
<i>I/C</i>	Ionomer:carbon weight ratio, used to express the amount of ionomer added in the catalyst
<i>Ink</i>	The dispersion of all the catalyst materials during the processing
<i>IrO<sub>x</sub>/TiO<sub>x</sub></i>	Iridium oxide supported on titanium oxide (OER catalyst)
<i>LIC</i>	Low I/C, refers to 0.8 I/C in this report
<i>LOER</i>	Lattice oxygen evolution mechanism
<i>MEA</i>	Membrane Electrode Assembly
<i>OER</i>	Oxygen Evolution Reaction
<i>ORR</i>	Oxygen Reduction Reaction

<i>PEMFC</i>	Proton Exchange Membrane Fuel Cell
<i>PSD</i>	Particle Size Distribution
<i>Pt/C</i>	Platinum supported on carbon (HOR catalyst)
<i>RDE</i>	Rotating Disc Electrode
<i>RDS</i>	Rate Determining Step
<i>RHE</i>	Reversible Hydrogen Electrode
<i>RPM</i>	Round Per Minute
<i>RTA</i>	Reversal Tolerant Anode
<i>SEM/EDS</i>	Scanning Electron Microscope/Energy-Dispersive X-ray Spectroscopy
<i>XPS</i>	X-Ray Photoelectron Spectroscopy
<i>XRF</i>	X-Ray Fluorescence

# Chapter 1

## Introduction

The European Union (EU) has made an agreement to emit 55 % of the level of greenhouse gasses in 2030 compared to 1990 levels and has set the goal to reach zero net emission in 2050. This deal is also known as the European Green Deal and has the goal to make the EU a climate-neutral continent [1]. In order to reach this, the EU recognizes hydrogen as one of the key-factors. Hydrogen can bridge the gap where electrification has short comings, as for example in the steel, chemical industry and certain parts of the transport sector. The goal is to make a hydrogen eco-system in the EU, where hydrogen is produced, stored and used without the emission of greenhouse gasses. The production of hydrogen can be done climate-neutral by the use of water electrolysis, where water is split into hydrogen and oxygen by electricity that is gained from renewable energy (solar, wind, etc.). The hydrogen that is gained by this procedure is called "green hydrogen" and can be stored till necessary. The storage makes hydrogen an extra interesting energy carrier. Because with the storage of hydrogen, the effects of seasonal fluctuations from the production of renewable energy can be diminished and a reliable energy output can be guaranteed. When the energy is necessary, a fuel cell will be able to convert the (green) hydrogen and oxygen (air) into electricity and water. Therefore, the cycle is completed without the emission of greenhouse gasses [2].

Concerning the transport sector, Fuel Cell Electric Vehicles (FCEV) together with Battery Electric Vehicles (BEV) are the foremost candidates to replace the Internal Combustion Engine Vehicle (ICEV), which emits CO<sub>2</sub> by burning fossil fuels. In the EU, the Fuel Cells and Hydrogen Joint Undertaking (FCHJU) has made a road map and has set the goal to have 3,7 million fuel cell passenger vehicles, 500,000 light commercial fuel cell vehicles (vans) and 45,000 fuel cell trucks and busses on the road by 2030. To realize this plan 3700 hydrogen refueling stations should be installed by 2030. The concept of FCEV is especially interesting for the long distance trucks compared to battery electric vehicles (BEV). This can be explained by the short refueling time compared to BEV and the long distances that can be reached with it due to the high energy gravimetric density (kWh/kg) of hydrogen. Busses- and trucks FCEV are thought to break even before 2028 with BEV and ICEV in terms of costs of ownership per 100 km [3][4][5].

Proton-Exchange-Membrane Fuel Cell (PEMFC) is currently the most suitable and used fuel cell for automotive applications due to its high power density, low weight, quick start-up and low operating temperature [6]. At the anode side of a PEMFC hydrogen (fuel) is converted into protons and electrons by the Hydrogen Oxidation Reaction (HOR). The protons are conducted through the membrane to the cathode. The electrons produced at the anode cannot travel through the electrical isolating membrane and will therefore flow through an external circuit, where it will be used for work, to the cathode [7]. At the cathode the electrons and oxygen (air) will be reduced to water by the Oxygen Reduction Reaction (ORR). Both the HOR and ORR are catalyzed by Pt supported on carbon (Pt/C). During normal operation sufficient hydrogen is supplied. However, when the situation occurs that no hydrogen can reach the Pt/C on the anode, the cell is referred to as completely fuel starved. The PEMFC stack still tries to pull out a current, but without hydrogen available for the HOR, the potential at the anode rises and the carbon oxidation reaction (COR) and oxygen evolution reaction (OER) will be used to deliver the required current. The potential at the anode becomes higher than the cathode, which opposes the potentials at normal operation conditions. For that reason, this phenomenon is also known as fuel cell reversal. The carbon oxidation reaction (COR) causes carbon corrosion during fuel cell reversal. Carbon corrosion has huge consequences for the durability of the anode and the cell can be considered "dead" within minutes during reversal, due to complete destruction of the Pt/C catalyst layer structure [8].

The trucks manufacturer Daimler has set future goals to reach 1.2 million km over a period of 10 years and a total of 25000 hours of operating for its FCEV trucks [9]. The issue of complete fuel cell reversal and its carbon corrosion consequence at the anode is one that needs to be overcome in order to reach the future goals set for the FCEV. System control strategies can help to overcome this issue, however these will lead to a more fragile operation system, lowering the performance and still leave the catalyst layer open to carbon corrosion. Therefore, material strategies on the catalyst layer are more of interest. One option is to make the carbon more resistant against corrosion in order to increase the lifetime. Another option is to apply an Oxygen Evolution Reaction (OER) catalyst to the anode, which causes a preference towards the OER instead of the COR during complete fuel starvation. This makes the anode more resistant against fuel cell reversal. Therefore, one could say that by introducing an OER catalyst to the anode, a reversal tolerant anode (RTA) is created.

The goal of this research was to relate the processing of the RTA to its performance and durability at fuel cell reversal potentials. Many researches have done this by testing the RTA catalyst layer *in situ* [10][11][12][13][14]. However, the fuel cell is a complex system and many components are influencing one another. Because of this, it was decided to use an *ex situ* Rotating Disc Electrode (RDE) set-up, which allows to test the RTA catalyst layer only. Multiple researches have described the RDE as inadequate for testing OER catalysts at fuel cell reversal potentials, since the created oxygen is hard to remove and blocks reactant [15][16].

Therefore, it was aimed to create a protocol that allowed measuring the performance and durability of the RTA without the effects of oxygen bubble formation. When a suitable protocol could be found, it allowed to test the different processed RTA catalyst layers. During processing and before electrochemical testing, characterizations of the RTA were necessary to recognize the effects of processing on its structure. In order to test the durability, the protocol was made in a way that enough stress was put on the RTA. Additional material characterization techniques were necessary, to understand what electrochemical stress did with the RTA at fuel cell reversal potentials.

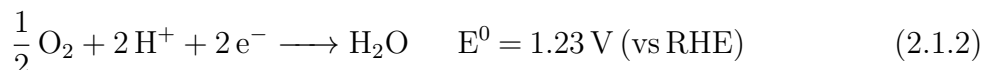
Before going into the research executed, this report will contain a theory part. First, the principles and components of the PEMFC are clarified, followed by the mechanism and kinetics of the reactions that occur during normal operation and fuel cell reversal of the RTA. Then a description of the concept of complete fuel starvation, its consequences and mitigation strategies can be found. Afterwards, a closer look is taken if the Pt/C itself can be made more resistance against corrosion. The theoretical part will end with the OER catalyst in the RTA found in other literature. After this, the research of this report will be treated. This will start with the methods used, which explain theoretical background of the measurements and how those were interpreted. This is followed by an experimental, where all the practical proceedings are elaborated. Finally, the results will be presented along with a discussion.

# Chapter 2

## Theory

### 2.1 Components & Principles of a PEMFC

During operation of a PEMFC, the Hydrogen Oxidation Reaction (HOR) takes place at the anode, which results into the formation of protons and electrons (Reaction 2.1.1). The protons flow from the anode through the proton conducting membrane towards the cathode. Whereas, the electrons created by the anode will flow through an external circuit, where it will be used for work (e.g. propulsion of the vehicle) and finally reach the cathode. At the cathode the protons, electrons and oxygen will react through the Oxygen Reduction Reaction (ORR) into water (Reaction 2.1.2). This whole process is also shown in Figure 2.1.



For fuel cells the reversible HOR is commonly used as a reference. This reference reaction can be chosen under standard conditions, where the potential is 0.0 V at all temperatures with an unit activity of 1 mol/L.s of the  $\text{H}^+$  and a pressure of 1.00 bar of  $\text{H}_2$ . This is known as the Standard Hydrogen Electrode (SHE) reference. A more convenient choice is the Reversible Hydrogen Electrode (RHE), where the HOR is measured as reference under the conditions of the measurement [17]. Since the HOR reaction is the reference, the potential of the HOR at the anode is 0.0 V and for the ORR the standard electrode potential is 1.23 V at the cathode and hence the potential of the whole cell is 1.23 V. Nevertheless, this is the case for an ideal fuel cell. In reality this cell potential will never be reached for a fuel cell. The difference between the real potential ( $E$ ) and the ideal/reversible potential ( $E_r$ ) is called the overpotential ( $\eta$ ). The concept of overpotential can be applied to an entire cell ( $\eta$ ), electrodes ( $\eta_c, \eta_a$ ) or specific processes within the cell. The overpotential of an entire cell is a buildup of the overpotentials of all the components/processes (Equation 2.1.3). It consists of the electrolyte resistance towards the proton conductivity ( $\eta_y$ ), the reaction kinetic limitations ( $\eta_k$ ), the electrical resistances of the different components ( $\eta_e$ ) and finally the concentration/mass transport losses ( $\eta_t$ ) [18].

$$\eta = \eta_y + \eta_k + \eta_e + \eta_t \quad (2.1.3)$$

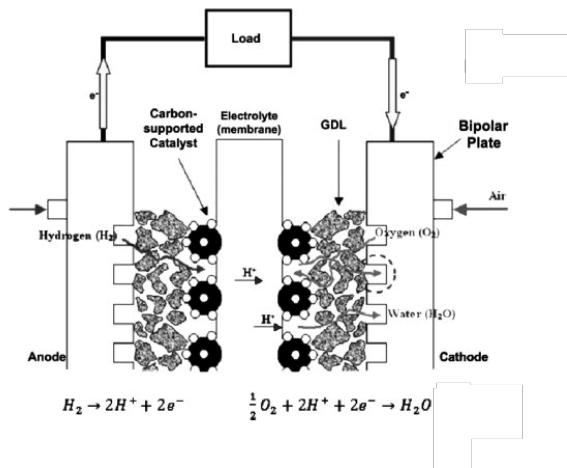


**Figure 2.1:** Schematic representation of the MEA's working principle and its components [22]

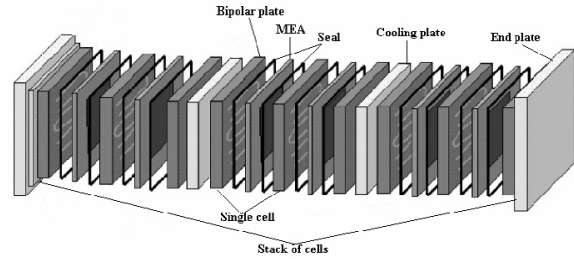


**Figure 2.2:** A schematic overview of a PEM Fuel Cell Stack [23]

An agreement for the reference conditions of PEMFC for automotive application has been made between several car companies, universities and research institutes within the European Union. It states that the reference temperature within a PEMFC in automotive applications is 80 °C. In addition, the relative humidity (RH) of the inlet gasses has to be 50 % for the fuel and 30 % for air. At the cathode, the RH for the inlet gasses is lower because there is also water produced with the ORR [19]. A range of 30 - 100 % RH within the fuel cell can be expected, where the lowest value corresponds to the start-up conditions [20]. The catalyst layer can be tested either *in situ*, where a whole membrane electrode assembly (MEA) is subjected to different tests in a fuel cell testing bench. Or *ex situ*, where a Rotating Disc Electrode is used to perform electrochemical test on the catalyst layer only. In order to mimic degradation of real life fuel cells in a short amount of time, protocols are often designed for *in situ* and *ex situ* testing. These protocols are also known as Accelerated Stress Tests (AST) [21].

### 2.1.1 Fuel Cell components

A PEM Fuel Cell stack consists of multiple single fuel cells, also known as Membrane Electrode Assembly (MEA)(see Figure 2.2). The amount and dimensions of the MEA's placed in a fuel cell stack depend on the required power output of the application. In a fuel cell stack, each MEA is separated from another by a bipolar plate. Gaskets are placed between the components to make sure the system is gas tight (sealing). In Figure 2.2 cooling plates are placed between some of the bipolar plates. However, these cooling plates can be removed from the design by integrating the cooling into the bipolar plate with additional flow channels [23][24][25]. The MEA consists of a proton conducting membrane sandwiched between an anode and cathode catalyst layer with a gas diffusion layer (GDL) attached on either sides. The working principle, components and electrochemical reactions of the MEA during operation are depicted in Figure 2.1 and are further described in the next sections.

## Bipolar plate

The bipolar plate is an essential part of the fuel cell and has several functions including distribution of the gasses to the MEA, separating MEA's in order to prevent current crossover, collecting electric current, evacuation of the water produced, humidification of the inlet gasses and cooling of the system [26]. On both sides of the bipolar plate a flow field design is applied, whereas in the middle of the bipolar plate a design is made for a liquid to cool the system. Within a cell water and protons are present, which results that bipolar plates at operation conditions are exposed to a pH of 2-3. This in combination with the elevated operating temperature (80 °C) make harsh conditions, which can cause corrosion or metal dissolution on the bipolar plate and hence loss in conductivity and performance of the fuel cell. To overcome this issue, the metal bipolar plates can be coated with a protective layer [20][23]. Since this report is focused on the fuel cell for automotive application, low weight and low volume are essential for fuel cell components. The bipolar plate is the component with the highest impact on the weight and volume of the stack [27]. Therefore, research on reducing the weight and volume of the bipolar plate is important, while maintaining high stability, high conductivity, low processing costs and secure the gas flow.

## Membrane

The most widely known membrane for the PEMFC is the Nafion membrane, which is discovered in 1966 by Dupont [6][26]. The Nafion membrane is a perfluorosulfonic acid polymer (PFSA), which consist of a polytetrafluoroethylene (PTFE or Teflon) backbone with a side chain terminated with a sulfonic acid ( $-\text{SO}_3\text{H}$ ) group. The membrane is able to absorb water due to the hydrophilic sulfonic acid groups, it can absorb 50 wt % of water compared to its dry weight. The side chains terminated with sulfonic acid are necessary to allow the conduction of protons. The sulfonic acid group of the PFSA is able to deprotonate, what results into  $-\text{SO}_3^-$ . The protons are weakly attracted to the  $-\text{SO}_3^-$ , which make them mobile through the hydrated regions in the membrane. The hydrated regions will start to connect if more water is adsorbed and eventually a proton conducting network will be formed (see Figure 2.3). This network of hydrated regions allows the protons to flow from the anode to the cathode. So the proton conductivity of the membrane will increase with the amount of water adsorbed [28].

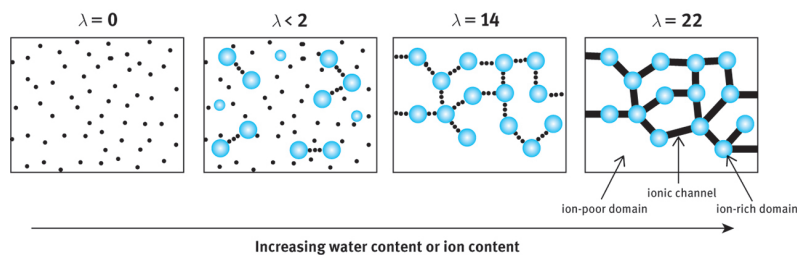


**Figure 2.3:** The rise of a network of hydrated regions with the amount of water adsorbed. The value of  $\lambda$  reflects the total number of water molecules adsorbed per sulphonate group. [28]

## Gas Diffusion Layer

The Gas Diffusion Layer (GDL) is placed between the bipolar plate and the catalyst layers. Generally, the GDL exists of a porous carbon structure, which is necessary for a good flow and distribution of the reactant gasses. Besides, it should allow transport of the electrical current between the catalyst layer and the bipolar plate. Furthermore, the GDL has an impact on water management. It should be able to remove excess water to prevent flooding at the electrode. Therefore, the porous carbon structure of the GDL is often coated with a certain amount of Teflon to obtain a more hydrophobic character [29].

## Catalyst layer

A schematic representation of a anode catalyst layer can be found in Figure 2.4, where the catalyst layer is sandwiched between the GDL and membrane. The carbon (grey) has a porous structure with Pt nanoparticles (yellow) deposited on it. A Pt/C catalyst layer in real life is shown with a SEM image from top and side in Figure 2.5. Pt is the most widely used catalyst in the cathode and anode of a PEMFC. If the Pt nanoparticles are smaller less volume and mass of Pt would be necessary to achieve the same total area of the particles. Meaning that less Pt can be used for the same electrochemical performance. This is desirable because Pt is an expensive rare earth element, which causes the catalyst layer to have the highest impact on the costs of a stack. On the cathode side more Pt is used on average than on the anode side, which is a results of the slower kinetics of the ORR compared to the HOR [27]. The amount of Pt used in a catalyst is generally expressed as the amount of Pt loaded on a certain area of the catalyst layer ( $\mu\text{g}/\text{cm}^2$ ). The Pt is loaded on a porous carbon structure, the porous structure is necessary in order to have as much surface available on a certain area. A higher surface area allows a better spreading of the Pt particles and therefore less chance of agglomeration of the Pt particles. The Pt/C layer is covered with a layer of ionomer, which is the same type of material (PFSA) as the membrane and hence will become proton conductive as well when water is being uptaken. This ionomer layer is necessary in order to deliver the protons resulting from the HOR on the Pt catalyst to the membrane and to deliver the protons from the membrane to the Pt surface for the ORR on the cathode. Besides, the ionomer functions also as a kind of glue, which keeps the whole structure together [30]. The electrons resulting from the HOR cannot diffuse through the electrical isolating ionomer and membrane but can travel through the electrical conducting carbon structure to the cathode.

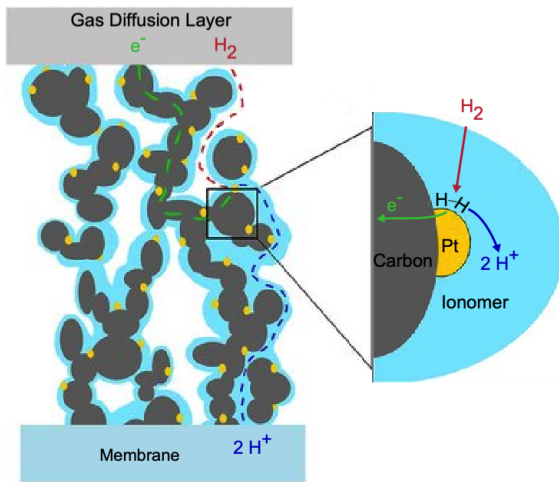


**Figure 2.4:** A schematic representation of the anode catalyst layer, where the hydrogen oxidation reaction (HOR) is taking place on a Pt/C catalyst layer [31]

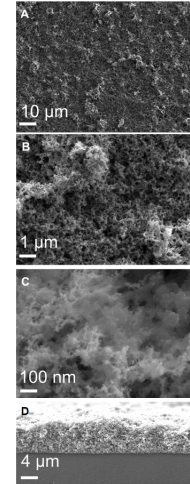
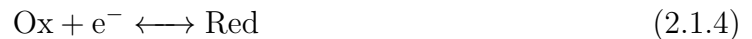


**Figure 2.5:** A SEM image of a Pt/C catalyst layer viewed from top (A,B & C) and from the side on a membrane (D) [32]

## 2.1.2 Kinetics & Mechanisms

In the next section (*2.2 Fuel Cell Reversal*) a more detailed description can be found about the electrochemical reasoning and consequences of complete fuel starvation and its impact on the fuel cell. However, this section will deal with the kinetics and mechanisms of the reactions occurring at the anode during normal operation and during complete fuel starvation (HOR, OER and COR). But first a short review about the general electrochemistry is necessary to get a good understanding of the reactions. A general electrochemical reaction between the oxidized (Ox) and reduced form (Red) can be written as shown in Reaction 2.1.4.



An electrochemical reaction can go in both directions, also known as forward and backward reaction. For each direction there is an activation barrier that needs to be overcome with an activation energy  $G_r$  and  $G_p$ , as can be seen in Figure 2.6. The probability ( $P_{act}$ ) that such an activation barrier will be overcome depends on the activation energy  $G$ , gas constant  $R$  and temperature  $T$  (see Reaction 2.1.5).

$$P_{act} = e^{-\Delta G/(RT)} \quad (2.1.5)$$

The reaction rate  $J$  ( $\text{mol s}^{-1} \text{cm}^{-2}$ ) of a reaction in a certain direction depends on the probability that the activation barrier has been overcome ( $P_{act}$ ) along with the concentration of reactant species available at the surface  $c_R^*$  ( $\text{mol cm}^{-2}$ ) and  $f$  ( $\text{s}^{-1}$ ), which is the decay rate of the product formed. The decay rate can be viewed as the possibility that the activated species (see Figure 2.6) will transform into the product instead of back to the reactant.

$$J = c_R^* f P_{act} = c_R^* f e^{-\Delta G/(RT)} \quad (2.1.6)$$

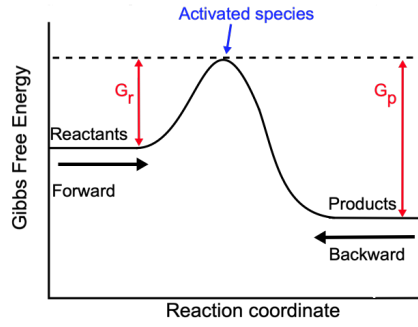


**Figure 2.6:** A chemical reaction between a reactant and product with the corresponding Gibbs energies  $G_r$  and  $G_p$ , respectively

For fuel cells, it's important to know how much current is produced by a reaction. The amount of current produced can be expressed as current density  $j$  ( $\text{A cm}^{-2}$ ), which can be calculated by multiplying the reaction rate  $J$  by Faraday's constant  $F$  (96485 C/mol) and the number of electrons transferred in the reaction  $n$ .

$$j = nFJ = nFc_R^*f e^{-\Delta G/(RT)} \quad (2.1.7)$$

At thermodynamic equilibrium should be zero net current density. This means that the current density of the forward reaction should equal the current density of the backward reaction. The value when the forward equals the backward current densities is called the exchange current density  $j_0$ . But when the energy barrier  $G$  of the forward and backward reaction is different ( $G_r \neq G_p$ ) and it is assumed that the concentration on the surface of the products  $c_p^*$  and reactants  $c_R^*$  are equal (see Equation 2.1.7). Then, the decay rate ( $f$ ) should be different for the forward and backward reaction in order to get the same current density  $j$ . This means that either the forward or backward is occurring more at equilibrium. So, the exchange current density tells something about the intrinsic kinetics of the catalyst. A higher exchange current density means that the reactions will be faster in that direction compared to a lower exchange current density.

$$j_{forward} = j_{backward} = j_0 \quad (2.1.8)$$

But out of this thermodynamic equilibrium there is a net current produced. This current produced can be expressed by using the current exchange density  $j_0$  together with two probability functions of the activation energy as can be seen in Equation 2.1.9. The first probability function ( $e^{\frac{\alpha n F \eta}{RT}}$ ) relates to the forward reaction and the other probability function ( $e^{\frac{-(1-\alpha)n F \eta}{RT}}$ ) to the backward reaction.  $\alpha$  is the transfer coefficient and depends on the symmetry of the transition state (activated species in Figure 2.6) in an electrochemical reaction and can be a value between 0 and 1, but for reactions on a metallic surface it's 0.5.  $\eta$  is the overpotential, which is in this case the difference between the voltage obtained minus the equilibrium voltage. This equation is also known as the Butler-Volmer equation [26][33][34].

$$j = j_{forward} - j_{backward} = j_0 \left( e^{\frac{\alpha n F \eta}{RT}} - e^{\frac{-(1-\alpha)n F \eta}{RT}} \right) \quad (2.1.9)$$

## Hydrogen Oxidation Reaction

The Hydrogen Oxidation Reaction (HOR) is shown in Reaction 2.1.10.



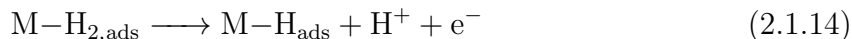
The pathway of hydrogen towards electrons and protons in an anode catalyst layer of a PEMFC is schematically shown in Figure 2.4. First, the hydrogen gas delivered from the GDL diffuses through the ionomer layer ( $\text{H}_{2,\text{sol}}$ ) and is adsorbed on the catalyst surface ( $\text{M-H}_{2,\text{ads}}$ ).



After adsorption, two routes are possible in order to get the final HOR. The first one is the Volmer-Tafel route, where the adsorbed hydrogen gas is split into two protons, which both remain adsorbed on the catalyst surface (Reaction 2.1.12). This is followed by an oxidative desorption of the protons from the surface (Reaction 2.1.13).



The HOR can also follow the Heyrovsky-Volmer route. After the hydrogen gas adsorption on the catalyst surface (Reaction 2.1.11), one proton will be adsorbed and the other proton created will be released directly along with an electron (Reaction 2.1.14). This step is also known as the oxidative adsorption. The adsorbed proton will also finally be desorped following the mechanism of Reaction 2.1.13 [26][35].



Pt group metals are well known for their catalytic abilities for the HOR and ORR. The Pt group members include Pt, Ru, Pd, Ir, Os and Rh. In order to get an idea for about the optimal HOR performance of materials a volcano plot is shown in Figure 2.7. The horizontal axis represents the enthalpy of the intermediate metal hydrogen bond (M-H) in the mechanism of HOR. The vertical axis stands for the logarithm of the exchange current density. An optimum of exchange current density can be achieved if the enthalphy of bonding is neither too high or too low. If the bonding is too strong (too high enthalpy) the desorption will limit the HOR, but if the enthalphy is too low the adsorption of hydrogen on the catalyst surface is not energetically favored. Therefore, it can be seen in Figure 2.7 that Pt will be the most suitable material for this purpose [36]. Different crystallographic structure of Pt could result towards different activity. It was found that the highest activity for Pt in acidic medium towards the HOR is (110) followed by (100) and finally (111) [37].

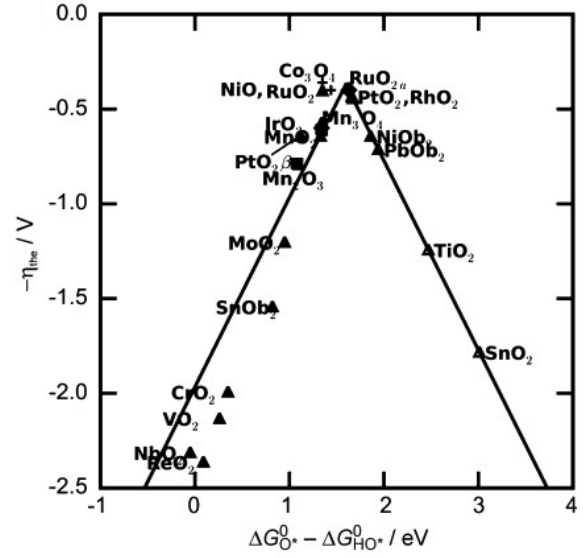
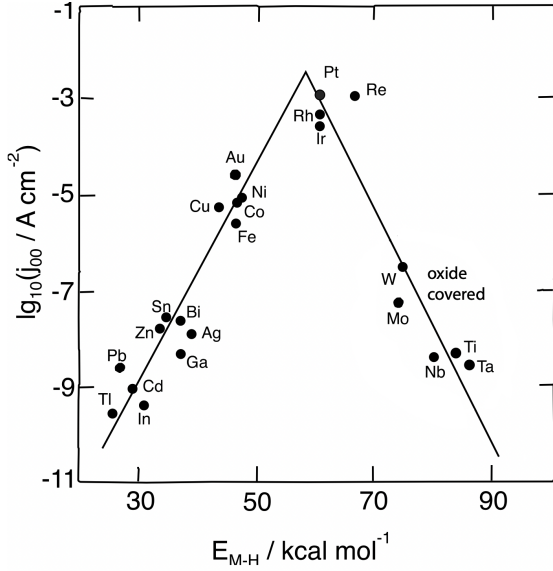


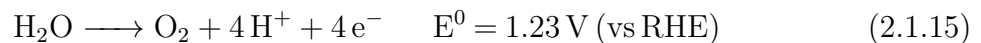
**Figure 2.7:** Volcano plot of the HOR [36]

**Figure 2.8:** Volcano plot of the OER [38]

Since, hydrogen is adsorbed and desorbed on the catalyst surface. The total amount of adsorbed and/or desorbed hydrogen correlates to the amount of active catalyst available on the surface. The amount of catalyst electrochemical available on the surface is also known as electrochemical surface area (ECSA) in  $\text{m}^2/\text{g}$ . The ECSA can be determined with a cyclic voltammetry measurement *in situ* or *ex situ*, which will be further explained in section 3.1.2 *Electrochemical Surface Area (ECSA)*.

## Oxygen Evolution Reaction

The oxygen evolution reaction (OER) (also known as water oxidation reaction) is a reaction, where water is split into oxygen, protons and electrons (Reaction 2.1.15) [39]. The reaction draws much attention because it is the anodic reaction in a PEM electrolyser, which is an electrochemical device that can be used to produce environmentally friendly hydrogen [40]. For this research, the OER is of interest because it could be used as a kind of "lightning rod" in the catalyst layer. This means that when the voltage is increasing due to fuel cell reversal, the OER can keep the potential lower so that COR will be kinetically hindered and therefore prevents the carbon corrosion degradation in the catalyst layer [8]. In this section, the plausible mechanisms of the OER will be discussed along with its kinetics.



<b>I) Oxide Path</b>	<b>II) Electrochemical Oxide Path</b>
1) $\text{H}_2\text{O} + \text{M} \rightarrow \text{M-OH} + \text{H}^+ + \text{e}^-$	1) $\text{H}_2\text{O} + \text{M} \rightarrow \text{M-OH} + \text{H}^+ + \text{e}^-$
2) $2 \text{M-OH} \rightarrow \text{M-O} + \text{M} + \text{H}_2\text{O}$	2) $\text{M-OH} \rightarrow \text{M-O} + \text{H}^+ + \text{e}^-$
3) $2 \text{M-O} \rightarrow 2 \text{M} + \text{O}_2$	3) $2 \text{M-O} \rightarrow 2 \text{M} + \text{O}_2$
<b>III) Electrochemical Metal Peroxide Path</b>	<b>IV) DFT-predicted Peroxide Path</b>
1) $\text{H}_2\text{O} + \text{M} \rightarrow \text{M-OH} + \text{H}^+ + \text{e}^-$	1) $\text{H}_2\text{O} + \text{M} \rightarrow \text{M-OH} + \text{H}^+ + \text{e}^-$
2) $2 \text{M-OH} \rightarrow \text{M-O} + \text{M} + \text{H}_2\text{O}$	2) $\text{M-OH} \rightarrow \text{M-O} + \text{H}^+ + \text{e}^-$
3) $\text{M-O} + \text{H}_2\text{O} \rightarrow \text{M-OOH} + \text{H}^+ + \text{e}^-$	3) $\text{M-O} + \text{H}_2\text{O} \rightarrow \text{M-OOH} + \text{H}^+ + \text{e}^-$
4) $2 \text{M-OOH} \rightarrow \text{M-O} + \text{H}_2\text{O} + \text{O}_2 + \text{M}$	4) $\text{M-OOH} \rightarrow \text{M} + \text{O}_2 + \text{H}^+ + \text{e}^-$

**Figure 2.9:** Overview of different proposed Oxygen Evolution Reaction mechanisms [41]

The mechanism of the OER is at the moment still in discussion and multiple suggestions have been made in literature. Reier et al (2017) has made an overview of the most promising OER mechanisms, which can be found in Figure 2.9 [41]. All the reactions, start with the adsorption of water on the catalyst surface (M) followed by other chemical processes to finally release oxygen, electrons and protons. All these mechanisms are known as adsorbate evolution mechanism (AEM). The first 3 processes (I-III in Figure 2.9) were proposed by Bockris (1956), which used Tafel Slope measurements to determine the rate determining step (RDS). The 4th mechanism in Figure 2.9 is obtained with the use of DFT by Rossmeisl et al (2005) and is one of the most recognized routes for the OER [42][43].

Each step of the reactions shown in Figure 2.9 has its own Gibbs free energy. The sum of the  $\Delta G$  of all the reaction steps equals the total  $\Delta G$  of the reaction. The step with the maximum Gibbs free energy ( $\Delta G_{max}$ ) is recognized as the potential-determining step (PDS). The overpotential of the total OER depends on the PDS as can be seen in Equation 2.1.16. In ideal conditions, the  $\Delta G$  of each step would equal the standard electrode potential of 1.23 V in order to get the total overpotential to zero of the OER [42].

$$\eta_{\text{OER}} = \frac{\Delta G_{\text{max}}}{e} - 1.23 \text{ V} \quad (2.1.16)$$

The  $\Delta G$  for each step can be very different depending on the type of catalyst but also on its surface structure. The difference in  $\Delta G$  in each step could be a result of the different properties of the intermediates. For example, if an intermediate metal oxide has a very strong bond with the -OH and -OOH groups, this intermediate will be more stable and possess a higher  $\Delta G$ . The increase of stability of the hydrophilic intermediate then also increases the chance of dissolution of the catalyst, which would decrease the catalyst lifetime [44]. Next to this, a very strong bonding with oxygen, would decrease the activity because it would be harder to form M-OOH species at step 3 of mechanism IV in Figure 2.9. But a too weakly bind oxygen would cause a decrease in activity because oxidation would occur at for example step 2 of mechanism IV in Figure 2.9. This means that for an OER catalyst an appropriate binding strength between the catalyst and the intermediate oxygen is crucial for its lifetime and activity [42]. Therefore, a parameter that includes the bonding strength of the -O and -OH ( $G_{\text{O}^*}^0 - G_{\text{HO}^*}^0$ ) could be plotted against the overpotential, which gives rise to a volcano plot of the OER as can be seen in see Figure 2.8.

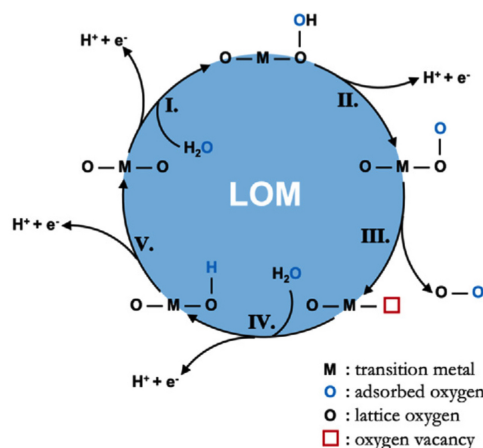


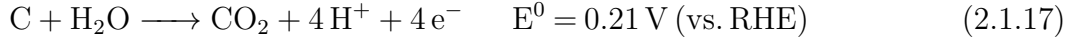
**Figure 2.10:** The mechanism of the Lattice Oxygen Evolution Mechanism (LOER) [45]

It should be noted that this Volcano plot of the OER is based on DFT calculations, but that experimental values found could differ from the predicted Volcano plot. The reason is that there are more mechanisms possible for the OER, which couldn't all be included in the DFT calculations [38]. For example, it was found that OER catalytic activity exceeds the limitation of the volcano relationship for some materials. Besides, it was found that the activity of some OER catalysts were pH dependent, which contradicts the pH independent activity of the adsorbate evolution mechanisms of Figure 2.9. An alternative mechanism explaining the shortcomings of the AEM is the lattice oxygen evolution reaction (LOER) and is shown in Figure 2.10. The main difference between the AEM and the LOER, is that for the latter the lattice oxygen of the catalyst directly participates in the oxygen evolution [46]. At the LOER, a water molecule is adsorbed on the surface lattice oxygen ( $M-O-OH_2$ ) and dissociate a proton in order to form ( $M-O-OH$ ) on its surface. After that, the second proton is dissociated, which leaves solely a bond between the original lattice oxygen and the oxygen from the initial water molecule ( $M-O-O$ ). Finally, the oxygen ( $O_2$ ) dissociates and leave a vacancy on the surface. This surface lattice will be restored due to the adsorption of water. Despite some differences between the two mechanisms, both theories are well in line that metal oxides with a more amorphous structure exhibit better catalytic activity than higher crystallized metal oxides [47]. Besides, both mechanisms include a nucleophilic attack on an oxygen (lattice or adsorbate) [42].

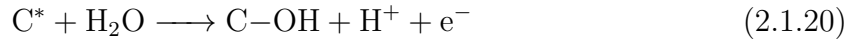
### Carbon Oxidation Reaction

There are two possible products of the carbon oxidation reaction (COR), namely carbon monoxide (CO) and carbon dioxide ( $CO_2$ ) (see Reaction 2.1.17 and 2.1.18). However, the formation of CO compared to  $CO_2$  is a factor of 10 lower, which can be explained by the higher standard potential of CO formation [48]. Besides, the standard potential of the conversion of CO to  $CO_2$  is even lower, which is a result of the easy transformation of the CO formed towards  $CO_2$  as can be seen in Reaction 2.1.19. Nevertheless, even very small fractions of CO can poison the fuel cell and result in lowering the total performance. This occurs due to Pt coverage of CO, which is a reversible process [49]. In general the

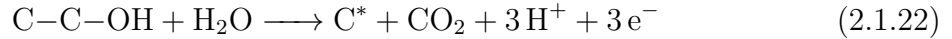
standard potentials of the COR reactions (2.1.17 & 2.1.18) are low, but the kinetics are relatively slow under PEMFC operating conditions and possess a high overpotential and almost does not occur under operating conditions [50][51].



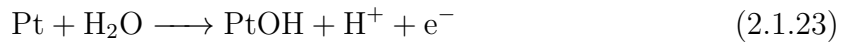
It is hard to distinguish a general mechanism for carbon corrosion in a PEMFC, because some carbon structures are more prone to corrosion than other carbon structures (see 2.3 *Platinum on carbon support*). Next to this, there are also different oxygen containing groups on the carbon surface, which results into different mechanisms of the COR [48]. However, Pandey et al (2013) has proposed a basic mechanism of the corrosion occurring at the fuel cell. First, it is assumed that the the reaction is starting at defects sites of the carbon ( $\text{C}^*$ ), where carbon and water is transformed into C-OH (2.1.20).



This hydroxyl group can be further oxidized into a ketone group (2.1.21) or at higher potential it will be oxidized to  $\text{CO}_2$  (2.1.22), which leaves defect carbon behind for another oxidization of reaction 2.1.20.



The reaction can be catalyzed due to the presence of Pt, because Pt in a water environment can be oxidized to form a hydroxyl group on it's surface (2.1.23). These OH groups on the Pt surface are thought to be spilled over to the carbon's surface (2.1.24), where reaction 2.1.22 can occur again resulting in a defect carbon ( $\text{C}^*$ ) and  $\text{CO}_2$  [52].



## 2.2 Fuel Cell Reversal

Fuel cell reversal is a phenomena caused by a wrong distribution of the inlet gasses. This means that the composition of hydrogen (fuel) to the anode and oxygen (air) to the cathode is changing. This phenomena is well known to occur when a fuel cell stack is starting up or shutting down, causing an imbalance of gasses at the electrode. In normal operating conditions there is excess fuel available at the anode for the HOR and enough oxygen is supplied to the cathode for the ORR. However, when this balance of gasses is disturbed the electrode will allow other side reactions to occur. When there is too little oxygen available for the ORR at the cathode (air starvation), the cell voltage decreases till a final cell potential of -0.1 V [53]. However, protons and electrons are still delivered from the anode through the membrane which causes the hydrogen evolution reaction (HER) at the cathode [54]. It is thought that air starvation is a result form water flooding at the cathode which decreases the diffusion of oxygen to the catalyst. This effect is expected to be more severe for a lower air stoichiometry [55][56]. However, the influence of air starvation on the durability of a PEMFC is much smaller than fuel starvation [53][55].

Fuel starvation at the anode gives rise to much higher cell potentials compared to air starvation and has carbon corrosion as consequence. Fuel starvation occurs either completely when no fuel is left or partially when there is still some hydrogen left. The two different starvation types look similar but the damage caused is on a different electrode with a different mechanism [8]. Partial fuel starvation is a result of heterogeneous fuel distribution and mostly occurs when starting-up/shutting-down the fuel cell and potentials even higher than 1.6 V can be reached at the cathode, but takes place only for a short amount of time (few seconds) [57]. Before starting up the PEMFC, the voltage is zero because both chambers of the anode and cathode are filled with air. Hence, the potential of both electrodes are equal to the open circuit voltage (OCV) and the cell voltage ( $V^C - V^A$ ) as a result will be zero. However, when hydrogen is released into the anode chamber, regions (Region A in Figure 2.11) in contact with hydrogen will lower the potential to the HOR (0.0 V vs. RHE). This causes a cell compartment voltage of 0.85 V. However, the total anode potential is maintained due to high electron conductivity. This total potential can be kept due to the available oxygen in other regions of the anode for ORR (Region B in Figure 2.11). Then, the cathode in region B tries to maintain its potential by an oxidation reaction (opposed to the ORR occuring at the anode), which it does with the available water and carbon in its environment causing a spike in voltage at the cathode. The reduction reaction in the anode and oxidation in the cathode mean that electric current and protons are flowing in the opposite direction compared to a normal operating fuel cell. Therefore, partial fuel starvation is also known as current reversal [58].

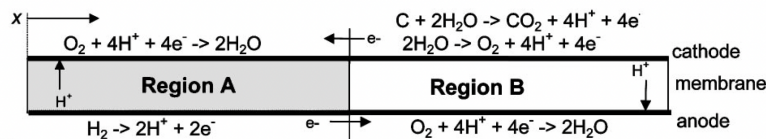


**Figure 2.11:** Reactions occurring during partial hydrogen starvation in a PEMFC [58]

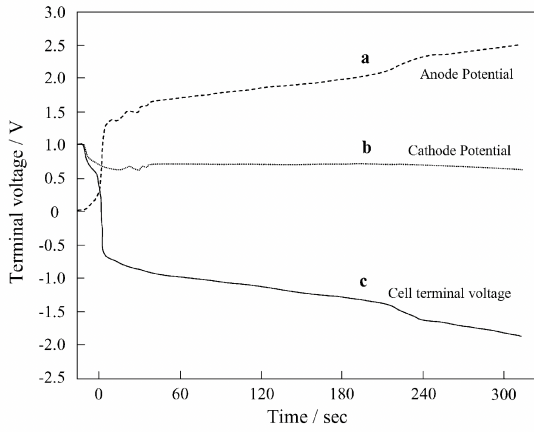


**Figure 2.12:** Anode, cathode and cell potential over time during a cell reversal caused by complete fuel starvation [61]

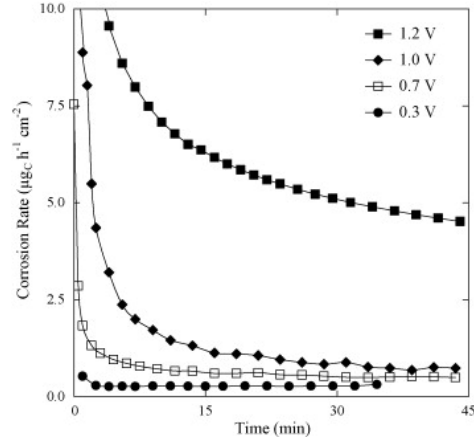


**Figure 2.13:** The corrosion rate of Pt/C plotted against the time at which the potentials are hold [62]

Opposite to partial fuel starvation and the main focus of this research is on complete fuel starvation, which causes degradation at the anode. This phenomena is caused by insufficient hydrogen, which cannot reach the catalyst due too much water or ice, which block the pores in the catalyst layer [59]. In Figure 2.12 it can be seen that the MEA at operating conditions (before  $t=0$  s) has an anode potential of 0 V and the cathode potential is equal to the cell voltage of approximately 1 V. However, when the anode fuel is completely starved (starting at  $t=0$  s) it can be seen that the potential of the anode quickly rises to approximately 1.3 V and the cathode decreases to 0.6 V. Because of this the total cell voltage become negative ( $V^C - V^A$ ) and the total potential of the cell is reversed. After the initial surge of the anode to 1.3 V the potential increases slower to a higher voltage and hence the total cell voltage decreases to a lower voltage. The fuel cell stack requires a current but without hydrogen available at the anode and a cathode that still requires protons and electrons to let the fuel cell run. The anode will start to use the water and carbon in it's environment to make the electrons and protons by either the OER or the COR [60].

### 2.2.1 Consequences

The high voltages caused by partial and complete fuel starvation cause the COR to take place, which is the responsible reaction for the corrosion of carbon in the catalyst layer. The carbon corrosion has huge consequences for the lifetime and performance of the catalyst layer. Roen et al (2004) found that carbon corrosion at a cell voltage of 0.8 V is not a real problem but starts to play a significant role in degradation at 1.1 V or higher [63]. This has been confirmed by Maass et al (2008), who obtained the different corrosion rates of a Pt/C catalyst layer at certain voltages, shown in Figure 2.13. The carbon corrosion rate was found to be higher with a higher Pt area, which could be explained by the catalytic effect of Pt on carbon corrosion described in *2.1.2 Carbon Oxidation Reaction* [62]. Next to this, the carbon corrosion rate will also be increased along with an increasing temperature and relative humidity in a PEMFC [59][62].

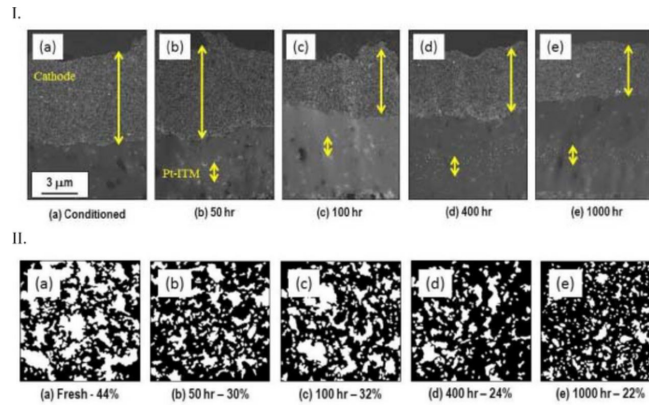


**Figure 2.14:** I. A cross section with a HAADF-STEM, where the cathode Pt/C catalyst layer has been subjected to 1.2 V with the different times indicated and II. represent binary TEM images of the same catalyst layer, where black represents the carbon and white the pores [64]

One of the foremost recognizable consequences of carbon corrosion in the catalyst layer of a PEMFC is the decrease in thickness [57][65][66]. This decrease in thickness is correlated with a collapse of the carbon backbone structure, which can be clearly seen in Figure 2.14, where a Pt/C catalyst layer is hold at a potential of 1.2 V (vs RHE) for a certain time [64]. Because of the collapsed pore structure it can be harder for the gasses to reach the catalyst and therefore increase the mass transfer losses. Next to this, decreasing the thickness of the catalyst layer can also lead to detachment from the GDL or membrane leading to increased electrical- and proton conduction resistance [65]. Another phenomena that increases the mass transfer losses during carbon corrosion is the increase of an hydrophilic character of the carbon. During corrosion, carbon gains hydrophilic oxygen-containing surface groups. Therefore, more water can be hold in the catalyst layer, which increases the diffusion resistance of the gasses towards the catalyst and the chance of flooding will also be increased [67]. Besides, the increase of the Pt nanoparticles size is also a degradation phenomena that occurs during carbon corrosion [61][64][65][67][68]. If the Pt particles are becoming bigger it will mean that there will be less electrochemical surface area (ECSA), which will lead to a decrease of performance of the PEMFC. The origin of the growth of Pt could devoted to the collapse of the structure, where different Pt particles collide against another leading to agglomeration. Besides, when Pt is dissolved it can be redeposited onto a larger particle, leading to an increase of particle size [69].

Electrochemically, carbon corrosion can be found by the carbon oxidation peaks in the CV spectrum source [62]. Other techniques to confirm carbon corrosion are titration and infrared spectroscopy, where titration requires large sample sizes and IR requires high concentration of the surface oxides. XPS remains the most popular choice for confirming carbon corrosion, where the top atom layers of the surface can be analyzed and give a view of the amount of oxide groups present. Furthermore, thermal desorption could be used that is based on the different desorption temperatures of the oxide groups that can be measured with a mass spectrometer or gas chromatography [70].

## 2.2.2 Mitigation strategies

Different mitigation strategies can be used to prevent fuel cell reversal or to protect the catalyst layer against the consequences of it. First, there are multiple options of system control mitigation strategies. There are two ways to detect fuel cell reversal in a stack. Firstly, the voltages of (individual) cells could be monitored, where a sudden rise in potential could indicate for a reversal occurring. Next to this, a sensor could be placed at the gas output and see if small fractions of  $\text{CO}_2$  can be found [71]. If reversal is detected, alternations on the current, voltage, stoichiometry and/or mass flow rate of the inlet gasses (fuel and air) are possible against the reversal. Furthermore, system control also includes the thermal and water management in a cell, which directly could influence the degree of which the fuel cell reversal is occurring and its consequences [72]. However, applying different system control strategies lead to a more fragile and expensive operation system, lowering the performance and due to its slower reaction time still leave the catalyst layer open to damage by corrosion. Therefore, a popular choice against fuel cell reversal are material mitigation strategies [59].

First, alternations on the support material (carbon) are possible in order to make the catalyst layer less susceptible against fuel cell reversal and the corrosion. In the next section (2.3 *Platinum on carbon support*), different properties of Pt/C catalyst are discussed along with the role of these properties related to fuel cell reversal. Next, the OER catalyst in the anode will be discussed (2.4 *OER catalyst*), where the addition of an OER catalyst in the catalyst layer is discussed. OER catalysts are applied in the anode to decrease the effect of complete fuel starvation. This works because the potential is kept lower due to the OER and therefore kinetically hinders the COR to occur. This effect could be seen in Figure 2.15, where the OER catalyst ( $\text{IrO}_2$ ) in the anode decreases the amount of  $\text{CO}_2$  formed and increases the  $\text{O}_2$  generation during an *in situ* fuel starvation experiment. Therefore, applying an OER catalyst in the anode layer makes the cell more resistant against complete fuel cell reversal and hence the name reversal tolerant anode (RTA) is often used [59][73][74][75].

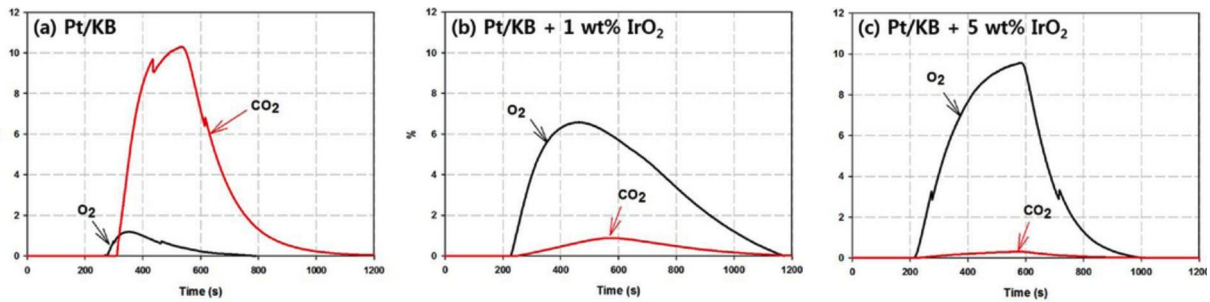


**Figure 2.15:** Results of an *in situ* fuel cell reversal test, where the  $\text{O}_2$  and  $\text{CO}_2$  generated are plotted as a function of time the MEA is completely fuel starved a) Pt loaded Ketjen black (KB) carbon) and b) and c) are loaded additionally with the amount of  $\text{IrO}_2$  indicated [68]

## 2.3 Platinum on carbon support

Carbon exists in many different forms also known as allotropes. Carbon is known to have over 500 different allotropes, which can differ by their geometry and properties [76]. Carbon can be  $sp$ ,  $sp^2$  or  $sp^3$  hybridized, where the ratio between those three determines the shape and properties. The thermodynamic most stable carbon allotrope known is diamond, which exists solely of  $sp^3$  hybridized carbon resulting in a 3D tetrahedral electrical isolating structure (see Figure 2.16a). A material that exists purely out of  $sp^2$  hybridized carbon is graphite, which is made of 2D graphene sheets stacked parallel (see Figure 2.16b,c). Because of the  $sp^2$  hybridized carbon, there is a delocalized  $\pi$ -bond, which gives rise to the good electrical conductive properties parallel to the graphene sheet. When 2 opposite edges of a graphene sheet are connected a rod shape arises, which is also known as the carbon nanotube (CNT) (see Figure 2.16 d). CNT materials possess unique conductive and mechanical properties, which can be of interest as support material for PEMFC. Furthermore, there is the amorphous carbon, which can be divided into 2 groups based on the dominance in presence of  $sp^2$  or  $sp^3$  hybridized carbon. If an amorphous carbon is not graphitizable ( $sp^3$  dominance), it is mostly known as a hard carbon. An example of an allotrope within the hard carbons class is the activated carbon, which is characteristic for its high surface area (500 - 3000  $m^2/g$ ) and high porosity. The pores of this activated carbon can take up 30-80 % of the volume [77]. However, hard carbons are not graphitizable and are therefore poor electrical conductors and less of interest for support material in the catalyst layer of a PEMFC. On the contrary, a graphitizable amorphous carbon is known as a soft carbon. This carbon will with heat treatment give rise to a more graphite-like structure. A well known group of such a graphitizable amorphous carbon is carbon black [77][78]. Carbon blacks have been the most common carbon type used in the catalyst support for PEMFC. The surface area of carbon black is typically found in the region of 50 - 1500  $m^2/g$ . It has been shown for carbon blacks with a higher surface area, a higher dispersion of Pt particle size can be reached resulting in a higher ECSA [26][79]. Carbon blacks are most commonly made by pyrolysis of hydrocarbons from aromatic residues of petroleum refiners or thermal decomposition of acetylene [33].

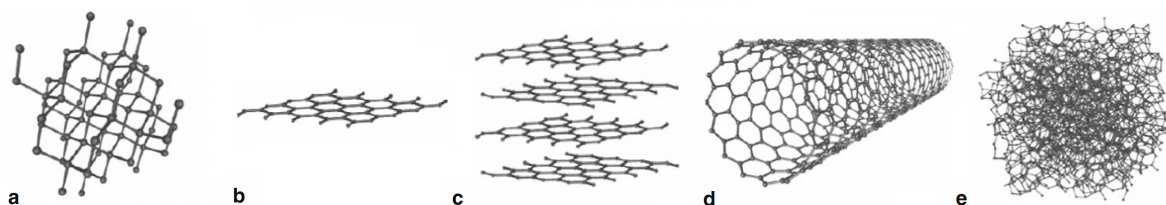


**Figure 2.16:** Structures of various carbon allotropes: a) diamond b) graphene c) graphite d) carbon nanotube e) amorphous carbon [78]

### 2.3.1 Porosity

Following IUPAC, porosity can be divided into three scales: micropores ( $< 2$  nm), mesopores (2-50 nm) and macropores ( $>50$  nm). For the fuel cell, the porosity size and shapes on the different scales have different importance for the fuel cell. In Figure 2.17, the typical different microstructures of carbon black are shown. The crystalline domain is where the graphene sheets make up the crystalline structure in the range of 10 - 20 Å. Combining these crystalline domains give rise to the primary particle (20 nm). Soboleva et al (2010) found that upon Pt deposition on carbon black the micropore volume has been reduced significantly. This could be explained by the edge sites of the crystalline domains, which are highly reactive because of the unsaturated electron density [79]. This unsaturated electron density can be devoted to the presence of oxygen containing surface groups, also known as active sites. These active sites help to prevent Pt agglomeration during carbon corrosion and initial deposition [80][81]. Castanheira et al (2016) states that these active sites in the micropores will be corroded anyway during fuel cell operating between 0.40 and 1.00 V, but that at higher potentials ( $> 1.00$  V) the graphitic domains will start to corrode leading to more active sites and more corrosion [82].

When primary particles are stacked together an agglomerate arises, which is in the range of 100-300 nm. The empty spaces in the agglomerate that are created between the primary particles are termed mesopores. Finally, when agglomerates are linked together, a chain-like aggregate structure will arise. The aggregate structure gives rise to the well connected 3D carbon structure, which is able to conduct the electrons. The voids between and within the agglomerates in the aggregate will produce the meso- and macropores in the final structure. The size and amount of meso- and macropores in the catalyst layer structure influence the transport of gasses and water management. Moreover, the pore size influences the spreading of the ionomer layer on the carbon black. It has been found that meso pores  $>20$  nm diameter allow spreading of ionomer. Therefore, the amount and sizes of the meso- and macropores are important for a desired spreading of ionomer [79]. Adjusting the aggregate sizes and the corresponding macropores have been the main focus of this research. This has been done with alternations in the processing, the effects found will be further discussed in Chapter 5.

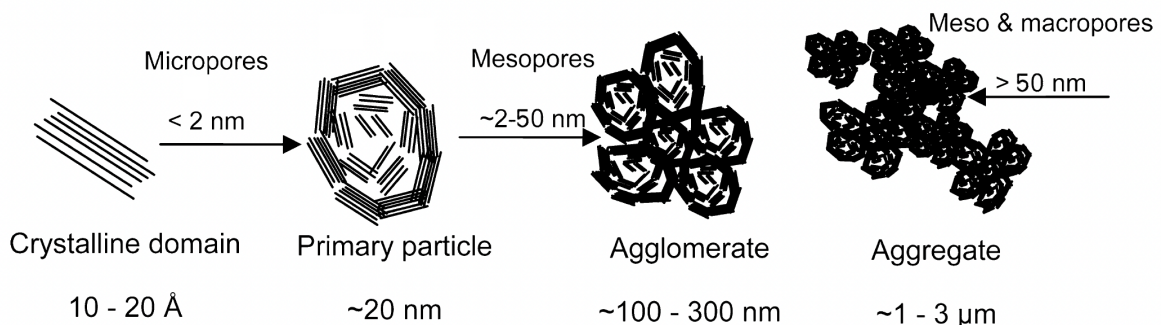


**Figure 2.17:** Schematic representation of the different microstructures of carbon with also an indication of the different pore sizes in the microstructures above the arrows [79]

### 2.3.2 Graphitic content

Cherstiouk et al (2010) found in their research that increasing the graphitic content of various carbon blacks (including Vulcan XC72 & Ketjen) increased the resistance against carbon corrosion [83]. As mentioned in 2.3.1 *Porosity*, the active sites are the edges of graphene crystalline domain ends, these active sites are also referred to as defects. Forouzandeh et al (2018) found that graphitizing the carbon reduces the density of these defects in the crystalline domain. This occurs, because the domains are growing during heat treatment, which results into a decrease of the amount of defects. This decrease of defects gives rise to a higher resistance against carbon corrosion. Because the presence of the oxygen-groups containing defects are also the points, where carbon corrosion takes place (see 2.1.2 *Carbon Oxidation Reaction*). However, also the micropores decrease upon graphitization [84]. This results in a surface area loss if the surface area of those carbons can be mainly devoted to the loss micropores. Since Pt is likely to be deposit into these active sites of the micropores (see 2.3.1 *Porosity*), it will be harder to deposit Pt and disperse it well over the surface. This is confirmed by Park et al (2016), who has showed that the non-graphitized carbon has a more dispersed Pt distribution compared to its graphitized counter part (see Figure 2.18). Also, there is less surface available for the Pt to deposit for a graphitized carbon, which also increase the chance of Pt nanoparticles to deposit on another. Therefore, Pt particles on the graphitized carbon have on average a bigger diameter resulting into a lower ECSA and during corrosion the redeposition of Pt is more likely to increase the diameter of the Pt nanoparticle [85]. However, even though the initial ECSA of graphitized carbon is lower, their resistance against carbon corrosion is in general found to be higher [65][68][85][86].

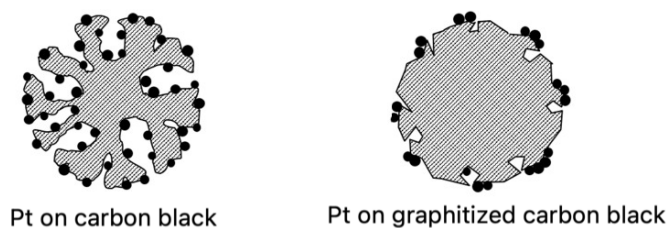


**Figure 2.18:** Schematic view of carbon black versus its graphitized counter part [85]

It was found that upon graphitizing the carbon, the surface becomes more hydrophobic (see 2.3.3 *Wettability*) and the ionomer becomes more attracted towards the hydrophilic Pt. This causes that the graphitized carbon has an harder to coat surface with ionomer compared to its non-graphitized counterpart [85]. Pantea et al (2003) found that increasing the degree of graphitization of carbon blacks increases the conductivity. Not only due to the increased amount of conductive carbon, but also due to a higher packing fraction. If the density of carbon blacks is higher, it means that there would be more chain connections of the agglomerates resulting into a higher electron conductivity [87]. However, a higher packing fraction of carbon might influence the mass transport negatively since it will be harder for the gasses to reach the catalyst. A useful way to investigate the effect of graphitization of carbon is with Raman spectroscopy and XRD [88].

### 2.3.3 Wettability

For fuel cells, it's important that the catalyst layer possess a good wettability. A too hydrophobic catalyst surface could cause a bad humidification of the ionomer and lead to loss of proton conductivity [89]. On the contrary, the carbon can neither be too hydrophilic, which can cause flooding. Flooding the catalyst layer and eventually the GDL as well will cause blockage of the pores and increase the gas transport resistance towards the catalyst and could have more fuel starvation as consequence [90]. Another aspect to keep in mind for the electrode is that on the cathode side water is produced by the ORR and on the anode side water is delivered from the membrane of the cathode side. Therefore, both sides will require a different wettability of the substrate. On the cathode side it would be preferred to have a slightly more hydrophobic character to prevent flooding. Whereas, the anode compared to the cathode would need a more hydrophilic character for its water management [91].

As mentioned before, the presence of the active sites (oxygen containing surface groups) increases the reactivity of the catalyst layer towards the COR. The surface chemistry of the carbons is directly related to the wettability of the catalyst layer, the presence of oxygen containing surface groups will increase the hydrophilic character [92]. Artyushkova et al (2012), who researched the morphology and surface properties of carbon black with Pt and their resistance against carbon corrosion, found that surface parameters indicating for a higher corrosion resistance were parameters that represent a high hydrophobicity [93]. These surface parameters include roughness, texture and compactness of the pores. The roughness could be expressed in an arithmetic average of the roughness profile ( $R_a$ ) and skewness of the roughness profile ( $R_{sk}$ ). Rougher surfaces are associated with lower contact angles, whereas lowering the contact angle is associated with increasing the hydrophilic character [94][95]. Next to this, an aspect ratio (AR) of the pores could be obtained. The AR is the ratio between the major and minor axis of an ellipse shape pore, if both the number is 1 than a spherical shape of the particle is the case. Artyuskove et al (2012) found that a high AR value (elongated pores) results in a better corrosion resistance. However, a true connection between the elongated pores and wettability of the carbon couldn't be made. Another parameter that influences the wettability is the compactness factor, which describes how compact a material is. A high compact material has narrower pores and smaller pore volume than a less compact material in the range of 20 - 50 nm. It was found that a high compact carbon black holds more water than a less compact carbon black [96]. Soboleva et al (2011) found that pores < 20 nm have a capillary effect on water and allow a better uptake of water. Besides, it was found that broader range of pore size distribution (PSD) will result into a better water retention compared to a wider range of (PSD) [89]. A straight forward way to find the influence between different catalyst layers would be with a contact angle measurement, where directly the differences between hydrophilic/hydrophobic character become clear, as done by Studebaker et al (1955) [94].

## 2.4 OER catalyst

As discussed and shown in the volcano plot in section 2.1.2 *Hydrogen Oxidation Reaction*, Pt would be the most suitable catalyst for the HOR. Next to the HOR catalyst, an OER catalyst could be applied in the anode catalyst layer as a mitigation strategy against fuel cell reversal. Because if fuel cell reversal occurs and the potential is increased ( $> 1.0$  V), a more dominant OER instead of COR could help to prevent the anode from damage [8]. The volcano plot of the OER in section 2.1.2 *Oxygen Evolution Reaction* seems to have multiple materials close or on the top of the volcano plot. This gives a bit of a wrong view, since the OER performance of the catalyst is very dependent on the conditions and the material itself. The harsh acidic conditions of the PEMFC make noble metals the best option for the OER and excludes other materials which could be used in alkaline conditions [38].  $\text{IrO}_2$  is in general recognized as the material that has the highest stability and activity towards the OER in both acidic and basic conditions [97]. Next to  $\text{IrO}_2$ , the less stable but higher active  $\text{RuO}_2$  catalyst could be used, doping  $\text{RuO}_2$  could help to overcome the stability issues [42]. An overview of OER activities in acidic conditions of different materials can be seen in Figure 2.19, where it can be observed that each material possess either Ir or Ru. Iridium, Rhuthenium and Platinum belong to Platinum-Group Metals (PGM), which are known as a scarce and expensive materials. They are divided into the same group, because of their similar physical and chemical properties. Besides, when mining these materials they tend to be found together in same mineral deposits [98]. Because of the scarcity of these materials, it is desirable to use as less as possible. Therefore, in Figure 2.19 the content of noble Ir and Ru metals are also indicated with the pure oxides in red and blue. In this research  $\text{IrO}_x$  loaded on  $\text{TiO}_x$  was used as OER catalyst. In this section the OER catalyst in the RTA described by other literature will be discussed.

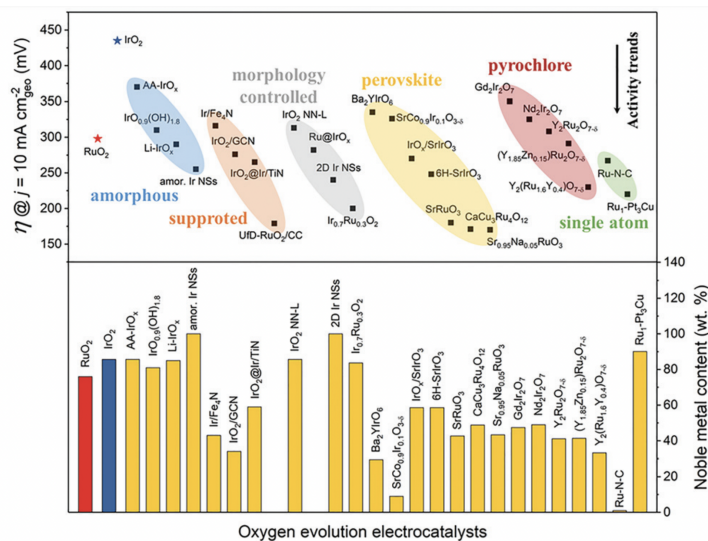


**Figure 2.19:** The image on top shows an overview of the different OER catalyst materials in acidic conditions, where the vertical axis indicates the overpotentials. Below, an overview of the catalyst materials and their noble metal content compared against  $\text{RuO}_2$  (red) and  $\text{IrO}_2$  (blue) [42]

## 2.4.1 OER catalysts in the anode

As described earlier in *2.2 Fuel Cell Reversal*, during complete fuel starvation the anode potential rises and the cathode potential stays approximately the same. This causes the total cell potential to become negative and hence it is reversed compared to normal operating conditions, as can be seen in Figure 2.20. Around a cell potential of -1.0 V the water electrolysis (OER) is the more dominant reaction and this region is called the water electrolysis plateau. After a certain time the potential will drop more and the carbon corrosion region will start, the lower the potential the more carbon corrosion will occur. Therefore, it is desired to increase the water electrolysis plateau as much as possible in order to prevent the carbon corrosion to occur. This is done by the addition of an OER catalyst [10]. The voltage reversal time is the time necessary to reach a potential at which the cell can be considered "dead" due to carbon corrosion. For the researches discussed in this section, 2.0 or 2.5 V are used as an offset for the voltage reversal time. In the reversal tests executed in this research 2.0 V was used as cutoff potential. The resistance against fuel cell reversal can be measured *ex situ* and *in situ*. *Ex situ* refers to a RDE set-up, where the catalyst layer is placed on a working electrode (see *3.1.3 Chronopotentiometry*) and the catalyst layer is required to deliver a current and the potential and time are followed to see when it reaches potential to consider the cell "dead". *In situ* refers to a test where a single cell (MEA) is placed in a testing bench and the anode is starved with hydrogen by filling it's chamber with nitrogen and the cell is still required to deliver a current, also here the potential and time are followed to obtain the voltage reversal time.

$\text{IrO}_2$  is in general recognised as the catalyst, which is the most stable with highest activity towards OER in acidic conditions [97]. One of the standard ways to apply  $\text{IrO}_2$  in the anode as a mitigation strategy is shown in Figure 2.21. Here, Pt/C particles are mixed with  $\text{IrO}_2$  particles, which is similar as done in this research. The mixing of the two catalyst results into a better resistance against fuel cell reversal compared to a test without OER catalyst. The higher the  $\text{IrO}_2$  loading, the higher the voltage reversal time observed [11].

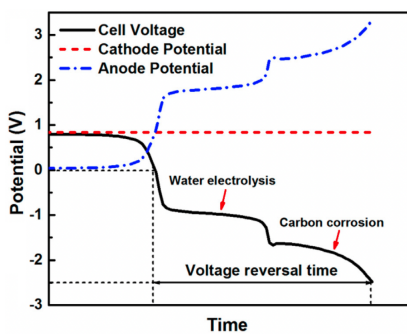


**Figure 2.20:** The anode, cathode and total cell potential in a MEA, when complete fuel starvation is occurring [10]

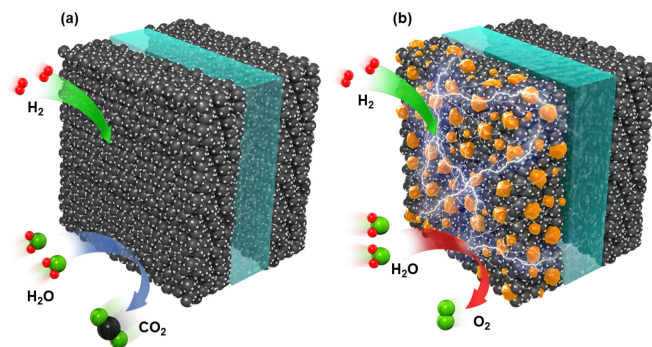


**Figure 2.21:** MEA where the upper arrow indicates the reaction under operating conditions and the lower arrow the reaction under fuel starvation with a) Pt/C anode and b) Pt/C mixed with  $\text{IrO}_2$  anode [12]

It has been found that the processing of the anode has a huge impact on the OER activity and the resistance against fuel cell reversal. First of all, the amount of OER catalyst could affect the resistance against fuel cell reversal. This could already be seen in Figure 2.15, where an increasing amount of  $\text{IrO}_2$  decreased the amount of  $\text{CO}_2$ , which was a result of the decreased COR occurrence at fuel cell reversal. A similar research was executed by Mandal et al (2018), where the Pt/C anode was loaded with 0, 5 and 50 wt %  $\text{IrO}_x$  and used for MEA testing *in situ*. It was found that the time to reach 2.0 V during a complete fuel starvation test was 2.2, 8.4 and 64.0 minutes for 0, 5 and 50 wt %, respectively. It should be noted that the initial performance of the fuel cell was the same for all three loadings and three lost the same amount of performance after the reversal test. Meaning that if the end of a reversal test has been reached with or without OER, the anode will be degraded in the same way independent of how long the voltage reversal time was. There was a linear relation found between the amount of  $\text{IrO}_2$  placed and the voltage reversal time. This is believed to happen because the  $\text{IrO}_2$  gets deactivated after a certain time, resulting that the one with absolute the most  $\text{IrO}_2$  will show the longest activity towards the OER [13]. It is not mentioned in this article where the linear relation between deactivation and amount of applied  $\text{IrO}_2$  comes from (see section 2.4.2 *Problems with Iridium Oxide*).

Where generally the OER catalyst is applied in the anode as shown in Figure 2.21, Zhou et al (2021) proved that mixing OER catalyst ( $\text{IrO}_2/\text{RuO}_2$ ) particles with Pt/C does not show the highest resistance against fuel cell reversal. This could be seen in Figure 2.22, where 3 different designs of the anode with respect toward the OER and Pt/C catalysts are used. On the right an *in situ* complete fuel starvation test is shown, where it can be seen that the design of MEA-3 showed the longest time to reach 2.0 V. This effect originates from the unequally distributed water and oxygen in a catalyst layer, which are the reactant and product of the OER. However, it should be mentioned that the initial performance of MEA-3 is slightly lower but comparable with MEA-2 and MEA-1, which could be explained by the differences in mass-transport as well [12]

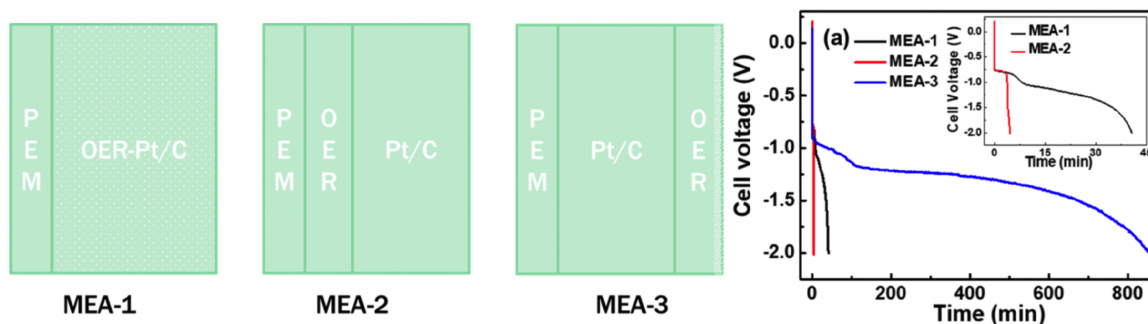


**Figure 2.22:** Complete fuel starvation test on the right with 3 different anode design shown on the left (MEA-1, MEA-2 & MEA-3) [12]

Chen et al (2021) investigated the thickness effects of the anode catalyst layer related towards the OER performance and reversal resistance. The tests with Pt/C without OER catalyst ( $\text{IrO}_2$ ) were all above 2.0 V in a minute and considered "dead". The tests with Pt/C and  $\text{IrO}_2$  loaded showed a linearly increasing reversal time versus the amount of  $\text{IrO}_2$  loaded. For the same amount of  $\text{IrO}_2$  loaded, it was found that the thinnest anode catalyst layer (2  $\mu\text{m}$ ) had a factor 6 higher reversal time (300 minutes) than the 3.5 and 6.5  $\mu\text{m}$ . The reason found for this is that the amount of ionomer is in general fixed to the weight of carbon (I/C). In order to make a thinner catalyst layer and have a similar ECSA as a thicker catalyst layer, the Pt content on carbon had to be increased. Meaning that a thinner anode has less carbon and more Pt. But, the amount of ionomer applied is fixed to the amount of carbon used (I/C ratio). This in combination that the surface of carbon doesn't scale linearly with it's weight. Results into a higher amount of ionomer available for the  $\text{IrO}_2$  catalyst, which also needs ionomer (proton conductivity) and carbon (electrical conductivity) contact points to let the OER occur as can be seen in Figure 2.24. An additional *ex situ* MEA test was executed, where only the I/C ratio was the changed parameter and it was found that indeed the highest I/C ratio had the highest reversal time, as can be seen in Figure 2.23 [10].

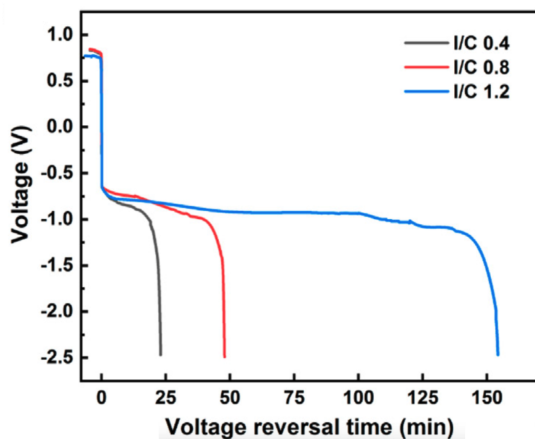


**Figure 2.23:** An *ex situ* MEA reversal test with different I/C in the anode catalyst layer, the current density is kept at 0,2  $\text{A}/\text{cm}^2$  and the anode is completely starved [10]

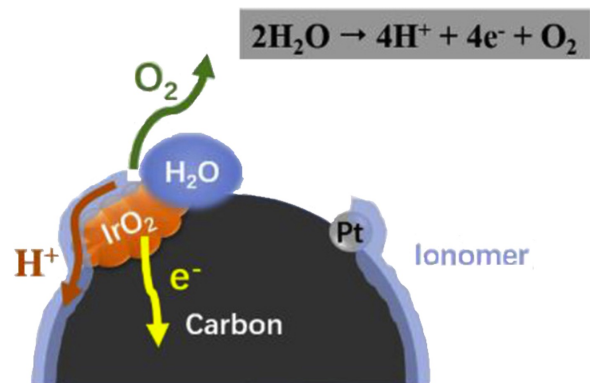


**Figure 2.24:** The OER reaction on  $\text{IrO}_2$  schematically shown in a RTA [10]

Another way of applying an OER catalyst in the anode has been done by Kim et al (2021), who made use of the fact that the defects in the carbon structure can act as anchoring centers for deposition of the catalyst. In this research, the defects in the Pt/C structure were used to deposit  $\text{IrO}_2$  particles. This has advantage that there are less defects after deposition, which are the active places where the carbon corrosion occurs (see 2.3.1 Porosity & 2.3.2 Graphitic content). Next to this, with this kind of deposition small nanoparticles of  $\text{IrO}_2$  could be achieved, which could mean an increased active area towards OER for the same amount of  $\text{IrO}_2$  used.

It was found that the carbon with initially the most defects had the highest OER activity and reversal time after IrO<sub>2</sub> deposition on the defects. But, a direct comparison with IrO<sub>2</sub> particles mixed with Pt/C particles lacks [14]. But this comparison was found in another research, Jang et al (2013) researched the difference between IrO<sub>2</sub> supported on carbon and the IrO<sub>2</sub> mixed with Pt/C particles. It was found that the IrO<sub>2</sub> supported on carbon had a higher intrinsic performance and showed better resistance against fuel cell reversal. Based on this, it could be said that IrO<sub>2</sub> loading on a support could improve the durability in fuel cell reversal compared to mixing IrO<sub>2</sub> with Pt/C particles [99].

## 2.4.2 Problems with Iridium Oxide

The aforementioned deactivation of IrO<sub>2</sub> is still unclear. But, two suggestions have been made by Joo et al (2020). The first one is the deactivation by detachment of IrO<sub>2</sub> from the carbon backbone and therefore will lose the electronic connectivity (Figure 2.25a). Second, the IrO<sub>2</sub> gets chemically deactivated by the species generated by the COR (Figure 2.25b). The IrO<sub>2</sub> was tested in a carbon support and a non-carbon support in an anode during fuel cell reversal, deactivation was only found for the IrO<sub>2</sub> in the carbon environment. Based on this it was concluded that the mechanism of deactivation of IrO<sub>2</sub> comes from carbon oxidation products [75].

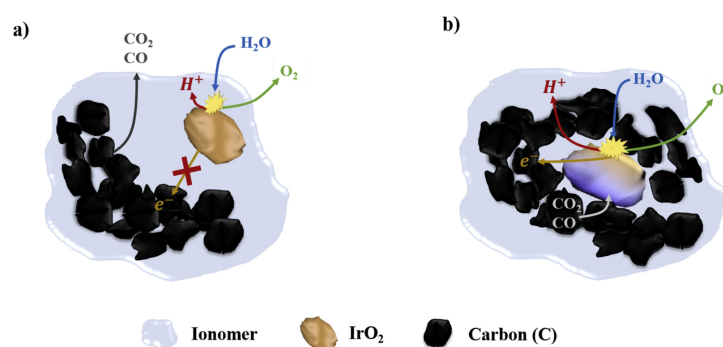


**Figure 2.25:** Two possible deactivation mechanisms of IrO<sub>2</sub> during a fuel cell reversal test, where a) represents a detachment of IrO<sub>2</sub> from the carbon support and b) deactivation of IrO<sub>2</sub> by COR products [75]

When testing an OER catalyst for a reversal tolerant anode, the focus is mainly on the behavior of the catalyst during starvation mode. However, it is just as important that the OER catalyst stays stable in the anode at operating conditions of a PEMFC. This means that the OER material should be stable at 80°C under a H<sub>2</sub> environment. It was found by Rheinlander et al (2021) that IrO<sub>x</sub> can be reduced to metallic Ir at an elevated temperature in a H<sub>2</sub> environment and the effects were researched on a PEM water electrolyser [100]. Fathi Tovini et al (2021) pointed out that this reduction can also occur in a PEMFC and has degrading consequences. First, the reduction of IrO<sub>2</sub> in a H<sub>2</sub> environment at elevated temperatures was confirmed by thermogravimetric analysis (TGA) combined with XPS and XRD. After that, starting-up/shutting-down operations were executed. It was found that when the fuel cell is operating the IrO<sub>2</sub> is reduced. This

is followed by the migration of the metallic Ir from the anode through the membrane to the cathode, where it will deposit on the cathode and lower the ORR performance. This migration of Ir occurs by the starting-up/shutting-down process. Besides, losing the IrO<sub>2</sub> on the anode side means also decreasing the reversal tolerance [101].

### 2.4.3 Problems with measuring OER catalyst *ex situ*

In the previous sections in this chapter, all the OER and durability tests discussed were performed *in situ*, which is an effective method for testing different materials because it's close to a the MEA in a real FCEV. However, a disadvantage is that many parameters could influence the outcome of a test and therefore it is hard to distract the influence of material/catalyst parameters. The *ex situ* Rotating Disc Electrode (RDE) is considered as an effective method to relatively cheap and quick gain information about the catalyst layer only. A disadvantage is that a very good and precise protocol is necessary to be in line with real life fuel cells [21]. Multiple RDE protocols for PEMFC catalyst can be found for determination of electrochemical surface area, ORR kinetics, carbon corrosion, Pt dissolution during operation on cathode, HOR resistance against CO impurities, etc. [21][102][103][104][105][106]. However, a good RDE protocol for the RTA and its stability in fuel cell reversal conditions is still lacking. One of the reasons is that OER measurements at higher potentials with a RDE setup is known to be more troublesome. The reasoning behind this is that with the OER oxygen bubbles are created, when applying potentials to mimic fuel starvation at the anode. These bubbles get stuck into the micropores of the catalyst layer and block reactant of the OER (water) to reach the catalyst. These bubbles are hard to remove by a RDE set-up. This causes that the OER activity is going down during an AST and the origin of that (actual degradation or blockage by oxygen of pores) can't be determined [107]. An example can be seen in Figure 2.26, where an AST is applied on IrO<sub>2</sub> in a RDE set-up by cycling the potential in the OER region 30 times (1.2 - 1.7 V). The OER activity is decreased at cycle 30 compared to cycle 1, this is followed by blowing Ar gas on the surface to get rid of the oxygen bubbles that are stuck in the pores of the catalyst layer. After that, the activity is increased compared to cycle 30, meaning that the decrease of OER could be devoted to oxygen bubble formation.

It can be argued that the same problem will be there for MEA in real fuel cell conditions. Fathi Tovini et al (2021) compared RDE and MEA and made the hypothesis that the MEA is less prone to bubble formation due to the thicker catalyst layer, which causes a pressure gradient through the catalyst layer and therefore the MEA can provide removal of oxygen towards the GDL. Besides, the oxygen is pulled through the membrane due to osmotic drag from the anode to the cathode. Both aforementioned phenomena are not possible at the working electrode of the RDE. However, this does not mean that this phenomena is not occurring at all in a MEA. This can be seen in Figure 2.27, where after an AST (potential hold) a relaxation time and cycling (between 0.05 and 1.2 V) has been executed, which caused the OER activity to be recovered [15].

In this research the aim was to develop an protocol (AST) in a RDE set-up, in order to

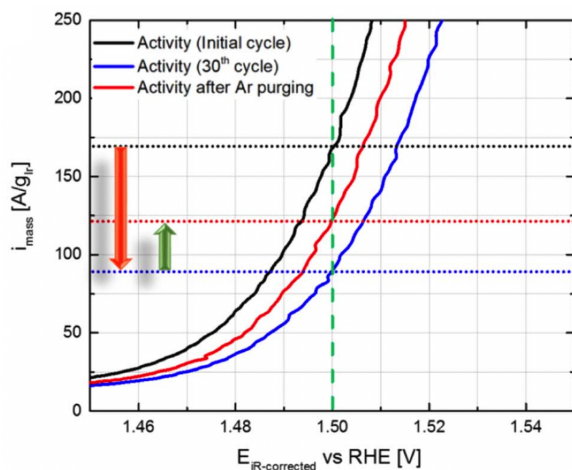


**Figure 2.26:** *ex situ* RDE test with an  $\text{IrO}_2$ , where the potential is cycled between 1.2 - 1.7 V [107]

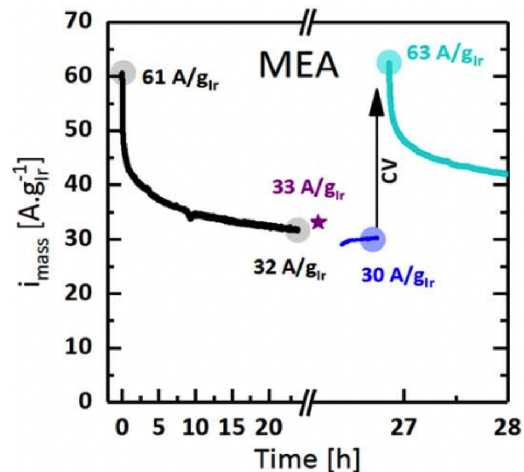


**Figure 2.27:** *in situ* MEA test, which is subjected to a potential hold of 1.53 V [15]

do relatively quick and cheap screening of the RTA catalyst layer. The AST should give information about the RTA in reversal conditions while the influence of oxygen bubbles blocking reactant is minimized. Besides, additional material characterization techniques on the RTA catalyst layer should give an idea about the its structure and degradation phenomenon going on. This should help to identify problems with the RTA catalyst layer in fuel cell reversal conditions.

# Chapter 3

## Methods

Several experimental methods in this research have been applied to investigate the influence of processing on the durability of a reversal tolerance anode of a PEMFC. First of all, laser diffraction was used to follow the particle size in the processing in order to differentiate samples. Next to this, the quality and surface roughness of the catalyst layer deposited on the working electrode was obtained with a laser microscope. The catalyst layer on the working electrode was electrochemically tested in a Rotating Disc Electrode (RDE) set-up. Additionally, material characterization techniques like XPS and SEM/EDS were used to investigate the effect of the electrochemical testing on the catalyst layer. In this chapter, the techniques used with the theoretical background behind the measurements will be explained.

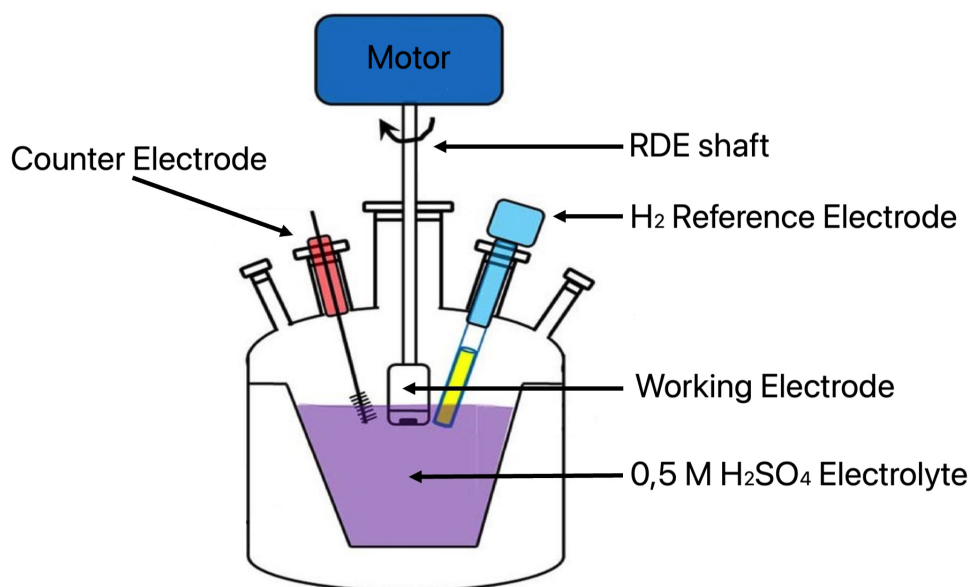


**Figure 3.1:** A schematic drawing of a RDE set-up for half cell testing [108]

## 3.1 Rotating Disc Electrode (RDE)

The RDE is a three electrode system (shown in Figure 3.1), which allows electrochemical testing on the PEM catalyst layer *ex situ*. The catalyst layer is placed on the working electrode, which is connected mechanically and electronically to a motor. The motor allows control of the rotation on the working electrode. The spinning working electrode causes a laminar flow in the electrolyte towards the working electrode's tip with the catalyst layer. This principle allows a steady-state current from the electrolyte towards the working electrode's tip [108]. Applying different rotational speeds cause different fluxes towards the working electrode's surface. For example, in ORR measurements a higher rotational speed in an oxygen saturated electrolyte will lead to more reactant per time available for the catalyst. This is due to the flux increase of the dissolved oxygen towards the tip. Whereas, in gas evolution measurements, like the OER, the rotations can be used to remove the produced gas from the surface [109]. The electrolyte has as function to conduct the protons and electrons. It can exist either as water with dissolved salt or as a diluted acid or base, since all these will deliver the positive and negative ions necessary for the conduction. However, in this research the electrolyte choice was made for sulfuric acid, in order to mimic the acidic conditions of a PEMFC. The counter electrode (a Pt wire in this research) allows the flow of charge and the circuit to be completed. When applying a potential or current on the working electrode, the counter electrode balances this to the desired current or potential by the flow of electrons [110][111]. A reference electrode is necessary to measure the current of the working electrode against. In this research the Reversible Hydrogen Electrode (RHE) was used. Specifically, a RHE Hydroflex electrode, which has an internal cartridge that allows a small amount of hydrogen to flow against a Pt wire. This allows electrochemical measurements against RHE without the need of an additional hydrogen source [112].

### 3.1.1 Tafel Slope

An analysis with the use of a Tafel plot with the corresponding Tafel equation and slope can help to get an understanding about the reaction kinetics. In the section *Kinetics & Mechanisms 2.1.2* the derivation of the Butler-Volmer has been shown. In this section the derivation of the Tafel Equation from the Butler-Volmer will be shown, with the corresponding meaning of the values used in this report.

When the overpotential becomes large, one of the terms in the Butler-Volmer equation becomes negligible (see Equation 3.1.1). For the forward (reduction) reaction, only the first term is important and the second term will become very small. Whereas, for the backward (oxidation) reaction only the second term will be of interest. This principle can be used to simplify the Butler-Volmer equation to the Tafel Equation. Since in this report Tafel analysis is only used for the OER reaction, which is an oxidation reaction, only the anodic deviation from the Butler-Volmer is shown. As mentioned before, for oxidation only the second term of the Butler-Volmer equation is of interest (3.1.2).

In order to obtain the overpotential out of the equation, a natural logarithm has to be taken (3.1.3), which can also be rewritten to a common logarithm (3.1.4). Finally, the formula can be simplified by substituting certain parts of the equation and the Tafel Equation is obtained (3.1.5). The Tafel Equation can be used to make a Tafel Plot. Where the exchange current density will be represented by the interception with the current density axis (a in 3.1.5). Besides, the slope of the linear part of the Tafel Plot can be used to observe how the kinetics are (b in 3.1.5). If the Tafel Slope is higher, the reaction kinetics will be slower [26][33][34].

$$j = j_{forward} - j_{backward} = j_0 \left( e^{\frac{\alpha n F \eta}{RT}} - e^{\frac{-(1-\alpha) n F \eta}{RT}} \right) \quad (3.1.1)$$

$$j = j_0 \left( -e^{\frac{(1-\alpha) n F \eta}{RT}} \right) \quad (3.1.2)$$

$$\eta = -\frac{RT}{(1-\alpha)nF} \ln(j_0) + \frac{RT}{(1-\alpha)nF} \ln(-j) \quad (3.1.3)$$

$$\eta = -\frac{2.303RT}{(1-\alpha)nF} \log(j_0) + \frac{2.303RT}{(1-\alpha)nF} \log(-j) \quad (3.1.4)$$

$$\eta = -a + b * \log(-j) \quad (3.1.5)$$

An example how the Tafel Slope was gained in this report can be seen in Figure 3.2. The different graphs indicate the different sweeps in the AST where the Tafel analysis was executed on. All the graphs are fitted with an equation in the region where the graphs are linear, which is represented by the dark shaded line in Figure 3.2. The corresponding formula is then obtained and is shown in the legend. If this formula is compared with Equation 3.1.5, it can be seen that the value of the Tafel Slope (in V/dec) is given by the value before x in the fitted equations ( $y = \dots x + \dots$ ) in Figure 3.2. This is because the x-axis of Figure 3.2 is given in log current density, which is similar as  $\log(-j)$  in Equation 3.1.5.

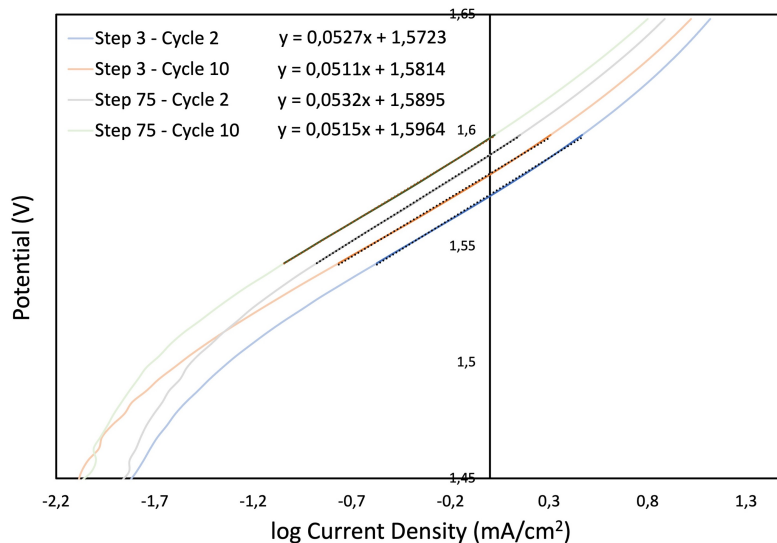


**Figure 3.2:** Tafel slope analysis executed for the OER activity during an AST

### 3.1.2 Electrochemical Surface Area (ECSA)

A cyclic voltammetry (CV) measurement was performed by swiping back and forth between two potential limits. The obtained current is plotted against the potential and gives rise to the CV curve. A CV curve of a Pt/C catalyst in a RDE set-up can be found in Figure 3.3. If the voltage is swept from a lower towards a higher potential it is called the oxidative scan (upper part Figure 3.3), when reversed it is named the reductive scan (lower part Figure 3.3). The yellow part in Figure 3.3 during the oxidation sweep can be labeled as the desorption region, because here protons are desorped on the Pt. This is contrary to the red region in Figure 3.3, here protons are adsorped on the Pt during the reduction scan. Therefore, this region is also known as the adsorption region. So, the integral of one of these two regions is proportional to the amount of protons adsorped or desorped. This directly relates to the amount of Pt available on the surface for electrode reactions.

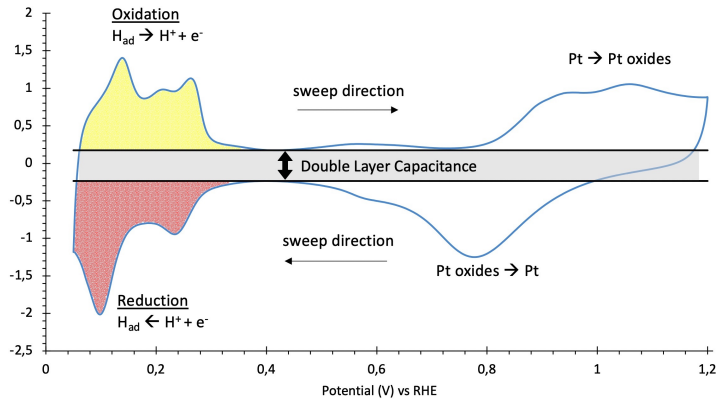


**Figure 3.3:** A cyclic voltammetry measurement of a PEMFC catalyst on a RDE set-up cycled between 50 and 1200 mV with the yellow, red and grey areas indicating the desorption, adsorption and DLC region, respectively.

In this research, the hydrogen adsorption and desorption peaks of Pt are both used for determination of the ECSA. The formula of the total charge involved in the desorption ( $Q_{des}$  in C) and adsorption ( $Q_{ads}$  in C) can be seen in Equation 3.1.6, where  $I$  (A) is the current,  $v$  is the sweep rate (V/s) and  $U$  is the potential (V) window used. The lower limit should not be lower than 50 mV, because this is the part where hydrogen evolution ( $H_2$  gas formation) occurs. The upper voltage limit has been chosen when the current reaches the region of non-Faradaic proces, also known as the Double Layer Capacitance (DLC) as shown in Figure 3.3. This area of the DLC region should not be included into the determination of  $Q_{des}$  and  $Q_{ads}$ .

$$Q_{des} \text{ or } Q_{ads} = \int I \cdot dt = \frac{1}{v} \int U \quad (3.1.6)$$

$$ECSA = \frac{\frac{1}{2} \cdot (Q_{des} + Q_{ads})}{2,1 \cdot L \cdot A \cdot 0,77} \quad (3.1.7)$$

The integrals of the desorption ( $Q_{des}$ ) and adsorption ( $Q_{ads}$ ) can be used in Equation 3.1.7 to calculate the final ECSA ( $\text{m}^2/\text{g}$ ), where 2.1 is the charge required to oxidize one monolayer of hydrogen on a polycrystalline Pt in C/m. L refers to the Pt loading in the catalyst layer in ( $\text{g}/\text{m}^2$ ) and A the evaluated area of the catalyst layer ( $\text{m}^2$ ). Next to this, a correction factor is applied of 0,77 because the active area corresponds to 77 % of the actual existing area [113][114][115][116].

### 3.1.3 Oxygen Evolution Reaction

#### Activity Measurement

During fuel cell reversal the stack tries to pull a current out of a fuel starved cell. An higher OER activity of the catalyst could potentially mean that a lower potential could be hold when fuel cell reversal occurs. The activity of the OER can be monitored by looking to the current density at a certain potential. In section 2.1.2 *Kinetics & Mechanisms* the derivation of the current density ( $j$  in  $\text{A}/\text{cm}^2$ ) has been described. The current density is also used as a measurement for the activity of the catalysts tested in this report. When the potential is cycled in the OER region a current generated due to the OER can be found. The value of the current obtained can be divided by the area of the working electrode, which gives the current density. Obtaining the current density at a certain voltage and comparing this value with other processed catalysts can give a good idea about the catalyst performance. Whereas following the current density during an AST will give a good view about the catalyst's stability. Next to the current density, the mass activity could be a possibility to represent the activity of a catalyst (in  $\text{A}/\text{g}_{catalyst}$ ), where the amount of current generated is given against the amount of catalyst loaded [117]. Since in this report all the catalyst loadings were the same, the current density represented in this report is in exact line with the mass activity.

#### Chronopotentiometry

To mimic real life fuel cell reversal of a PEMFC, chronopotentiometry could be applied in a RDE set-up. In chronopotentiometry a certain current is applied to the catalyst layer and the potential is followed over time. This is very similar to a fuel starved anode, where the fuel cell stack tries to pull out a current of the MEA as shown in Figure 2.20. By using a certain cut-off potential (e.g. 2 V), a reversal time could be obtained in the RDE set-up for that catalyst layer. As mentioned, in 2.4.3 *Problems with measuring OER catalyst ex situ* there is quite a big discrepancy between the catalyst layer *ex situ* versus *in situ*. Nevertheless, comparing *ex situ* chronopotentiometry results of different catalysts all tested in a RDE set-up could give some fundamental insights related to the reversal tolerance of the catalyst layer.

### 3.1.4 Electrical Impedance Spectroscopy (EIS)

Electrical impedance ( $Z$ ) can be seen as the resistance of an alternative current through a conductive material. With the results of electrical impedance spectroscopy (EIS) and fitting this in an electrical circuit model, information could be obtained on the electrical properties of different components [118]. For an EIS measurement, the potential of the working electrode was alternated around a defined amplitude with a certain frequency compared to the reference electrode. This will result into a sinus movement of the applied voltage, which can be described with the Equation 3.1.8. The response of the cell will be an alternative current ( $I_t$ ), which is a sinus movement as well but slightly shifted compared to the applied potential with a phase ( $\Phi$ ). The impedance ( $Z$ ) is the ratio of excitation voltage and responsive current (see Equation 3.1.9) [119].

$$E_t = E_0 \sin(\omega t) \quad (3.1.8)$$

$$Z_{total} = \frac{E_t}{I_t} = \frac{E_0 \sin(\omega t)}{I_0 \sin(\omega t + \Phi)} = Z_0 \frac{\sin(\omega t)}{\sin(\omega t + \Phi)} \quad (3.1.9)$$

If the sinus wave function of the applied voltage ( $E_t$ ) is plotted on the x-axis and the current obtained ( $I_t$ ) on the y-axis an oval shape will result in where the two waves meet. This oval shape can be expressed in complex numbers with Euler's relationship. This means that if the impedance is expressed in complex numbers, an imaginary part ( $Z_{img}$ ) can be distinguished. A Nyquist plot can be obtained if the imaginary part ( $Z_{img}$ ) of the impedance is plotted against the real part ( $Z_{real}$ ). Different phenomena can be observed based on the frequencies applied and the models used for interpreting those. If the model is well, it overlaps precisely with the the Nyquist plot. This gives then information about the resistances in the catalyst layer [119].

In this research the Transmission Line Model (TLM) has been used to analyze the resistances occurring in the PEMFC anode catalyst layer in a RDE set-up. A representation of the TLM can be found in Figure 3.4, where the electrical resistance of the catalyst layer itself ( $R_{ele}$ ) can be set to zero. This can be done because the electrical resistances can be considered negligible in the carbon of the catalyst layer compared to the ionic resistance ( $R_{ion}$ ). The ionic resistance can be seen as the resistance of the ion transport ( $H^+$ ) in the porous electrode. The abbreviation HFR in Figure 3.4 stands for High-Frequency Resistance. Besides, it was important that the EIS tests were measured in the non-faradaic (400 mV) region in order to prevent other electrochemical reactions influencing the impedance results [120].

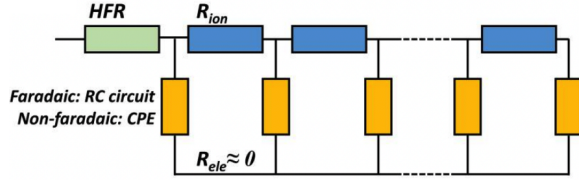


**Figure 3.4:** The transmission line model (TLM) in a region of non-faradaic processes for a porous electrode [121]

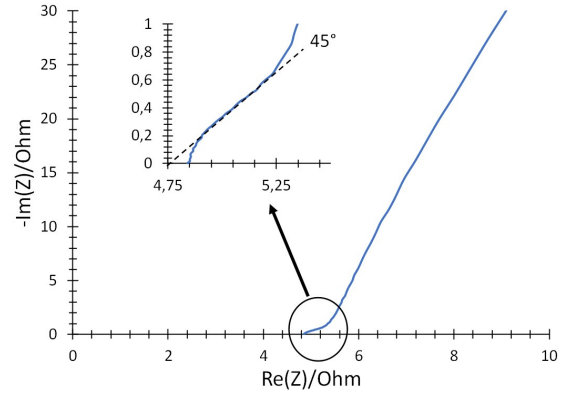


**Figure 3.5:** A Nyquist plot of an EoL sample of a RTA catalyst layer obtained by EIS in a RDE set-up

In this research, like the one in Kwon et al (2021), the constant phase element (CPE) was used for fitting and to derive Equation 3.1.10 for the PEMFC catalyst layer [121]. Based on this, the impedance of a porous electrode should follow a 45° line as shown in Figure 3.5 followed by a divergence of the imaginary impedance ( $Z_{img}$ ). Equation 3.1.10 describes the relation between the length of the graph following the 45° line ( $L$ ), the ionic resistance  $R_{ion}$  and two impedances obtained ( $Z_{real}$  and  $Z_{img}$ ). Normally, this equation would also include the  $R_{ele}$ , but as mentioned before  $R_{ele}$  can be considered zero due to the high conductivity. However, the  $R_{ele}$  of all the elements present in a RDE set-up can be obtained by looking to the value  $Z_{real}$  when the graph crosses the X-axis of the Nyquist plot [122].

$$Z_{real} = \frac{R_{ion} \cdot L}{3} \cdot Z_{img} \quad (3.1.10)$$

## 3.2 Material Characterization

### 3.2.1 Particle size

The particle size distribution (PSD) of a dispersion can be determined with a laser diffraction meter. For this research it was useful to obtain the PSD of the RTA during processing. This was done because the influence of particle size in the anode catalyst layer on reversal tolerance was researched. When the PSD had to be checked, a sample of RTA dispersion (ink) was taken out during the processing and was diluted with solvent. These diluted inks were placed in the laser diffraction meter to determine the particle sizes.

A laser diffraction meter is shown schematically in Figure 3.6 and consists of a sample holder in which the sample is placed. A laser light beam is focused on the sample, which is surrounded by detectors. The light will be scattered upon interaction with the particles. Smaller particles scatter the incident laser beam at higher angles and bigger particles at lower angles [123]. Since the sample is surrounded by detectors, the angles of the scattered light could be determined [124]. The detected angle of the scattered light and its intensity correlate to the particle size and its presence in the dispersion. Using this principle in combination with the Mie and Fraunhofer theory will result into an establishment of the PSD. The Mie theory gives a solution for light scattering by homogeneous sphere by including all types of light interaction. This requires a lot of data about the optical properties of the particle, the medium and the interactions of both. This can very be hard to determine, because it depends on many parameters (e.g. surface roughness, crystal structure, wavelength of light, etc.). Without all the optical parameters, the parameters could be manipulated in order to fit the theory with the obtained data, which is still very insight full for the PSD. However, when used with all defined optical parameters, it gives a very precise and true answer. The shortcomings of the Mie theory can be omitted by using the Fraunhofer theory. This theory assumes particles as two dimensional discs, only takes the interactions at the contour of a particle into account and only the scattering in the forward direction is considered [125].

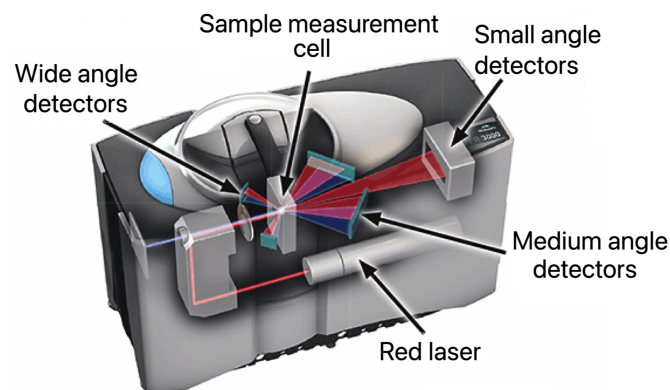


**Figure 3.6:** A schematic representation of the laser diffraction meter with its components [124]

When a scattering spectrum is obtained, the computer uses both theories to fit the spectrum as good as possible to give a PSD. For particles with the size 10 times bigger than the wavelength of light of the incident beam the Fraunhofer theory is more valid. Where smaller than this value, the Mie theory is more assumable [126]. Since, in this research the PSD was in the range of 1 - 5  $\mu\text{m}$  and infrared light was used, it's more likely that the Mie theory have been used more dominantly. Besides, it should be noted that scattered light can scatter again with other particles giving a wrong image of the scattered angle. Therefore, it is important to repeat many scans to diminish this effect [125]

### 3.2.2 Surface roughness

A Keyence laser microscope was used in this research to evaluate the surface roughness of the RTA catalyst layer on the working electrode. This was executed by the principal of Confocal Laser Scanning Microscopy (CLSM). Confocal means that the scanning for the image is done in the focal plane only. Compared to electron microscopes (see 3.2.4 *SEM/EDS Analysis*), the CLSM has less resolution but it can be used quickly without the need of extensive sample preparation and 3D imaging quality is comparable [127].

The working principle is based on a laser beam, which is emitted from the light source towards the surface of the sample. The reflected laser passes through a half mirror to the receiver. The intensity of the reflected laser is stored with the corresponding X and Y coordinates. This will be saved as an intensity image at that height. Afterwards, the Z-axis (distance between microscope and sample) is slightly alternated, followed by making another intensity image with the corresponding X and Y coordinates. Making a lot of these images over the Z-axis and combing this data can give a very detailed height profile [128]. With the use of the of an height profile, a surface roughness profile could be obtained. Roughness can be defined as a surface parameter that describes the unevenness of the surface [129]. In this report the surface roughness is of interest because it can be used as an indicator for the effect of particle sizes in the ink dispersion on the eventual deposited catalyst layers on the working electrode. Different parameters can be used to quantify the surface roughness. In this report the choice has been made to compare the differences in average roughness ( $R_a$ ).  $R_a$  is a single value of the average roughness and it's physical meaning can be seen in Figure 3.7 and in Equation 3.2.1. The || was used to treat all values as positive compared to the mid line. Besides,  $z(x)$  indicates the height of point x and  $l_r$  the length used for sampling [130]. In this research a height profile with a surface of 500 x 5000  $\mu\text{m}$  was made along the diameter of the catalyst layer coating on the working electrode. This allowed extraction of surface parameters and comparison of the coatings. An example of a height profile with the images and roughness parameters from the RTA catalyst layer on a working electrode is shown in Appendix A.

$$R_a = \frac{1}{l_r} \int_0^{l_r} |z(x)| dx \quad (3.2.1)$$

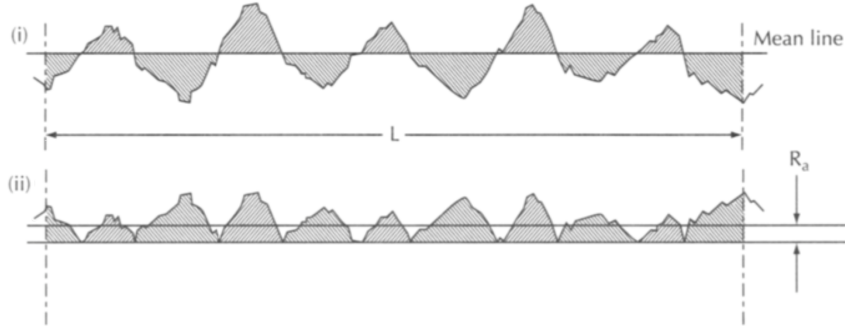


**Figure 3.7:** The physical meaning of Equation 3.2.1 in order to calculate  $R_a$  [130]

### 3.2.3 X-Ray Photoelectron Spectroscopy

X-Ray Photoelectron Spectroscopy (XPS) is a technique used for the investigation of chemical composition of a surface. XPS can be used qualitatively, where the type of bonding or oxidation states of the elements can be investigated. Besides, XPS can be used quantitatively, where the amount of the different elements on a surface with a certain type of bonding or oxidation state can be distinguished. The penetration depth of the XPS can be up to 10 nm, therefore the characterization is a sensitive surface analysis technique [131].

A sample is irradiated with X-Rays, which are generated in this research from an Al source. The electrons interact with the surface atoms by a formula that can be seen in Equation 3.2.2. Where  $h\nu$  relates to the energy from the photon,  $\phi_s$  to the work function of the spectrometer itself and  $BE$  is the binding energy of the atomic orbitals from the atoms on the surface. The binding energy can be viewed as the energy difference between initial and final state after the emission of the photo electron. This allows specific identification of elements, because the atomic orbitals of an element will be different based on the type of element, bonding, oxidation state, etc. For a XPS spectrum, the x-axis contains the binding energy and the y-axis the counts (amount of electrons received per time unit). Since the binding energy is very specific for the element, shifts and the place on the x-axis can be used to determine the element and its bonding. The integral ( $I$ ) of the peak, directly relates to the amount of that certain element in that state present. Because if there is more of a certain element on a surface, a higher amount of electrons with that specific binding energy will be detected and result into a higher peak. Next to this, to calculate the different ratios of the atomic elements the sensitivity factor ( $S$ ) should be taken into account, as can be seen in Equation 3.2.3.  $n$  is the number of atoms/cm<sup>3</sup> and  $S$  is a known value and depends on the angle between the analyser and x-ray source, which was for this research 54.7°[132].

$$KE = h\nu - BE - \phi_s \quad (3.2.2)$$

$$\frac{n_1}{n_2} = \frac{I_1/S_1}{I_2/S_2} \quad (3.2.3)$$

### 3.2.4 SEM/EDS Analysis

Scanning Electron Microscope-Energy-Dispersive X-ray spectroscopy (SEM/EDS) is a machine that consists of a electron microscope (SEM) with an additional detector for chemical composition analysis (EDS). An electron beam is created in the electron gun with a certain energy. Through apertures, lenses and a deflection coil the beam is focused on the sample. At the sample the incoming primary electrons will interact with atoms of the sample, which will reflect the electrons through elastic and inelastic collisions. These surface interactions will give rise to back-scattered electrons, secondary electrons and X-Rays. The back-scattered electrons have an elastic collision with the atoms, therefore they have comparable energy as the incoming primary electron. Secondary electrons are a result of inelastic collisions of the primary electrons. This means that when colliding with the atom, the atom can uptake the energy to become ionized, which will lower the energy of reflecting secondary electron. When relaxation of the atom occurs, the atoms can release their energy as X-Rays or Auger-electrons.

In order to obtain an image, all SEM are equipped with detectors for back-scattered electrons (high energy) and secondary electrons (low energy). Additionally, the SEM used in this research also had an additional detector for X-Rays. The X-Rays can be detected either wave-dispersive or energy-dispersive. For this research the Energy-Dispersive X-Rays (EDS) detector was used, because this one allows to measure the photon intensity as a function of their energy, which can be used to analyse the chemical composition quantitatively and qualitatively [133][134].

An example of a SEM image can be seen in Figure 3.8 with the corresponding EDX in Figure 3.9. The microscope was zoomed in on the catalyst layer, where different area's were chosen to do an elemental analysis on. The results of an EDX were obtained in percentages of the atomic presence graph (see Figure 3.9)

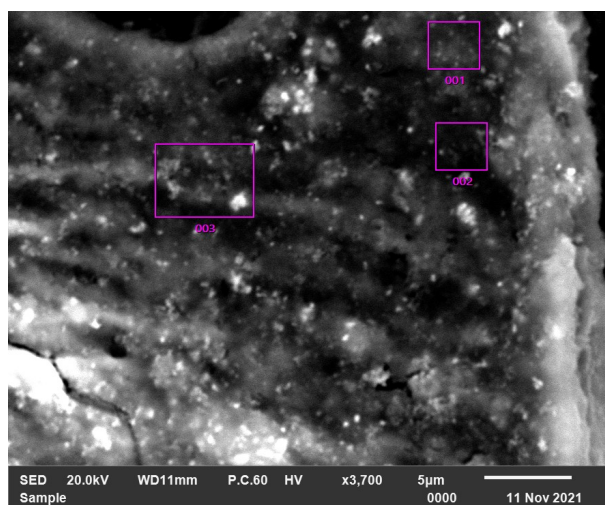


**Figure 3.8:** An SEM image of BoL anode catalyst layer used in a RDE set-up, the purple squares indicate the areas used for EDX elemental analysis

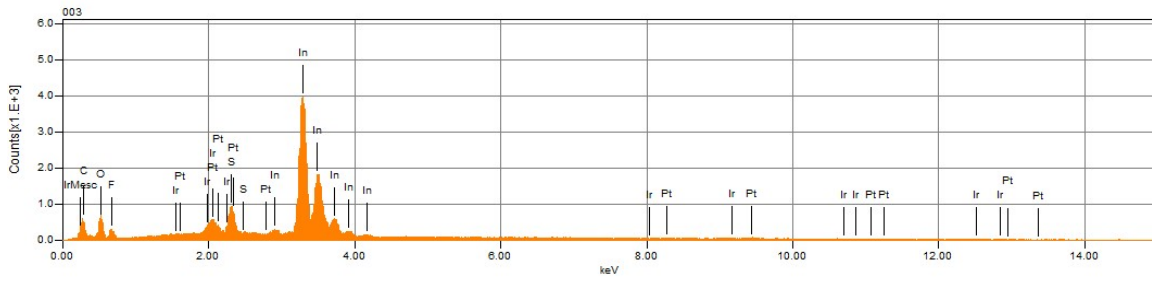


**Figure 3.9:** An EDX elemental analysis of square 3 from Figure 3.8 with on the x-axis the energy applied and on the y-axis the photon intensity detected

# Chapter 4

## Experimental

### 4.1 Ink preparation

The RTA ink was processed by mixing of platinum supported on carbon (Pt/C), solvent (aqueous alcohol with a fixed ratio), ionomer (sulfonated perfluorinated ionomer with equivalent weight  $< 900$  g/mol) and iridium oxide supported on titanium oxide ( $\text{IrO}_x/\text{TiO}_x$ ). The amount of ionomer added to the ink is normally represented as a ratio of the ionomer weight to the carbon weight also known as I/C ratio. In this research, the different amounts of ionomer chosen were  $\text{I/C} = 0.8$  and  $\text{I/C} = 1.0$ , these inks are referred to in this report as LIC (Low I/C) and HIC (High I/C), respectively. Besides, the weight of iridium was fixed fixed 1:1 to the weight of Pt. All the materials were placed in a beaker, which was filled additionally with zirconia beads. By accelerating the beads with a rotator, the zirconia beads will collide and break up the Pt/C and IrOx into smaller particles, a process also known as ball milling [135]. The time of stirring is related to the energy introduced to the system and therefore will cause differences in sizes of the Pt/C and IrOx particles. After a short amount of time a sample was taken out and measured with XRF to ensure the weight ratio of Pt and Ir was 1:1. Next to this, this ink sample was taken out and labeled as the big particle sample (BP) and its PSD was characterized by laser diffraction and used for further electrochemical analysis. The stirring was continued for several hours and the PSD was followed by laser diffraction. After a certain amount of time, the ink was taken out and labeled as small particle (SP) and the PSD was determined. The ink samples taken (BP and SP) were stored by putting it on rollers and keeping it slowly in motion. This was done to prevent the agglomeration of the particles over time, which would mean loss of the well dispersed ink. Besides, the PSD was performed after several weeks on the big particles and small particles sample. This was done to make sure that the two different inks showed similar PSD as just after the processing and agglomeration didn't occur over time in the inks.

## 4.2 Electrode preparation

The working electrode and its components are shown in Figure 4.1. The RTA catalyst layer was placed on the glassy carbon disk, which possesses a surface area of  $0.196 \text{ cm}^2$ . The glassy carbon is held with a PTFE U-cup into a PTFE shroud and the back of the carbon tip is electronically connected with a golden tip, which allowed the conduction of the current through the rotor towards the potentiostat.

Before coating the catalyst layer, the surface of the glassy carbon tip had to be polished. Polishing is a highly important process because it helps to diminish surface effects of the glassy carbon on the measurements. The surface of glassy carbons can undergo oxidation in air and irreversible changes can occur in electrolyte when doing electrochemical tests [136]. Polishing was executed with the use of alumina ( $0.05 \text{ }\mu\text{m}$ ) and diamond ( $1.00 \text{ }\mu\text{m}$  slurries). The alumina polish was executed before every measurement and the diamond polish was performed additionally before every  $3^{\text{rd}}$ , both with their own corresponding polishing pad. 2-3 drops of the slurry and water was placed on the polishing pad and the glassy carbon was polished by making "8" figures for 5 minutes. After that, the tip of the working electrode was rinsed with DI water, placed in an ultrasonic bath for 3 minutes and finally dried with  $\text{N}_2$ .

A sample of the processed ink was taken and diluted by a factor 10 with the same aqueous solvent that was used for the processing of the ink. The diluted ink was placed on roller bars in order to mix the ink with the solvent for at least 15 minutes. The rotator of the RDE set-up was taken and placed upside down with the polished working electrode on top while rotating at 300 RPM. After this, a calculated amount of diluted ink was taken with a pipette and dispersed on the rotating electrode's glassy carbon and was dried in the atmosphere. The quality of the coating was checked with an optical microscope. If it looked well the surface was further analyzed with a laser microscope before electrochemical testing. The amount of diluted ink was calculated so that the amount of Pt and Ir on the electrode surface both equaled  $50 \text{ }\mu\text{g}/\text{cm}^2$ . Many literature describe that before coating the diluting ink, it should be placed in an ultrasonic bath in order to get a more homogeneous dispersion. However, since this research is focused on the differences in particle size, it is important that the diluted inks were not placed in the ultrasonic bath. Since, this will alternate the particle size as can be seen in Figure 4.2.

After electrochemical measurements, the tip was gently rinsed with ultra pure water in order to remove the electrolyte from the catalyst layer. This was followed by applying a few drops of ink solvent on the catalyst layer. The catalyst layer dissolved into the solvent, which allowed pipetting the drops into a small flask. Because of this the EoL catalyst layer could be stored and later on being used for further material characterization (XPS & SEM/EDS).

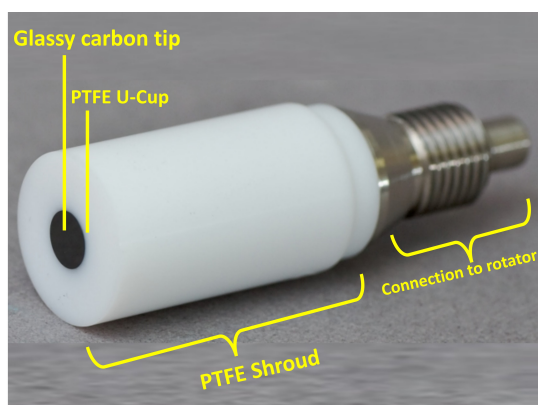


**Figure 4.1:** An image of the changeable working electrode used in this research with its components [137]

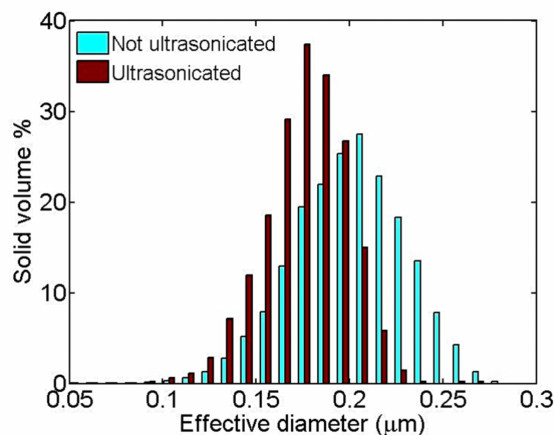


**Figure 4.2:** PSD differences between ultrasonicated and non-ultrasonicated particles [138]

### 4.3 Electrochemical protocol

All the electrochemical tests started with the conditioning of Pt. This was done by executing 150 cycles between 50 and 1200 mV with a sweep rate of 100 mV/s at 0 RPM. The amount of cycles was chosen as a standard because it resulted into a stable CV (see Figure 4.3). After the conditioning, an ECSA was made with 4 cycles between 65 and 865 mV with 100 mV/s with the rotator set on 1600 RPM. The last cycle was used to determine the ECSA. After this the current hold or the AST was started.

#### Current Hold

For the current hold (chronopotentiometry) 10 mA/cm<sup>2</sup> was applied with a rotational speed of 1600 RPM and the potential was monitored against the time. When applying rotations, it was chosen to use 1600 RPM as a standard for all tests in this research. This value was chosen to prevent damage to the working electrode, even though higher rotations could lead to better evacuation of the formed oxygen bubbles by the OER. High rotational speed lead to higher centrifugal forces on the glassy carbon disc, which can widen the PTFE U-Cup and shroud. This can lead to acidic electrolyte flowing behind the glassy carbon, where it can corrode the electrical connections. After the current hold, the Pt conditioning and an ECSA measurement was executed.

#### Accelerated Stress Test (AST)

For the accelerated Stress Test (AST) a procedure has been developed to minimize the effects of bubble formation on the catalyst layer. After the conditioning and an ECSA measurement as described before, an EIS test was applied (at 0.4 V with a range of 100 kHz to 100 mHz). This was followed by a cyclic voltammetry, where the potential was swept 10 times from 1200 to 1650 mV with a sweep rate of 10 mV/s at 1600 RPM. This cycling was done to follow the OER activity.

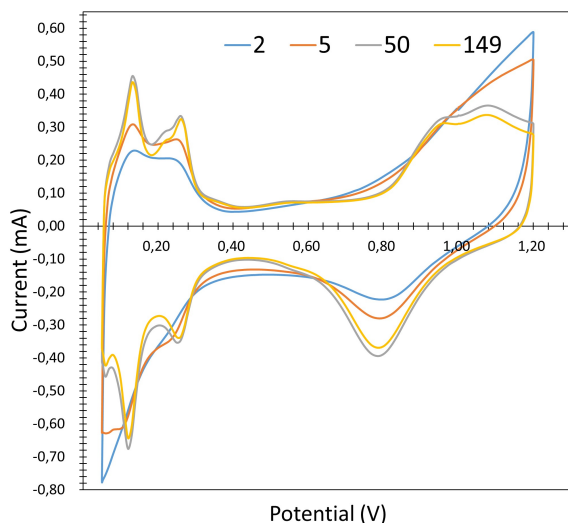


**Figure 4.3:** The different lines indicate the different cycles during the initial conditioning of Pt

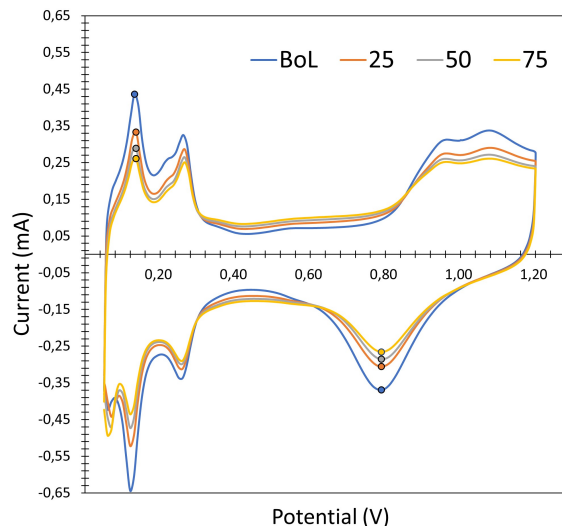


**Figure 4.4:** The different lines indicate the 15<sup>th</sup> conditioning cycle at that specific step in the AST, whereas the dots indicate the minima or maxima of the peaks

1.6 V was chosen as reference point to obtain the activity at that point (in mA/cm<sup>2</sup>) based on other literature found [139][140]. After cycling in the OER region, a potential hold at 50 mV for 8 minutes with 1600 RPM was applied. This was done to let the oxygen bubbles evacuate without an additional electrochemical stress, hence the name relaxation for this action. 50 mV was used for the relaxation, because this is the approximate potential of the anode during operation. After the relaxation, 15 cycles of Pt conditioning and 4 cycles for an ECSA measurements were executed. The OER cycling, rest, conditioning and ECSA are labeled as a single "step". The steps were in total 75 times executed. Finally, an EIS test measurement was repeated again, in order to obtain the EoL resistances.

Afterwards, an analysis was executed in order to make sure that the reference electrode was stable and not shifted during the whole AST. The potential of the Pt peaks at the 15<sup>th</sup> conditioning cycle within a step during the AST was kept track on, as can be seen in Figure 4.4. The integral of these peaks can change during a measurement due to the change of available surface of Pt (see 3.1.2 *Electrochemical Surface Area (ECSA)*). However, the position of these peaks should always be the same for a material. A small shift (e.g. 2 mV) in these peaks could have huge consequences for the OER activity results, because in this region the activity (mA/cm<sup>2</sup>) develops exponential versus the potential. Therefore, it is very important to make sure that the reference electrode remains stable during measuring.

# Chapter 5

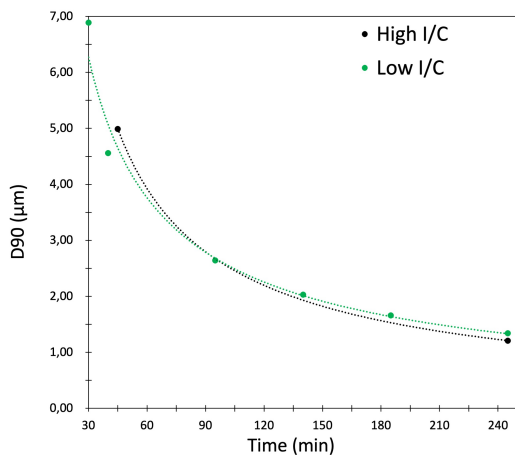
## Results & Discussion

### 5.1 Begin of life characterization

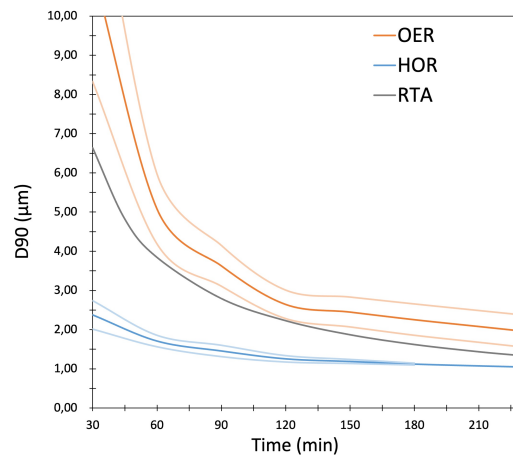
#### 5.1.1 Particle Size Distribution (PSD)

The results of the PSD development over the ball milling time can be found in Figure 5.1. D90 (in  $\mu\text{m}$ ) refers to 90% of the particles that have a diameter smaller than the corresponding value given on the y-axis [130]. In Figure 5.1a, it can be seen that for both RTA inks (HIC and LIC) used in this research the particle size decreased over time. The big particle samples were taken after 40 and 45 minutes for the LIC and HIC inks, respectively. This resulted into a D90 values of 4,56  $\mu\text{m}$  and 4,99  $\mu\text{m}$  for the LIC and HIC, respectively. The samples that were labeled as small particle in this report were both taken after 245 minutes of ball milling time. This resulted into a D90 value of 1,34  $\mu\text{m}$  for the LIC and 1,21  $\mu\text{m}$  for the HIC ink. It is worth noting that for the HIC ink, the PSD was determined only after 45 and 245 minutes. Contrary to the LIC ink, which PSD was determined with certain time intervals during ball milling. However, it was assumed that the HIC ink did follow the same trend as the LIC ink concerning the decrease of D90 over the ball milling time as can be seen in Figure 5.1a. Based on this an average was taken for both inks, which allowed a PSD comparison of the RTA inks with the inks solely existing out of HOR or OER particles (see Figure 5.1b).

It can be seen that the ink with the OER particles only had a higher D90 value and bigger standard deviation over the ball milling time compared to the ink with HOR particles only. The PSD of the OER particles decreased fast in the beginning, but over time the decrease slowed down. The PSD of HOR particle ink did not show the high initial D90 value as the OER particles ink and neither did decrease that fast. Based on this, it can be concluded that the biggest contributor to the higher D90 value in the beginning of the inks analysed in this report originates from the bigger OER particles. However, it should be noted that still the particle size of the HOR particles is also significantly decreased with a factor of 1,82 from 45 to 180 minutes. The OER and RTA inks decreased with a factor 3,54 and 2,97, respectively.



(a) Fitted curve of of the RTA two inks made



(b) HOR particles only, OER particles only and RTA ink average made from (a)

**Figure 5.1:** Particle size distribution (D90 in  $\mu\text{m}$ ) over the ball milling time for the different inks, where the light shaded colours in (b) refer to the standard deviations measured (data from the HOR & OER particles only inks were obtained from previous measurements by K. Aylar)

### 5.1.2 X Ray Fluorescence (XRF)

Next to the PSD, the big particles and small particles samples from the HIC and LIC inks were also measured by XRF during processing. XRF works by the same principles as EDS, which is described *3.2.4 SEM/EDS Analysis*. Except that only secondary elements are detected and not a vacuum is necessary. Besides, with the use of a wavelength dispersive analysis, quantitative results of Ir and Pt in the ink dispersion could be executed [141]. XRF was executed to exclude mixing errors and to make sure that the right amount of HOR and OER catalyst would be loaded on the working electrode. The big particles (40 & 45 minutes mixing) and small particles (245 minutes mixing) samples were taken and measured by XRF during the processing of the LIC (see Table 5.1) and HIC ink (see Table 5.2). It can be seen that for both the RTA inks regardless of particle size, the ratio of Ir and Pt is almost 1:1.

	Pt	Ir
Big Particles	$18.7 \pm 0.1$	$18.2 \pm 0.2$
Small Particles	$18.7 \pm 0.1$	$18.3 \pm 0.3$

**Table 5.1:** XRF of Low I/C in g/L

	Pt	Ir
Big Particles	$17.7 \pm 0.2$	$17.2 \pm 0.1$
Small Particles	$17.5 \pm 0.1$	$17.5 \pm 0.1$

**Table 5.2:** XRF of High I/C in g/L

However, the concentrations of Pt and Ir are slightly higher for the LIC ink. This can be explained that a different ionomer concentration requires a different amount of solvent. This resulted into a concentration difference between the HIC and LIC ink. As mentioned in *4.2 Electrode preparation*, it was aimed to have  $50 \mu\text{g}/\text{cm}^2$  for both Pt and Ir on the working electrode. Because of this, the volume of ink that needed to be applied for coating the catalyst layer on the working electrode was different for the HIC and LIC ink.

The amounts calculated on beforehand are in line with the results found by XRF. Therefore, the XRF results are a conformation that for both inks, there was an equal amount of Ir and Pt present when the ink was applied on the working electrode.

### 5.1.3 Surface Roughness

The average roughness ( $R_a$ ) results of the coated catalyst layers can be found in Figure 5.2. It can be seen that the coating from the big particles possessed a higher  $R_a$  value for both inks than the RTA coatings made from smaller particles. This can be explained by the fact that bigger particles cause bigger peaks and valleys on the micrometer scale in the catalyst layer structure. An example can be seen in Figure 5.3, where the rougher sample originates from the big particles. The reasoning why the bigger particles show a rougher surface, could be explained by the effect of particle diameter on the drying process. The smaller the particle the slower the particles settle in a dispersion while drying [142]. This effect gives the smaller particles more time to settle down and give rise to a more homogeneous catalyst layer coating compared to the bigger particles.

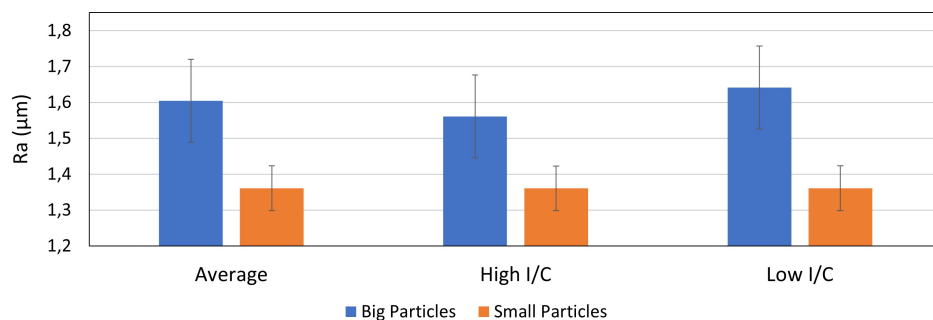
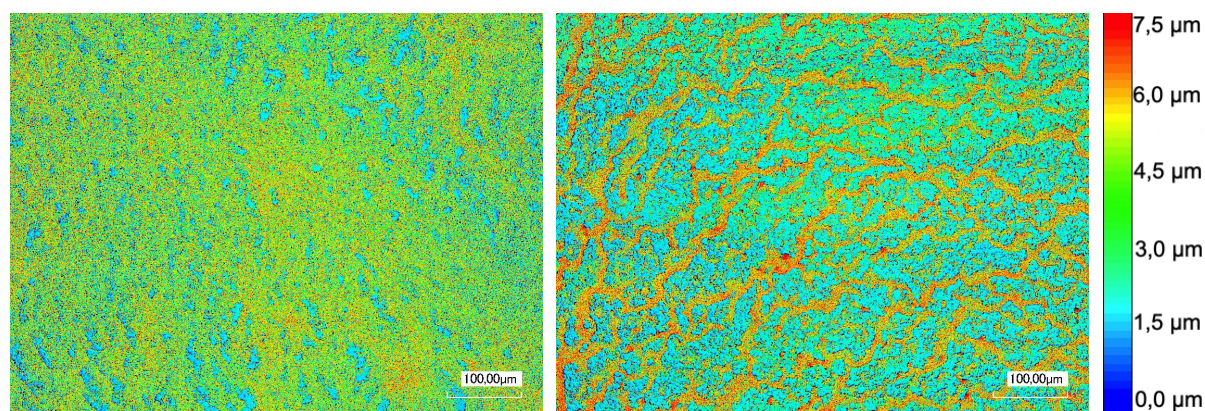


**Figure 5.2:** The average surface roughness results from the coated catalyst layers on the working electrode



(a) Sample of small particle catalyst layer with  $R_a=1.36$  (b) Sample of big particle catalyst layer with  $R_a=1.57$

**Figure 5.3:** Height images of the catalyst layers made from different particle sizes, the legend on the right indicates the height with the corresponding colour

The catalyst coatings labeled as small particles for both inks had almost a similar  $R_a$  value (HIC= $1.36 \pm 0.07 \mu\text{m}$  and LIC  $1.36 \pm 0.06 \mu\text{m}$ ). This is different for the big particles, whose average had a bigger deviation between the inks (HIC= $1.56 \pm 0.13 \mu\text{m}$  and LIC  $1.64 \pm 0.12 \mu\text{m}$ ). A suggestion that could be made is that for the high I/C there is more ionomer on the surface, which will result into a more smooth surface. But this relation is very unsure and a conclusion could not be drawn out of it and more investigation would be necessary. Especially, since the standard deviation of the average  $R_a$  value of both inks is relatively big and overlapping. Besides, this relation cannot be found back in results of the smaller particles, where the  $R_a$  values are almost equal for both inks. Furthermore, it should be noted that the HIC and LIC inks contain two different particles (Pt/C & IrO<sub>x</sub>/TiO<sub>x</sub>). The two inks only made of HOR and OER particles showed a relatively high value of the PSD at the same ball milling time when the big particles samples were taken from the RTA ink (40/45 minutes) (see Figure 5.3b). Therefore, a bigger variety of particle sizes can be expected in the big particles RTA inks. This will result into higher  $R_a$  values with a bigger variety of the  $R_a$  value between the catalyst layers made by big particle ink.

#### 5.1.4 Electrochemical Surface Area (ECSA)

As mentioned before, the ECSA was measured electrochemically with cyclic voltammetry. The BoL ECSA results of the big- and small particles HIC- and LIC ink are shown in Table 5.3. It can be seen that there is no significant difference between the big particles and small particles with the same I/C. However, an ECSA difference could be obtained between the HIC and LIC coatings, where the HIC catalyst layer showed a lower Begin-of-Life ECSA than the LIC catalyst layer. As explained in the XRF results (see 5.1.2 *X Ray Fluorescence (XRF)*), the ECSA difference could not be a result from a manual error when mixing the ingredients.

	Big Particles	Small Particles
High I/C	35,7 ± 2,2	35,3 ± 2,0
Low I/C	39,2 ± 2,1	38,8 ± 2,2
Average	37,4 ± 2,9	

**Table 5.3:** Results of all the BoL ECSA's in m<sup>2</sup>/g of the catalyst coatings

On first sight, this results seem to be quite contradictory because when particle size is reduced an increase of surface area will result. Using the same amount of ionomer for an increased surface area would mean less ionomer available. Therefore, one could argue that by using smaller particles, and hence increase of surface area would lead to a similar effect as decreasing the amount of ionomer. This relationship seem to be opposed by the results of this research.

Suzuki et al (2020) also found that there is no correlation between the decrease of particle size and increasing surface area of ionomer layer and ECSA. Here it was suggested that smaller particles would result into more burying of the pores containing Pt, which will compromise the increased surface area [142]. However, another reasonable explanation can be found in the manner of how ionomer attaches itself to the Pt/C particles. When processing the ink, the polymer molecule of the ionomer will unfold itself in the solvent and will be attracted towards the Pt/C particle. The force of this attraction depends on dielectric constant/polarity of the solvent, hydrophilic/hydrophobic character of the ionomer/catalyst layer support and chain length of ionomer [143][144]. If an excess of ionomer is assumed: the stronger the attraction between Pt/C and ionomer, the thicker the coated ionomer layer on the Pt/C surface. The process of unfolding of the ionomer in a solvent, being attracted towards the Pt/C catalyst and finding its equilibrium structure will be done within hundreds of nanoseconds [145]. So the formation of the ionomer layer on the Pt/C particle is way much quicker than when the first big particle sample was taken after 40/45 minutes. If this thick ionomer layer has such a strong attraction towards the Pt/C particles, it means that it will stay on its place even though the particle size will be reduced. Therefore, when coated and measured the small particles don't show a change in ionomer layer compared to the big particles and a similar ECSA could be obtained. This principle is shown in Figure 5.4.

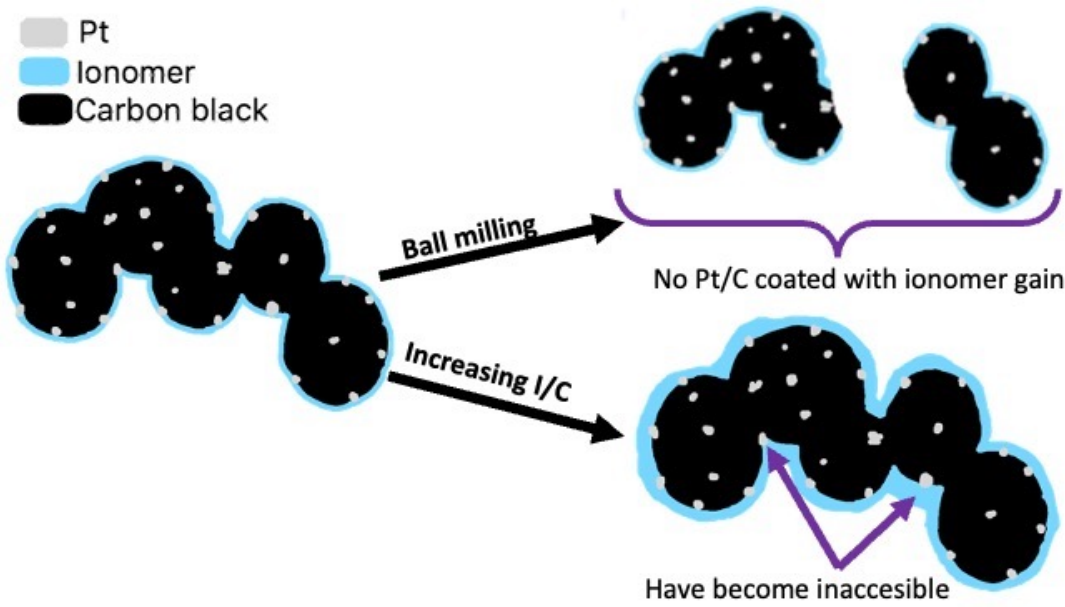


**Figure 5.4:** Schematic proposed explanation about the differences in ECSA obtained

This aforementioned explanation can also help to clarify why an increased I/C causes a lower ECSA. Because, more ionomer is available and hence a thicker ionomer layer will be coated on the Pt/C due to its strong attraction to the ionomer. This could again have the ability to stay stable over the ball milling time. The ECSA versus the I/C always comes with an optimum. Because, too less ionomer results into an increase of ionic resistances, since not a good network can be formed to conduct the protons. The ionomer is still necessary in a RDE set-up to deliver the protons to the Pt, even though there is an acidic electrolyte. This originates from the diffusion layer between the bulk electrolyte and surface electrode, therefore the electrode surface is not in direct contact with the bulk electrolyte [146]. Besides, if too little ionomer is added it could also mean that some potential electrochemical active Pt particles are not covered. On the other hand, too much ionomer can cause that electronic connections can be blocked and therefore the Pt cannot discharge the electrons, causing a decrease in ECSA [10]. Concerning the ECSA, in this research between the two RTA inks, the optimum I/C was found to be 0.8 (LIC).

## 5.2 Accelerated Stress Tests (AST)

The goals of developing a new AST in this research were to:

1. Diminish the effect of bubble formation on the activity
2. Follow the degradation over time electrochemically
3. Make sure the degradation originates from the potentials that occur during fuel cell reversal on the anode

It was chosen to cycle the voltage between 1.2 and 1.65 V with a sweep rate of 10 mV/s and to check the activity at 1.60 V for the oxidation sweep. It can be seen in Figure 5.5, that the activity decreased over 10 cycles at 1.60 V. However, when this is followed by a period where the potential is kept at 0.05 V (approximate operation potential of anode) for 8 minutes while still rotating (1600 RPM). It was found that the activity was restored (see Figure 5.7), meaning that the relaxation time (at 0.05 V) after the cycles in the OER region caused the oxygen bubbles to evacuate. Furthermore, it is desired to follow the ECSA during the AST, because this is a parameter that depends on the morphology of the material. If the ECSA is changing, it means that an alternation on the Pt/C catalyst layer is going on. It was found that an ECSA measurement between each step (10 cycles of OER measurements) increased the activity of the OER afterwards. Therefore, it was decided to add an ECSA measurement between every step. So, 1 step exists of an OER activity measurements (10 cycles 1.2 - 1.65 V) 8 minutes of relaxation at 0.05 V with 1600 RPM and an ECSA measurement. However, the addition of an ECSA measurement could add an uncertainty to point (3) mentioned above. For that reason, a measurement was executed without OER cycles to see if the ECSA stayed stable over time. This was found to be true (see Figure 5.6), which made this AST a suitable technique for analysing the stability of the RTA in the OER region.

Besides, no differences in ECSA or OER activity could be found in this ECSA over time in  $N_2$  or atmospheric conditions. Therefore, it was decided to use atmospheric conditions to reduce the chance of contamination coming from the  $N_2$  gas lines.

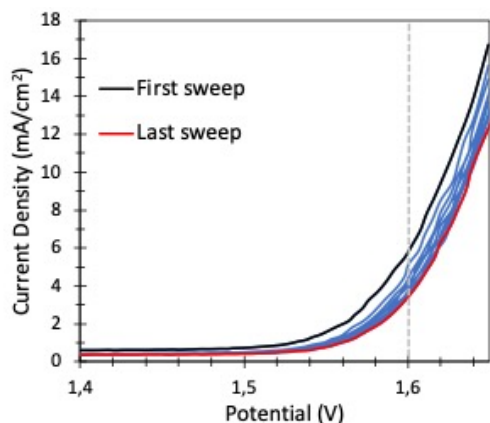


**Figure 5.5:** 1 step with 10 OER cycles, where only the oxidation sweep is shown

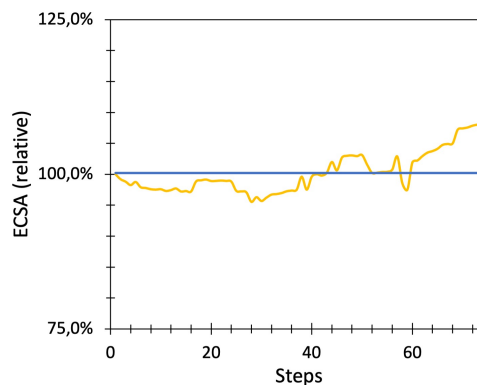


**Figure 5.6:** ECSA development without OER stress (yellow line) and average relative ECSA (blue)

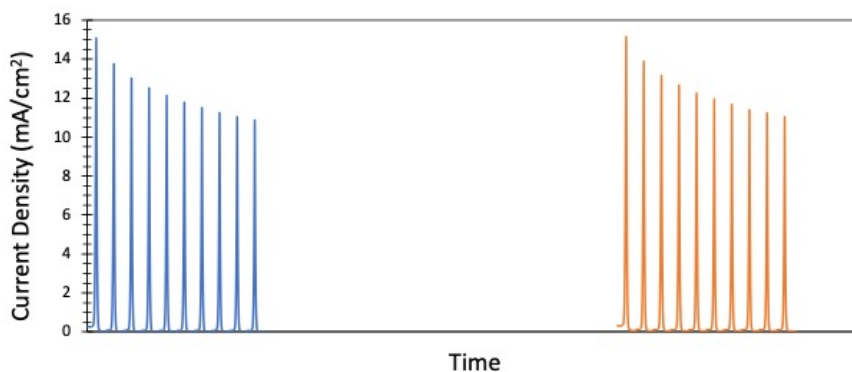


**Figure 5.7:** OER activity measurement (10 cycles 1.2 - 1.6V) of a step (blue) and the regeneration of the activity for the next step (orange) after relaxation time and an ECSA measurement

## 5.2.1 Activity

The development of the activity over the steps in the AST can be seen in Figure 5.8. Here the 2<sup>nd</sup> (Figure 5.8a) and 10<sup>th</sup> (Figure 5.8b) cycle of each step are shown, where the 10<sup>th</sup> cycle has a lower activity than the 2<sup>nd</sup> due to the blockage of oxygen (see Figure 5.5 & 5.7). It should be noted that there was no activity difference found between the different I/C applied to the ink processing. Therefore, the average with standard deviations of the big particles and small particles with both HIC and LIC are shown in Figure 5.8. There are three things that can be seen from the activity results. First, the small particle catalyst layer show a higher OER activity than the bigger particles.

Next, the activity increased a bit in the beginning (first 3 steps) followed by a decrease over steps in the AST. Finally, the standard deviation of the activity measured at 1.6 V is bigger for the big particle than the small particle catalyst layers.

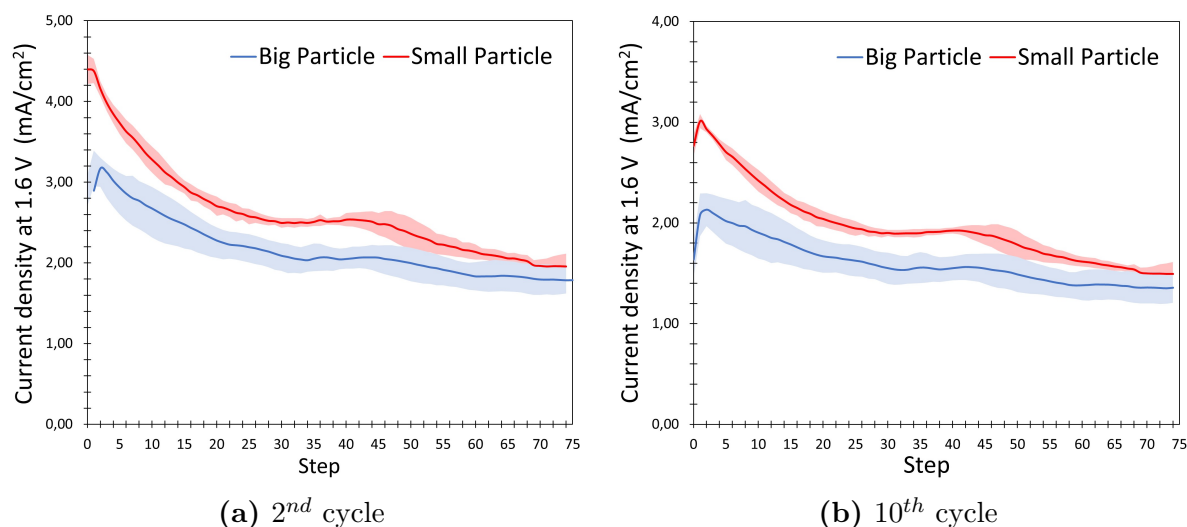


**Figure 5.8:** Activity measurement at 1.60 V of the indicated cycle versus each step of the AST. The dark coloured line indicates the average value, whereas the associated shaded area color indicates the standard deviation

Contrary to the BoL ECSA, the OER activity changed upon ball milling. This is thought to originate from the increase of surface area, more contact points with the ionomer and the less porous structure of  $\text{IrO}_x/\text{TiO}_x$  particles. As mentioned earlier, the surface area of the OER particles increased absolute and relatively more during ball milling than HOR particles. Next to this, still the same assumption can be made that upon ball milling the ionomer will remain on the same surface of the particle due to the strong interaction (see 5.1.4 *Electrochemical Surface Area (ECSA)*). When the size of OER particles were reduced due to the ball milling, it will be left with some uncoated parts (see Figure 5.9). However, in the final catalyst layer structure on the working electrode, the small OER particles will be able to share with the ionomer originating from the HOR particle. This effect will increase the effective area for the OER particles. Therefore, the OER particles will show a higher activity upon increasing the ball milling time. Sharing the ionomer doesn't have much effect on an increase of ECSA. As explained in 2.3.1 *Porosity*, the Pt particles are located into the micropores and on the carbon surface. Meaning that sharing the ionomer originating from the OER particles doesn't necessarily reach the Pt particles in the porous structure. Besides, the surface area of the Pt/C ( $60 \text{ m}^2/\text{g}$ ) is higher than the  $\text{IrO}_x/\text{TiO}_x$  ( $15 \text{ m}^2/\text{g}$ ) particles. This means that it's more likely that an uncoated OER particle finds a coated surface of the Pt/C than the other way around. Besides, increasing the ionomer content didn't increase the OER activity. This can be explained, if the ionomer will stick on the surface in the same manner as discussed in 5.1.4 *Electrochemical Surface Area (ECSA)*. Therefore, no extra gain will be made on the the effective surface area of the OER particles.

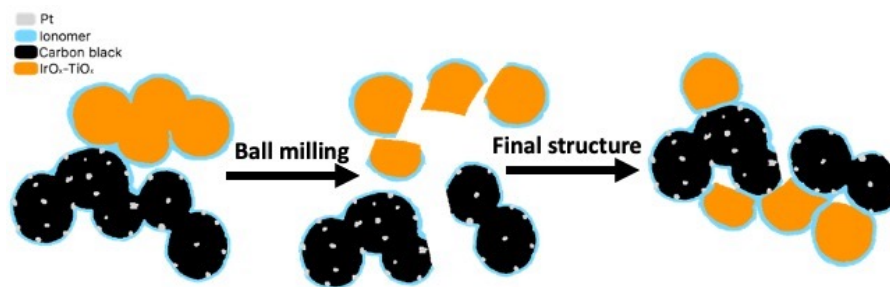


**Figure 5.9:** Schematic proposed explanation about increase of OER activity due to ball milling

The OER activity went up a little bit in the beginning, followed by a decrease till the end of the AST as can be seen in Figure 5.8. The small initial rise of activity could probably originate from some metallic Ir, which is present and is not an OER catalyst. However, after a few cycles all the metallic Ir will be transformed to  $\text{IrO}_x$ , which is an OER catalyst [147]. A Tafel Slope analysis was performed on the 2<sup>nd</sup> and 10<sup>th</sup> cycle at step 3 and 75 in the AST, as was shown in Figure 3.2. This was done to see if a change in kinetics could be found. It was found that all the values of the Tafel slope were very close (see Table 5.4) and no significant difference could be obtained between the catalyst layers from big- and small particles, HIC and LIC, BoL and EoL. This means that the OER mechanism on the  $\text{IrO}_x/\text{TiO}_x$  particles remained very stable during the AST and did not differentiate between the difference processing techniques. The lacking effect of  $\text{IrO}_x$  particle size on the Tafel Slope was also found by Reier et al (2012), who also indicated the highly stable  $\text{IrO}_x$  [139]. However, additional material characterization and EIS indicated the probable reason for the decrease of activity and will be discussed further in 5.2.5 *Degradation phenomenon*.

	HIC	LIC
Small Particles	$53.3 \pm 2.5$	$53.1 \pm 1.6$
Big Particles	$54.0 \pm 2.5$	$51.9 \pm 1.0$
Average	$53.1 \pm 2.1$	

**Table 5.4:** Results of the Tafel Slope determinations in mV/dec, the averages shown include OER activity from cycle 2 at step 3 and step 75 of the AST

The bigger standard deviation for the bigger particles in the OER activity in Figure 5.8 can be explained by the PSD and the roughness. The D90 value for the OER particles ink is much higher in the beginning of the ball milling process. Consequently, when the big particle sample is taken, there is a bigger variety of OER particle sizes in the RTA ink. This phenomena was also seen back in surface roughness, where the bigger particles also resulted into a bigger standard deviation for the  $R_a$  values. Therefore, one could say that there is more variety of particle sizes in the the big particles sample compared to the small particle samples. In combination with the findings of Figure 5.8, where it can be seen that the particle size in the ink matters for the OER activity. It can be concluded that the bigger variety of particle sizes in the big particle sample cause a bigger standard deviation in the OER measurement than the small particle sample.

## 5.2.2 ECSA

As mentioned before, an ECSA measurement was used to have an electrochemical parameter for degradation and to get the highest activity. This allowed to keep track of the ECSA over every step in the AST. It was found that for all catalyst layers regardless of particle size or ionomer loading, the ECSA decreased in the same trend over time in the AST (see Figure 5.10). Comparing this with Figure 5.6, it can be seen that the addition of OER stress did affect the active surface area of Pt.

As discussed in *2.2.1 Consequences*, the loss of ECSA can occur due to carbon corrosion and can often be devoted to the growth of the Pt nanoparticles resulting into loss of surface area and hence ECSA. The growth of Pt nanoparticles is also known as Ostwald ripening, which is a well known degradation phenomenon of the fuel cell. Ostwald ripening doesn't occur only due to corrosion but can occur also during normal operation [148][149]. Ostwald ripening isn't thought to be the main reason why the ECSA decreases in this AST, which will be explained further in *5.2.5 Degradation phenomenon*. However, still Ostwald ripening cannot be excluded as a contributing factor to the ECSA loss. A material characterization technique that is able to confirm the extent of the Ostwald ripening is TEM analysis, which allows to measure the Pt nanoparticle sizes. Therefore, TEM analysis would be recommended in future research to find out how much the Ostwald ripening is responsible for the loss of ECSA with the AST executed in this report.

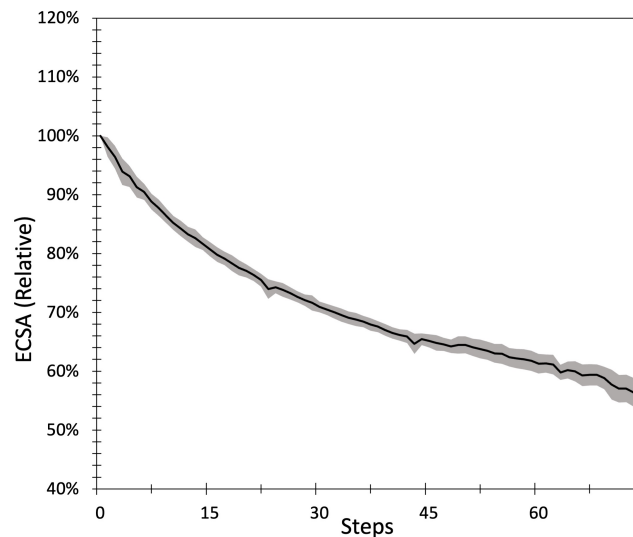


**Figure 5.10:** ECSA development in AST relative to its initial value, averaged over all AST's executed in this research

### 5.2.3 EIS

For this research, EIS was executed to follow the total electrical resistance and ionic resistance, as described in 3.1.4 *Electrical Impedance Spectroscopy (EIS)*. It should be mentioned that the electrical resistance measured with EIS is a build-up of all components in a RDE set-up (i.e. electrolyte, rotator connection, distance between working electrode and reference electrode, surface glassy carbon, etc.) [146]. Since the electronic resistance of the catalyst layer is only a small part of this, the value of  $R_{ele}$  shouldn't be directly correlated to the electrical resistance of the catalyst layer. The BoL  $R_{ele}$  found in this research are in the range from 4.6 - 10  $\Omega$ . However, if the whole set-up remains untouched during the AST and it can be assumed that only electrical properties are changed due to the change of the catalyst layer. Then, the absolute change in  $R_{ele}$  from the BoL to EoL does tell something about the change in resistance of the catalyst layer. These data are shown in Table 5.5.

For all measurements a decrease in  $R_{ele}$  has been found for the EoL compared to BoL. This can be devoted to the an increase connections in the carbon structure, which results into a better overall electron conductivity of the catalyst layer. However, the standard deviation for the  $R_{ele}$  difference for the big particles is much bigger than the small particles catalyst layers. If a big particle catalyst layer structure collapses, a better carbon connected network will be created between different aggregates (see Figure 5.11). Nevertheless, if the big particles catalyst layer stays stable then no additional electrical conductivity is gained. This opposes a collapse of smaller particles, which already exhibit a structure with a better connected. Therefore, the gain on electrical conductivity will be less than the bigger particles. Besides, a decrease of electrical resistance could also be linked to a decrease in ionomer content [150].

Furthermore, the ionic resistance was followed. A direct comparison between the  $R_{ion}$  BoL samples couldn't be made because the standard deviation was too big, which can probably be devoted to the sensitivity of resistances in a RDE set-up. Similar to  $R_{ele}$ , the BoL and EoL differences were used to observe the change in  $R_{ion}$ , the results can be seen in Table 5.5. It was found for all the samples that the ionic resistance was increased significantly. The average increase of the ionic resistance compared to its initial value was 256%. A low  $R_{ion}$  is an indicator for a thicker ionomer layer, because it gives rise to a better proton conducting network [150][151]. The fitting of the EIS is shown in Appendix B.

	$R_{ele}$ ( $\Omega$ )	$R_{ion}$ ( $\Omega$ )
Small Particles	$-0.09 \pm 0.01$	$1.90 \pm 0.27$
Big Particles	$-0.295 \pm 0.23$	$1.94 \pm 1.02$

**Table 5.5:** Electrical ( $R_{ele}$ ) and ionic ( $R_{ion}$ ) resistance differences between the BoL and EoL catalyst layers

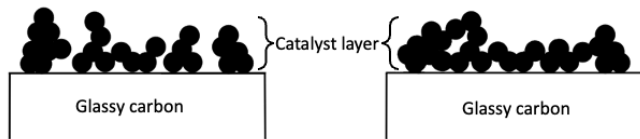


**Figure 5.11:** Schematic representation of the big particle catalyst layer coating not well electrical connected (left) and well connected (right)

## 5.2.4 Material Characterization

A BoL and EoL sample were taken from a High I/C Small Particle ink as described in 4.2 *Electrode preparation*. Concerning the BoL sample, only a ECSA measurement was executed in order to have contact with the electrolyte and have similar conditions as the EoL sample. The aim was to characterize the materials in order to find a reason for the activity and ECSA decrease in the AST (see Figure 5.8). A XPS survey and several multiplexes have been made in order to see if a change in surface could be found. It should be noted that the machine was shifted ( $\pm 4$  eV), all the peaks were adjusted accordingly. This meant that a detailed qualitative analysis was limited. Even with the shift, the results obtained with the XPS were already sufficient to make a conclusion.

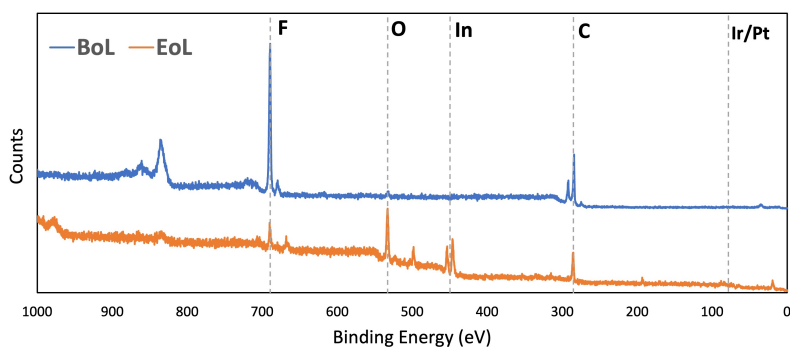


**Figure 5.12:** XPS Survey of the BoL and EoL samples

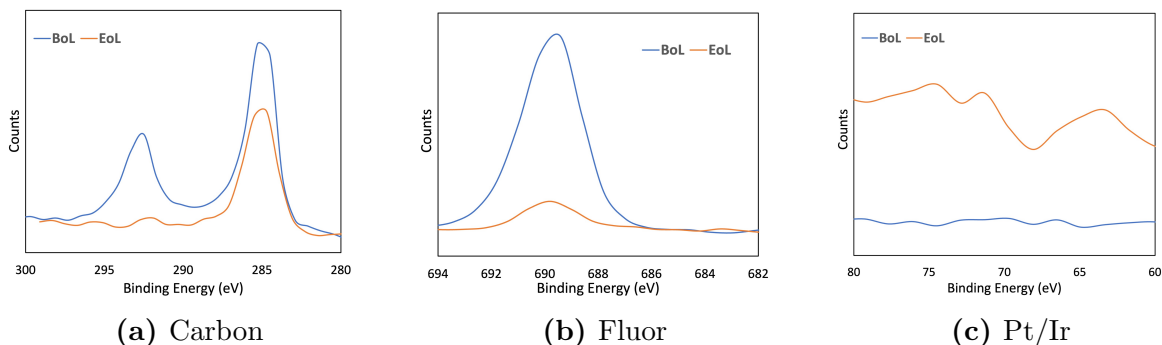


**Figure 5.13:** XPS on the regions of interest

The XPS survey of both measurements can be found in Figure 5.12. It can be seen that there are more peaks present in the EoL compared to the BoL. First, the peak at 532 eV has arisen for the EoL, which can be assigned to O1s. However, it is not used for further analysis because the oxygen can also originate from an oxidized support, where the catalyst layer was deposited on (Indium). The Indium peaks were also found at 554 eV and 446 eV. The reason why those were not detected in the BoL comes from the coverage of the EoL catalyst layer, which didn't completely cover the Indium support on the place where the x-ray beam was focused on, contrary to the BoL. The peak arisen at 500 eV couldn't be assigned to the materials applied for the XPS measurement.

Next to this, the XPS allowed a quantitative analysis on the catalysts (Pt/Ir), the ionomer (carbon and fluorine) and catalyst support (carbon). Unfortunately, the OER support (titanium) couldn't be detected. This could highly probable be devoted to the very small Ti peak that would exactly overlap with the Indium peak at 554 eV. In Figure 5.13a, the C1s of carbon can be found at 285 eV and the peak at 292 eV can be assigned to the C-F<sub>2</sub> bonds [132]. The peak at 285 eV can be assigned to the carbon catalyst support and the second one to the carbon in the ionomer [152]. The latter peak is indicative for the C-F<sub>2</sub> bond, which can be found in the Teflon backbone of the ionomer molecule (see 2.1.1 Catalyst layer & 2.1.1 Membrane). It can be directly seen that the ratio of the integral of CF<sub>2</sub> to the C1s peak has almost vanished in the EoL catalyst layer, whereas the catalyst support C1s stayed stable in the AST. The vanishing of the fluorine of the ionomer can also be seen back in the XPS fluorine region in Figure 5.13b. The peak at 689 eV can be identified as the the fluorine in (-CF<sub>2</sub>-CF<sub>2</sub>-), which is also an indicator for the ionomer layer [153]. Again an almost complete loss can be bserveed. However, a direct comparison between the intensities of the fluorine peaks between the BoL and EoL is not justified since the XPS spectrum of the EoL also exists out of more materials (indium and oxygen). Therefore, the ratio of the F peaks was determined against the C1s, following Equation 3.2.3. It was found that the C:F ratio increased from 0,86 to 10,8, which indicates a loss of ionomer on the surface. Another argument for the loss of ionomer can be found in the detection of Pt and Ir in the EoL but not in the BoL (see Figure 5.13c). The Pt and Ir peaks in the EoL can be found at 71-74 eV and ± 63 eV, respectively [132]. Since the ionomer layer is several nm thick and the penetration depth of the XPS is also several nm. It means that XPS couldn't detect any Pt nor Ir for the BoL due to the thicker ionomer layer. However, due to the loss of ionomer layer the Pt and Ir could be detected by the XPS for the EoL.

	BoL	EoL
C:F	1,05	2,48
Ir/Pt:F	1,01	2,13
Ir/Pt:C	0,97	1,16

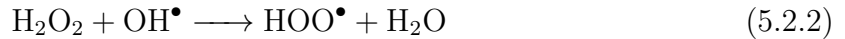
**Table 5.6:** Results of the SEM/EDS Analysis with the different ratio's between carbon (C), fluorine (F) and platinum/irridium (Pt/Ir) of the BoL and EoL samples

Next to this, an EDS measurement with SEM was executed, which results can be found in Table 5.6. It should be noted that the EDS can become unreliable when measuring Pt and Ir. This occurs because the atomic weight of Pt (78 u) and Ir (77 u) are very similar. Therefore, the intensity peaks of Pt and Ir are difficult to distinguish and make it hard to execute an quantitative measurement for the two in the same sample with an EDS [154]. This phenomenon can also be seen in Figure 3.9, where a EDS analysis is shown and all the high intensity peaks for Pt and Ir are overlapping in the region around 2 keV. Because of this reasoning, it was chosen to consider the atomic weight obtained from the EDS of the Ir and Pt as one (Ir/Pt in Table 5.6).

It can be seen in Table 5.6 that the amount of fluorine has been decreasing compared to carbon and Ir/Pt. It has decreased in a lesser extent than found by the XPS. But this can be explained by the deeper penetration depth of the EDS analysis. Besides, the Ir/Pt has increased a little bit compared to carbon. This can be attributed to the presence of carbon in the ionomer and as catalyst support. So if there is ionomer loss, there will also be a decrease of carbon content overall. However, this is in a way lesser extent than fluorine since the catalyst layer is also made of carbon. The XPS and SEM/EDS measurements both confirmed the loss of ionomer in the EoL sample compared to the BoL.

### 5.2.5 Degradation phenomenon

The material characterization techniques and the increase of ionic resistance by EIS are indicators that loss of ionomer has occurred during the AST. This is thought to originate from the chemically break up of the ionomer. First, hydrogen peroxide  $\text{H}_2\text{O}_2$  is formed, which is a side product of either the ORR or OER. Next, radicals ( $\text{OH}^\bullet$ ,  $\text{OOH}^\bullet$ ) can be formed out of hydrogen peroxide [155]. These radicals are able to attack the chemical bonds of the sulfonated perfluorinated ionomer, which will break up the polymer ionomer and result into loss of the ionomer. The formation of the radicals out of hydrogen peroxide is known as the Fenton reaction [156]. The Fention reaction is shown in Reaction 5.2.1 and 5.2.2, where M represent a metal contamination.



It is known that titanium can also be used as the metal (M) in Reaction 5.2.1 [157][158]. Since, titanium oxide was used as a support material it is highly possible that the titanium was the reason that the Fenton reaction occurred and that the ionomer was chemically degraded during the AST. It should be noted that in a PEMFC, the membrane is made out of the same material as the ionomer. Therefore, in a MEA the Fenton reaction wouldn't only destroy the ionomer in the catalyst layer, but also the membrane. This has also been stressed out by Zhang et al (2021), who urges that Titanium Oxide need to be omitted as support material for catalysts in a PEMFC [157].

The relation between ionomer content and OER activity has been described by Bernt et al (2016). Here the relation between the ionomer content and the optimal OER performance of  $\text{IrO}_x/\text{TiO}_x$  on a MEA has been described. It describes that too much ionomer leads to performance loss due to increased mass-transport resistance of oxygen evacuation. Next to this, the addition of too much ionomer can lead to more electrical isolating ionomer blocking the electrical conducting network of the carbon support. This can lead to an increase of resistance. On the other hand, too little ionomer will lead to an increased proton resistance because not a good ionomer network can be formed for the proton transport to the membrane.

At first sight, the loss of ionomer network seems to be less of a concern for the catalyst layer in a RDE set-up than in a MEA. Because, in a RDE set-up the protons could easily flow back into the electrolyte and no conduction of the protons to the membrane is necessary as in a MEA. However, a decrease of ionomer in the catalyst layer will lead to a decrease of protons pathways to evacuate the produced protons from the catalyst layer. This suggestion is schematically shown in Figure 5.14. Due to the rotation in a RDE set-up, a flux is generated as can be seen in Figure 5.14a. During the OER, oxygen and protons are created. But, flowing back into the bulk electrolyte is hard for the products since a constant flux is on the catalyst layer. The ionomer network allows the protons to be conducted to outside the catalyst layer as shown in Figure 5.14b. Therefore, the rise of a high concentration of protons near the OER catalyst can be prevented. Nevertheless, without an ionomer network the protons cannot be evacuated that well anymore, which will cause an increased concentration of protons in the pores as can be seen in Figure 5.14c and hence a locally decreased pH. Two possible reason can be suggested why the aforementioned phenomenon decreased the OER.

The first suggestion could be found in the possible pH dependence of the OER catalyst. A few OER mechanisms are described and shown in section 2.1.2 *Oxygen Evolution Reaction*. If the rate-determining (RDS) step of the OER is the deprotonation, then it could be harder to deprotonate since the catalyst is surrounded by a high concentration of protons as in Figure 5.14c. It should be noted that this is only an assumption made and is very uncertain also because the OER mechanism as of today is unknown. However, the pH dependence of the metal oxide has already been described before [159]. Further research into the OER mechanism and its pH dependence would be necessary, to confirm or deny this reasoning between the loss of ionomer and loss of OER activity.

Another possibility could be due to the IrO<sub>x</sub> dissolution during the AST. Research executed by Knöppel et al (2021) found that a lower ionomer content and a lower pH were both separately responsible for a decreased lifetime of the OER catalyst due to increased IrO<sub>x</sub> dissolution [160]. This phenomenon could also have decreased the activity of the OER catalyst in the AST executed in this research. The decrease of ionomer was found with the material characterization techniques. Unfortunately, due to the thick BoL ionomer layer no BoL and EoL comparison between the IrO<sub>x</sub> content could be made by XPS. Next to this, the overlapping regions of Pt and Ir in the SEM/EDS did neither allow a detailed quantitative analysis of BoL and EoL samples on the Ir content. A recommended suggestion would be to apply an inductively coupled plasma mass spectrometer (ICP-MS), which allows to follow the dissolution of Ir in the electrochemical cell [161].

The reason for the ECSA decrease during the AST can be found in 5.1.4 *Electrochemical Surface Area (ECSA)*, where the relation between an optimal I/C and ECSA is described. Furthermore, it can be seen that Figure 5.14c explains why the  $R_{ele}$  was found to decrease for all the samples in the AST. Because, due to ionomer loss more carbon connections arise, which will result into a more electrical connected structure.

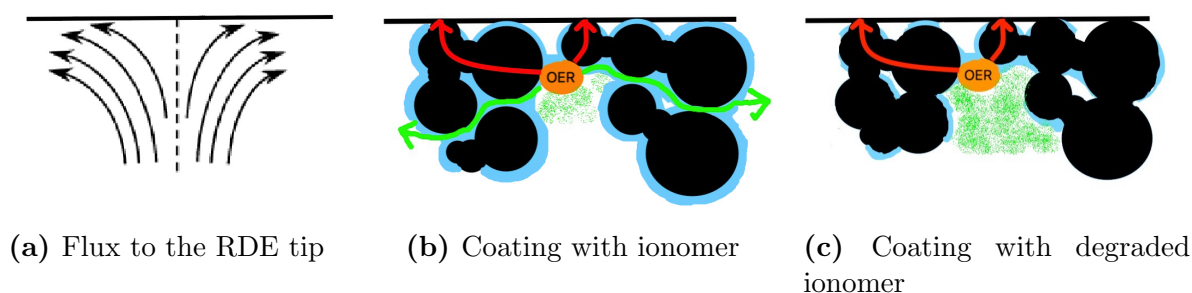


**Figure 5.14:** Catalyst layer where black represents the Pt/C particles, orange the OER catalyst, green the concentration of protons and the green lines the proton diffusion path and the red line indicates the path of the electrons

### 5.3 Reversal test

To mimic the *in situ* measurements that were discussed in 2.4 *OER catalyst*, a current hold was applied to determine the reversal time. It should be noted that the reversal time obtained in this research doesn't reflect the reversal time of a real fuel cell. This can be explained due to the troublesome evacuation of oxygen bubbles in a RDE set-up compared to the catalyst layer within a MEA. The *in situ* tests discussed in 2.4 *OER catalyst* were executed with a current of  $200 \text{ mA/cm}^2$  during a reversal test [10][12][14]. This couldn't be repeated in a RDE set-up because the reversal time would be too short and no difference between the materials couldn't be obtained. Even a current hold at  $50 \text{ mA/cm}^2$  was found to be too much for the RTA on a RDE set-up, as can be seen in Appendix C. Therefore, the current applied was adjusted till repeatable results were reached with an acceptable standard deviation. The desired current for a reversal test in a RDE set-up was found to be  $10 \text{ mA/cm}^2$  and its results are shown in Figure 5.15.

It can be seen that the big particles catalyst layer possessed a higher reversal time than the small particles. Again, no difference could be found between the two different ionomer loadings applied during the processing of the catalyst layer. Therefore, the average and standard deviations of both RTA inks are shown in Figure 5.15. It can be seen that in the range from 0 - 100 minutes, the potential is lower for the small particles. This is the result of the higher activity of the smaller particles found with the AST. Therefore, the smaller particles can generate the same amount of current at a lower potential compared to the big particles. However, this difference diminishes over time and eventually the bigger particles show a longer reversal time. This is thought to originate from the easier bubble evacuation of the bigger particles.

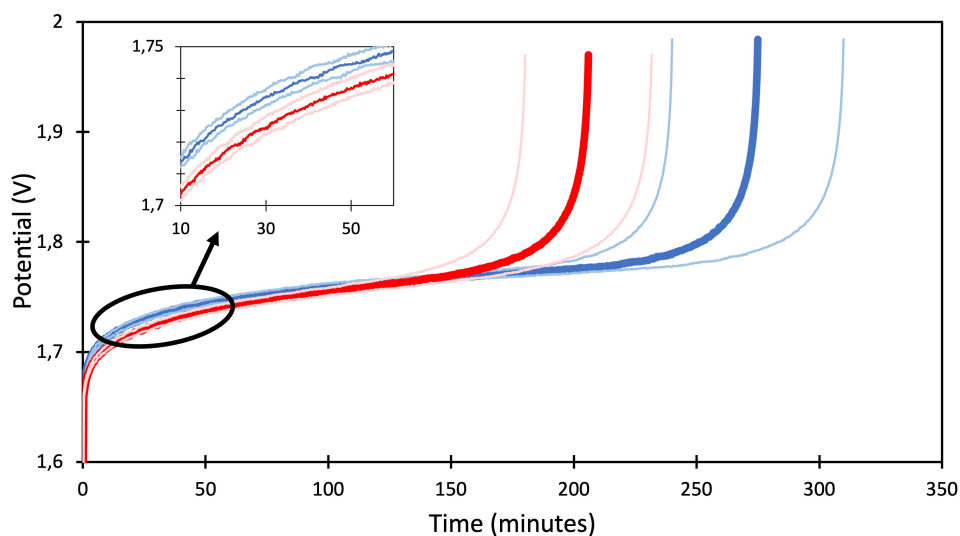


**Figure 5.15:** Results of the  $10 \text{ mA/cm}^2$  current hold tests with big particles (blue) and small particles (red) with the light shaded colour indicating the corresponding standard deviations measured

Placing an OER catalyst on the side of the catalyst layer in the direction in which the oxygen bubbles need to be evacuated improves the removal of oxygen bubbles, which was shown in Figure 2.22. This phenomenon occurs because if one bigger oxygen bubble is growing it will act like a sink in where the small bubbles will be sucked into. This extraction behaviour occurs due to the concentration gradient and is the driving force of the smaller oxygen bubbles towards the big bubble [12][162]. The bigger particle structure were found to have deeper and higher peaks in the structure, which is an indication to have wider pores on the micrometer scale (see *5.1.3 Surface Roughness*). This might help to increase the availability for more nucleation sites to have space available for bigger oxygen bubbles to grow and hence it will allow the easier evacuation of the oxygen bubbles. It can be viewed as an increased surface area for the growth of bigger oxygen bubbles.

# Chapter 6

## Conclusion

It was found that the processing of the RTA had an influence on its performance, stability and reversal tolerance at potentials that occur during fuel cell reversal. By using different ball milling times during the processing bigger particles and smaller particles could be differentiated. The bigger particles had for all measurements a higher standard deviation, which can be attributed to the broader particle size distribution of the catalyst particles. It was found that the particle size did not have an influence on the BoL ECSA, ECSA decrease during the AST nor the Tafel Slope. But, the big particles did show a higher surface roughness, lower OER activity and a longer reversal time. The lower OER activity can be devoted to the lower effective surface area of bigger OER particles. The contradiction between increased reversal time and lower OER activity is thought to originate from the easier oxygen evacuation in a bigger particle RTA catalyst layer during chronopotentiometry. The activity was found to decrease for all samples during the accelerated stress tests. EIS, XPS and SEM/EDS showed that this loss could highly probable be devoted to the loss of ionomer. The loss of ionomer is thought to originate from the presence of titanium in the catalyst layer, which allows the Fenton reaction to take place that can destroy the ionomer layer chemically. Electrochemical Impedance Spectroscopy (EIS) has proven to be very well in line with the degradation phenomena. However, due to the very sensitive RDE set-up a resistance comparison between the BoL samples couldn't be made. It would be recommended to find a way with the RDE set-up to make repeatable EIS measurements. If this could be achieved, direct comparisons between BoL catalyst layers could be made. Besides, the inclusion of TEM would be recommended to finger point and conclude the degradation phenomena on the ECSA.

This research has shown that an AST can be made for testing OER catalysts in a RDE set-up. The RTA in a RDE set-up cannot be related directly to the conditions of a catalyst layer in a fuel cell. However, this research does show that degradation phenomena and influence of the processing on the RTA catalyst layer can be very well understood with the use of a RDE set-up and additional material characterizations. Therefore, it could help to provide knowledge and new insights for future development of the RTA. Besides, it could serve as a guideline for further development of *ex situ* testing of OER catalyst materials, which could benefit the PEMFC and PEM electrolysis research.

# Appendix A

## Roughness Determination

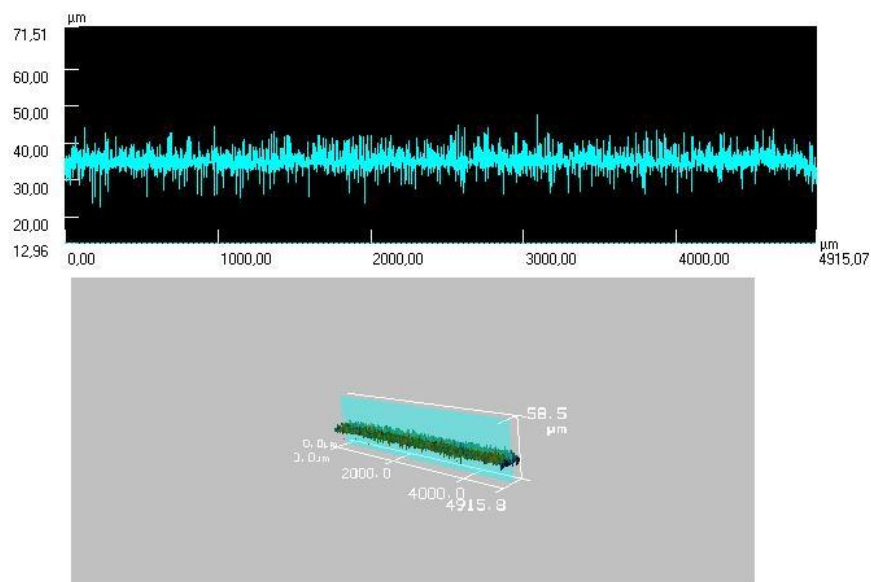
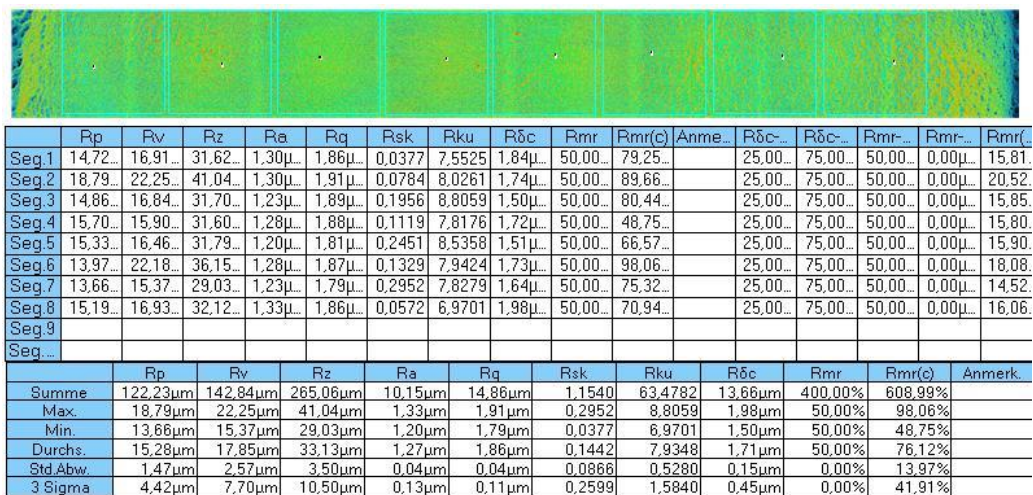


**Figure A.1:** The results of a roughness measurements obtained from the laser microscope, where the light blue squares on the picture on top indicate the segments (Seg). Seg. 1 indicates the left square and increases till Seg.9 on the right square.

# Appendix B

## EIS Fitting

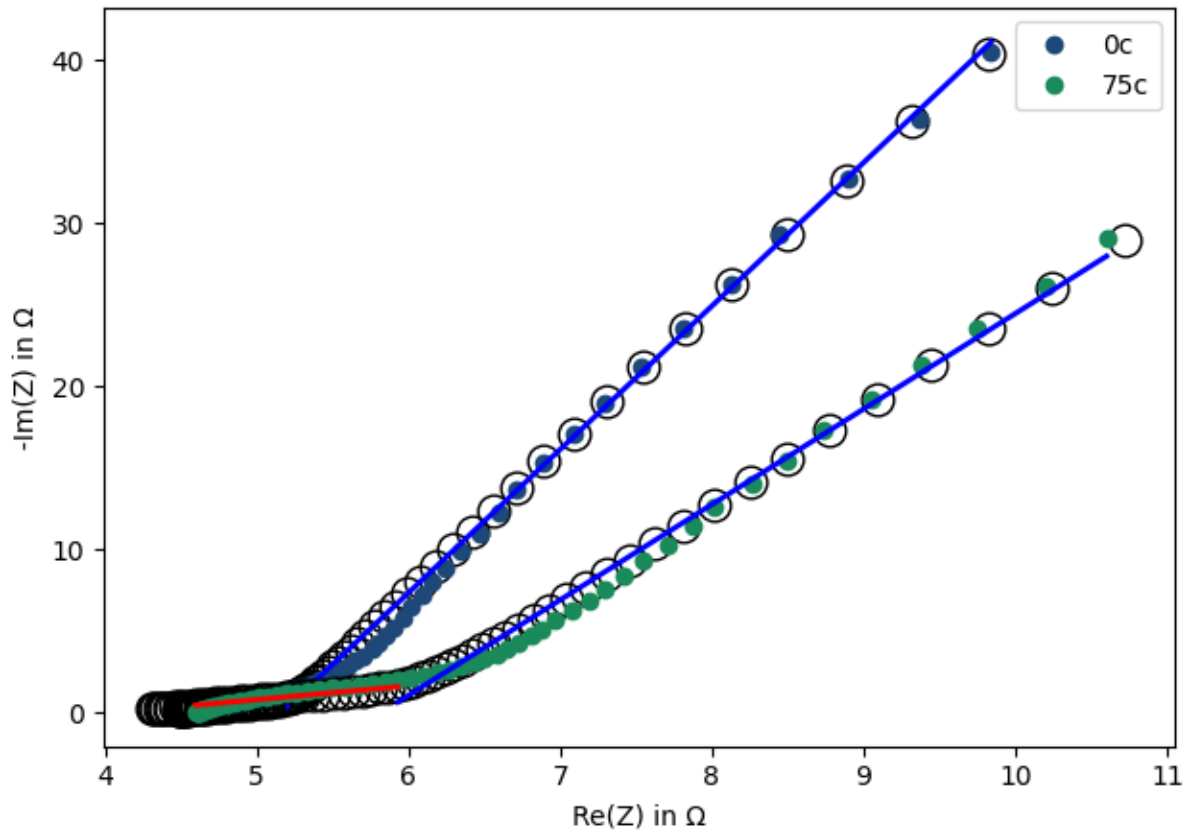


**Figure B.1:** An example of the EIS fitting based on the Transmission Line Model, this model was implemented by A. Jurjevic. The blue dots indicate the BoL sample (0c) and the green dots the EoL sample (75c). The red line indicates the fitted  $R_{ion}$  and the blue line the divergence from the  $R_{ion}$ . For this test a  $R_{ele}$  of 4,62  $\Omega$  and 4,60  $\Omega$  was obtained for BoL and EoL, respectively. Whereas for the  $R_{ion}$  1,64  $\Omega$  and 3,7  $\Omega$  was obtained for BoL and EoL, respectively

# Appendix C

## RDE reversal test at $50 \text{ mA/cm}^2$

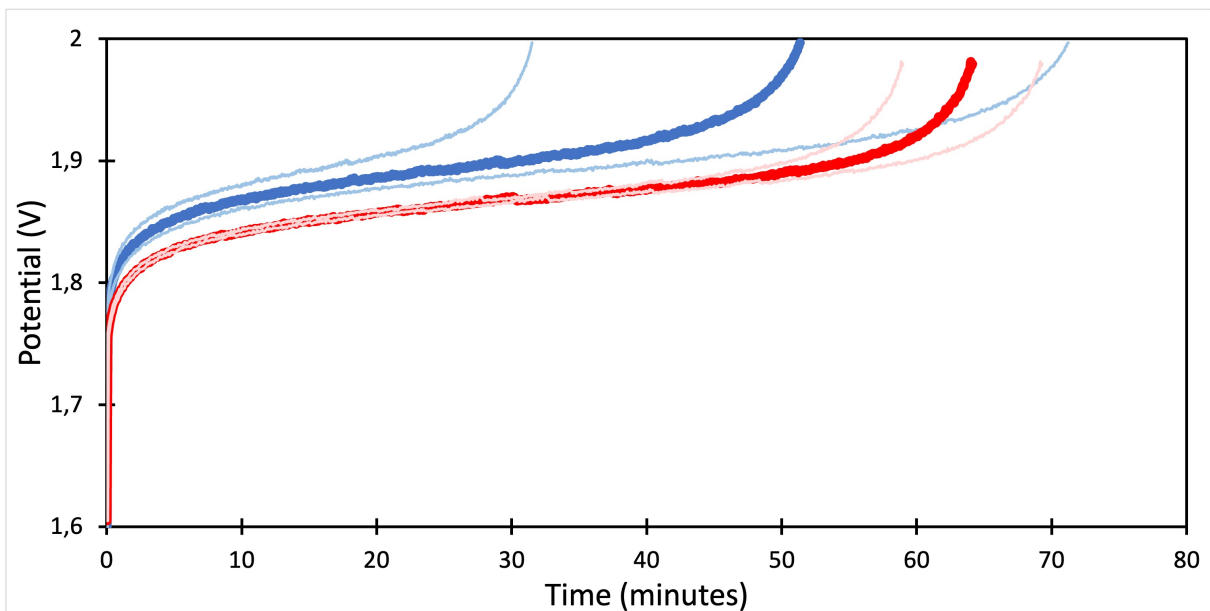


**Figure C.1:** Results of the  $50 \text{ mA/cm}^2$  current hold tests with big particles (blue) and small particles (red) with the light shaded colour indicating the corresponding standard deviations measured, showing the big and overlapping standard deviations measured. It contains the average for HIC and LIC, since no difference could be found between the two inks

# Bibliography

- [1] European Commission (EC), “Fit for 55’: delivering the EU’s 2030 Climate Target on the way to climate neutrality,” Tech. Rep., 2021. [Online]. Available: [https://ec.europa.eu/clima/citizens/support\\_en](https://ec.europa.eu/clima/citizens/support_en).
- [2] European Commission, “A hydrogen strategy for a climate-neutral Europe,” Tech. Rep., 7 2020. [Online]. Available: [https://ec.europa.eu/energy/sites/ener/files/hydrogen\\_strategy.pdf](https://ec.europa.eu/energy/sites/ener/files/hydrogen_strategy.pdf)
- [3] Deloitte and Ballard, “Fueling the Future of Mobility: Hydrogen and fuel cell solutions for transportation,” Tech. Rep., 2020. [Online]. Available: <https://www2.deloitte.com/content/dam/Deloitte/cn/Documents/finance/deloitte-cn-fueling-the-future-of-mobility-en-200101.pdf>
- [4] Transport & Environment, “Comparison of hydrogen and battery electric trucks,” 6 2020. [Online]. Available: [https://www.transportenvironment.org/wp-content/uploads/2021/07/2020\\_06\\_TE\\_comparison\\_hydrogen\\_battery\\_electric\\_trucks\\_methodology.pdf](https://www.transportenvironment.org/wp-content/uploads/2021/07/2020_06_TE_comparison_hydrogen_battery_electric_trucks_methodology.pdf)
- [5] US Department of Energy, “Hydrogen Storage.” [Online]. Available: <https://www.energy.gov/eere/fuelcells/hydrogen-storage>
- [6] B. Abderezzak, “1 - Introduction to Hydrogen Technology,” in *Introduction to Transfer Phenomena in PEM Fuel Cell*, B. Abderezzak, Ed. Elsevier, 2018, pp. 1–51. [Online]. Available: <https://www.sciencedirect.com/science/article/pii/B9781785482915500019>
- [7] Andrew L. Dicks and David A. J. Rand, “Proton-Exchange Membrane Fuel Cells,” in *Fuel Cell Systems Explained*. John Wiley & Sons, Ltd, 2018, ch. 4, pp. 69–133. [Online]. Available: <https://onlinelibrary.wiley.com/doi/abs/10.1002/9781118706992.ch4>
- [8] C. Qin, J. Wang, D. Yang, B. Li, and C. Zhang, “Proton exchange membrane fuel cell reversal: A review,” 12 2016.
- [9] Daimler, “Fuel-cell truck Start of testing of the new GenH2 Truck prototype,” 5 2021. [Online]. Available: <https://www.daimler.com/innovation/drive-systems/hydrogen/start-of-testing-genh2-truck-prototype.html>
- [10] W. Chen, C. Cai, S. Li, J. Tan, and M. Pan, “Thickness effects of anode catalyst layer on reversal tolerant performance in proton exchange membrane fuel cell,” *International Journal of Hydrogen Energy*, vol. 46, no. 12, pp. 8749–8757, 2 2021.
- [11] C.-Y. Ahn, S. Y. Kang, H. J. Choi, O.-H. Kim, Y.-E. Sung, and Y.-H. Cho, “Effect of anode iridium oxide content on the electrochemical performance and resistance to cell reversal potential of polymer electrolyte membrane fuel cells,” *International Journal of Hydrogen Energy*, vol. 46, no. 27, pp. 14 713–14 723, 2021. [Online]. Available: <https://www.sciencedirect.com/science/article/pii/S0360319921003955>
- [12] X. Zhou, Y. Yang, B. Li, and C. Zhang, “Advanced Reversal Tolerant Anode in Proton Exchange Membrane Fuel Cells: Study on the Attenuation Mechanism during Fuel Starvation,” *ACS Applied Materials and Interfaces*, vol. 13, no. 2, pp. 2455–2461, 1 2021.
- [13] P. Mandal, B. K. Hong, J. G. Oh, and S. Litster, “Understanding the voltage reversal behavior of automotive fuel cells,” *Journal of Power Sources*, vol. 397, pp. 397–404, 9 2018.

- [14] H. E. Kim, S. Shin, and H. Lee, "Pt-IrOx catalysts immobilized on defective carbon for efficient reversal tolerant anode in proton exchange membrane fuel cells," *Journal of Catalysis*, vol. 395, pp. 404–411, 3 2021.
- [15] M. Fathi Tovini, A. Hartig-Weiß, H. A. Gasteiger, and H. A. El-Sayed, "The Discrepancy in Oxygen Evolution Reaction Catalyst Lifetime Explained: RDE vs MEA - Dynamicity within the Catalyst Layer Matters," *Journal of The Electrochemical Society*, vol. 168, no. 1, p. 014512, 1 2021.
- [16] A. Hartig-Weiss, M. F. Tovini, H. A. Gasteiger, and H. A. El-Sayed, "OER catalyst durability tests using the rotating disk electrode technique: The reason why this leads to erroneous conclusions," *ACS Applied Energy Materials*, vol. 3, no. 11, pp. 10 323–10 327, 11 2020.
- [17] G. Jerkiewicz, "Standard and Reversible Hydrogen Electrodes: Theory, Design, Operation, and Applications," *ACS Catalysis*, vol. 10, no. 15, pp. 8409–8417, 2020. [Online]. Available: <https://doi.org/10.1021/acscatal.0c02046>
- [18] Y. Shiraishi and T. Hirai, "Selective organic transformations on titanium oxide-based photocatalysts," pp. 157–170, 12 2008.
- [19] G. Tsotridis, A. Pilenga, G. De Marco, and T. Malkow, "EU HARMONISED TEST PROTOCOLS FOR PEMFC MEA TESTING IN SINGLE CELL CONFIGURATION FOR AUTOMOTIVE APPLICATIONS," 2015. [Online]. Available: <https://ec.europa.eu/jrc>
- [20] R. A. Meyers, T. E. Lipman, and A. Z. Weber, "Encyclopedia of Sustainability Science and Technology Series Editor-in-Chief: Fuel Cells and Hydrogen Production A Volume in the Encyclopedia of Sustainability Science and Technology, Second Edition," Tech. Rep. [Online]. Available: <https://link.springer.com/bookseries/15436>
- [21] A. Riese, D. Banham, S. Ye, and X. Sun, "Accelerated Stress Testing by Rotating Disk Electrode for Carbon Corrosion in Fuel Cell Catalyst Supports," *Journal of The Electrochemical Society*, vol. 162, no. 7, pp. F783–F788, 2015.
- [22] S. G. Kandlikar and Z. Lu, "Thermal management issues in a PEMFC stack – A brief review of current status," *Applied Thermal Engineering*, vol. 29, no. 7, pp. 1276–1280, 2009. [Online]. Available: <https://www.sciencedirect.com/science/article/pii/S1359431108002251>
- [23] V. Mehta and J. S. Cooper, "Review and analysis of PEM fuel cell design and manufacturing," pp. 32–53, 2 2003.
- [24] S. Kandlikar, Z. Lu, Z. Edu, and T. Trabold, "Current status and fundamental research needs in thermal management within a PEMFC stack," 5 2021.
- [25] M. H. S. Bargal, M. A. A. Abdelkareem, Q. Tao, J. Li, J. Shi, and Y. Wang, "Liquid cooling techniques in proton exchange membrane fuel cell stacks: A detailed survey," *Alexandria Engineering Journal*, vol. 59, no. 2, pp. 635–655, 2020. [Online]. Available: <https://www.sciencedirect.com/science/article/pii/S1110016820300600>
- [26] J. Zhang, *PEM fuel cell electrocatalysts and catalyst layers: Fundamentals and applications*. Springer London, 2008.
- [27] G. J. M. de Bruijn A. Frank }and Janssen, "PEM Fuel Cell Materials: Costs, Performance and Durability," in *Encyclopedia of Sustainability Science and Technology*, R. A. Meyers, Ed. New York, NY: Springer New York, 2012, pp. 7694–7730. [Online]. Available: [https://doi.org/10.1007/978-1-4419-0851-3\\_152](https://doi.org/10.1007/978-1-4419-0851-3_152)
- [28] J. Walkowiak-Kulikowska, J. Wolska, and H. Koroniak, "Polymers application in proton exchange membranes for fuel cells (PEMFCs)," 8 2017.
- [29] A. Ozden, I. E. Alaefour, S. Shahgaldi, X. Li, C. Ozgur Colpan, and F. Hamdullahpur, "Chapter 2.28 - Gas Diffusion Layers for PEM Fuel Cells: Ex- and In-Situ Characterization," in *Exergetic, Energetic and Environmental Dimensions*, I. Dincer, C. O. Colpan, and O. Kizilkan, Eds. Academic Press, 2018, pp. 695–727. [Online]. Available: <https://www.sciencedirect.com/science/article/pii/B9780128137345000408>

- [30] A. Suzuki, U. Sen, T. Hattori, R. Miura, R. Nagumo, H. Tsuboi, N. Hatakeyama, A. Endou, H. Takaba, M. C. Williams, and A. Miyamoto, "Ionomer content in the catalyst layer of polymer electrolyte membrane fuel cell (PEMFC): Effects on diffusion and performance," *International Journal of Hydrogen Energy*, vol. 36, no. 3, pp. 2221–2229, 2011. [Online]. Available: <https://www.sciencedirect.com/science/article/pii/S0360319910022913>
- [31] T. Schuler, A. Chowdhury, A. T. Freiberg, B. Sneed, F. B. Spingler, M. C. Tucker, K. L. More, C. J. Radke, and A. Z. Weber, "Fuel-Cell Catalyst-Layer Resistance via Hydrogen Limiting-Current Measurements," *Journal of The Electrochemical Society*, vol. 166, no. 7, pp. F3020–F3031, 2019.
- [32] C.-Y. Ahn, J. Ahn, S. Y. Kang, O.-H. Kim, D. W. Lee, J. H. Lee, J. G. Shim, C. H. Lee, Y.-H. Cho, and Y.-E. Sung, "Enhancement of service life of polymer electrolyte fuel cells through application of nanodispersed ionomer," *Science Advances*, vol. 6, no. 5, 2020. [Online]. Available: <https://advances.sciencemag.org/content/6/5/eaaw0870>
- [33] G. Hoogers, *Chapter 6 - Fuel cell technology handbook*. CRC Press, 2003.
- [34] R. O'Hayre, S.-W. Cha, W. Colella, and F. Prinz, "Chapter 3: Fuel Cell Reaction Kinetics," in *Fuel Cell Fundamentals*. John Wiley & Sons, Ltd, 2016, ch. 3, pp. 77–116. [Online]. Available: <https://onlinelibrary.wiley.com/doi/abs/10.1002/9781119191766.ch3>
- [35] J. X. Wang, T. E. Springer, P. Liu, M. Shao, and R. R. Adzic, "Hydrogen Oxidation Reaction on Pt in Acidic Media: Adsorption Isotherm and Activation Free Energies," *The Journal of Physical Chemistry C*, vol. 111, no. 33, pp. 12 425–12 433, 2007. [Online]. Available: <https://doi.org/10.1021/jp073400i>
- [36] W. Schmickler and E. Santos, *Interfacial Electrochemistry*, 2nd ed.
- [37] N. M. Marković and P. N. Ross, "Surface science studies of model fuel cell electrocatalysts," *Surface Science Reports*, vol. 45, no. 4, pp. 117–229, 2002. [Online]. Available: <https://www.sciencedirect.com/science/article/pii/S016757290100022X>
- [38] I. C. Man, H.-Y. Su, F. Calle-Vallejo, H. A. Hansen, J. I. Martínez, N. G. Inoglu, J. Kitchin, T. F. Jaramillo, J. K. Nørskov, and J. Rossmeisl, "Universality in Oxygen Evolution Electrocatalysis on Oxide Surfaces," *ChemCatChem*, vol. 3, no. 7, pp. 1159–1165, 2011. [Online]. Available: <https://chemistry-europe.onlinelibrary.wiley.com/doi/abs/10.1002/cctc.201000397>
- [39] R. Paul, D. Zemlyanov, A. K. Roy, and A. A. Voevodin, "Chapter 3 - Characterization techniques and analytical methods of carbon-based materials for energy applications," in *Carbon Based Nanomaterials for Advanced Thermal and Electrochemical Energy Storage and Conversion*, ser. Micro and Nano Technologies, R. Paul, V. Etacheri, Y. Wang, and C.-T. Lin, Eds. Elsevier, 2019, pp. 63–88. [Online]. Available: <https://www.sciencedirect.com/science/article/pii/B9780128140833000032>
- [40] S. Shiva Kumar and V. Himabindu, "Hydrogen production by PEM water electrolysis – A review," *Materials Science for Energy Technologies*, vol. 2, no. 3, pp. 442–454, 2019. [Online]. Available: <https://www.sciencedirect.com/science/article/pii/S2589299119300035>
- [41] T. Reier, H. N. Nong, D. Teschner, R. Schlögl, and P. Strasser, "Electrocatalytic Oxygen Evolution Reaction in Acidic Environments – Reaction Mechanisms and Catalysts," 1 2017.
- [42] Z. Shi, X. Wang, J. Ge, C. Liu, and W. Xing, "Fundamental understanding of the acidic oxygen evolution reaction: Mechanism study and state-of-the-art catalysts," pp. 13 249–13 275, 7 2020.
- [43] J. Rossmeisl, A. Logadottir, and J. K. Nørskov, "Electrolysis of water on (oxidized) metal surfaces," *Chemical Physics*, vol. 319, no. 1, pp. 178–184, 2005. [Online]. Available: <https://www.sciencedirect.com/science/article/pii/S0301010405002053>
- [44] C. F. Dickens and J. K. Nørskov, "A Theoretical Investigation into the Role of Surface Defects for Oxygen Evolution on RuO<sub>2</sub>," *Journal of Physical Chemistry C*, vol. 121, no. 34, pp. 18 516–18 524, 8 2017.

- [45] X. K. Gu, J. C. A. Camayang, S. Samira, and E. Nikolla, "Oxygen evolution electrocatalysis using mixed metal oxides under acidic conditions: Challenges and opportunities," pp. 130–140, 8 2020.
- [46] A. Grimaud, O. Diaz-Morales, B. Han, W. T. Hong, Y. L. Lee, L. Giordano, K. A. Stoerzinger, M. T. Koper, and Y. Shao-Horn, "Activating lattice oxygen redox reactions in metal oxides to catalyse oxygen evolution," *Nature Chemistry*, vol. 9, no. 5, pp. 457–465, 5 2017.
- [47] H. Y. Qu, X. He, Y. Wang, and S. Hou, "Electrocatalysis for the oxygen evolution reaction in acidic media: Progress and challenges," *Applied Sciences (Switzerland)*, vol. 11, no. 10, 5 2021.
- [48] K. G. Gallagher and T. F. Fuller, "Kinetic model of the electrochemical oxidation of graphitic carbon in acidic environments," *Physical Chemistry Chemical Physics*, vol. 11, no. 48, pp. 11 557–11 567, 2009.
- [49] J. J. Baschuk and X. Li, "Carbon monoxide poisoning of proton exchange membrane fuel cells," *International Journal of Energy Research*, vol. 25, no. 8, pp. 695–713, 6 2001.
- [50] D. A. Stevens, M. T. Hicks, G. M. Haugen, and J. R. Dahn, "Ex Situ and In Situ Stability Studies of PEMFC Catalysts," *Journal of The Electrochemical Society*, vol. 152, no. 12, p. A2309, 2005.
- [51] F. N. Büchi, T. J. Schmidt, and M. Inaba, *Polymer electrolyte fuel cell durability*. Springer New York, 2009.
- [52] A. Pandey, Z. Yang, M. Gummalla, V. V. Atrazhev, N. Y. Kuzminykh, V. I. Sultanov, and S. Burlatsky, "A Carbon Corrosion Model to Evaluate the Effect of Steady State and Transient Operation of a Polymer Electrolyte Membrane Fuel Cell," *Journal of The Electrochemical Society*, vol. 160, no. 9, pp. F972–F979, 2013.
- [53] A. Taniguchi, T. Akita, K. Yasuda, and Y. Miyazaki, "Analysis of degradation in PEMFC caused by cell reversal during air starvation," *International Journal of Hydrogen Energy*, vol. 33, no. 9, pp. 2323–2329, 5 2008.
- [54] M. Bodner, A. Schenk, D. Salaberger, M. Rami, C. Hochenauer, and V. Hacker, "Air Starvation Induced Degradation in Polymer Electrolyte Fuel Cells," *Fuel Cells*, vol. 17, no. 1, pp. 18–26, 2 2017.
- [55] R. Schweiss, "Benefits of Membrane Electrode Assemblies with Asymmetrical GDL Configurations for PEM Fuel Cells," *Fuel Cells*, vol. 16, no. 1, pp. 100–106, 2 2016.
- [56] J. T. Pukrushpan, A. G. Stefanopoulou, and H. Peng, "Control of fuel cell breathing," *IEEE Control Systems Magazine*, vol. 24, no. 2, pp. 30–46, 2004.
- [57] B. Randrianarizafy, P. Schott, M. Gerard, and Y. Bultel, "Modelling carbon Corrosion during a PEMFC startup: Simulation of mitigation strategies," *Energies*, vol. 13, no. 9, 5 2020.
- [58] C. A. Reiser, L. Bregoli, T. W. Patterson, J. S. Yi, J. D. Yang, M. L. Perry, and T. D. Jarvi, "A reverse-current decay mechanism for fuel cells," *Electrochemical and Solid-State Letters*, vol. 8, no. 6, 2005.
- [59] B. K. Hong, P. Mandal, J. G. Oh, and S. Litster, "On the impact of water activity on reversal tolerant fuel cell anode performance and durability," *Journal of Power Sources*, vol. 328, pp. 280–288, 10 2016.
- [60] Z. Liu, L. Yang, Z. Mao, W. Zhuge, Y. Zhang, and L. Wang, "Behavior of PEMFC in starvation," *Journal of Power Sources*, vol. 157, no. 1, pp. 166–176, 2006. [Online]. Available: <https://www.sciencedirect.com/science/article/pii/S037877530501089X>
- [61] A. Taniguchi, T. Akita, K. Yasuda, and Y. Miyazaki, "Analysis of electrocatalyst degradation in PEMFC caused by cell reversal during fuel starvation," *Journal of Power Sources*, vol. 130, no. 1-2, pp. 42–49, 5 2004.

- [62] S. Maass, F. Finsterwalder, G. Frank, R. Hartmann, and C. Merten, “Carbon support oxidation in PEM fuel cell cathodes,” *Journal of Power Sources*, vol. 176, no. 2, pp. 444–451, 2008. [Online]. Available: <https://www.sciencedirect.com/science/article/pii/S0378775307016084>
- [63] L. M. Roen, C. H. Paik, and T. D. Jarvi, “Electrocatalytic Corrosion of Carbon Support in PEMFC Cathodes,” *Electrochemical and Solid-State Letters*, vol. 7, no. 1, 2004.
- [64] N. Macauley, D. D. Papadias, J. Fairweather, D. Spornjak, D. Langlois, R. Ahluwalia, K. L. More, R. Mukundan, and R. L. Borup, “Carbon Corrosion in PEM Fuel Cells and the Development of Accelerated Stress Tests,” *Journal of The Electrochemical Society*, vol. 165, no. 6, pp. F3148–F3160, 2018.
- [65] P. Kanninen, B. Eriksson, F. Davodi, M. E. M. Buan, O. Sorsa, T. Kallio, and R. W. Lindström, “Carbon corrosion properties and performance of multi-walled carbon nanotube support with and without nitrogen-functionalization in fuel cell electrodes,” *Electrochimica Acta*, vol. 332, 2 2020.
- [66] R. N. Carter, W. Gu, B. Brady, P. T. Yu, K. Subramanian, and H. A. Gasteiger, “Electrode degradation mechanisms studies by current distribution measurements,” in *Handbook of Fuel Cells*. American Cancer Society, 2010. [Online]. Available: <https://onlinelibrary.wiley.com/doi/abs/10.1002/9780470974001.f500055>
- [67] X. Zhang, Y. Yang, L. Guo, and H. Liu, “Effects of carbon corrosion on mass transfer losses in proton exchange membrane fuel cells,” *International Journal of Hydrogen Energy*, vol. 42, no. 7, pp. 4699–4705, 2017. [Online]. Available: <https://www.sciencedirect.com/science/article/pii/S0360319916310138>
- [68] K. H. Lim, W. H. Lee, Y. Jeong, and H. Kim, “Analysis of Carbon Corrosion in Anode under Fuel Starvation Using On-Line Mass Spectrometry in Polymer Electrolyte Membrane Fuel Cells,” *Journal of The Electrochemical Society*, vol. 164, no. 14, pp. F1580–F1586, 2017.
- [69] J. Durst, A. Lamibrac, F. Charlot, J. Dillet, L. F. Castanheira, G. Maranzana, L. Dubau, F. Maillard, M. Chatenet, and O. Lottin, “Degradation heterogeneities induced by repetitive start/stop events in proton exchange membrane fuel cell: Inlet vs. outlet and channel vs. land,” *Applied Catalysis B: Environmental*, vol. 138–139, pp. 416–426, 2013. [Online]. Available: <https://www.sciencedirect.com/science/article/pii/S092633731300180X>
- [70] K. H. Kangasniemi, D. A. Condit, and T. D. Jarvi, “Characterization of Vulcan Electrochemically Oxidized under Simulated PEM Fuel Cell Conditions,” *Journal of The Electrochemical Society*, vol. 151, no. 4, p. E125, 2004.
- [71] M. L. Perry, T. Patterson, and C. Reiser, “Systems Strategies to Mitigate Carbon Corrosion in Fuel Cells,” *ECS Transactions*, vol. 3, no. 1, pp. 783–795, 12 2019.
- [72] W. R. W. Daud, R. E. Rosli, E. H. Majlan, S. A. A. Hamid, R. Mohamed, and T. Husaini, “PEM fuel cell system control: A review,” *Renewable Energy*, vol. 113, pp. 620–638, 2017. [Online]. Available: <https://www.sciencedirect.com/science/article/pii/S0960148117305281>
- [73] C. Pak, S. W. Lee, C. Baik, B. H. Lee, D. J. You, and E. You, “New strategy for reversal tolerant anode for automotive polymer electrolyte fuel cell,” *Chinese Chemical Letters*, vol. 30, no. 6, pp. 1186–1189, 6 2019.
- [74] X. Zhou, H. Ji, B. Li, and C. Zhang, “High-Repetitive Reversal Tolerant Performance of Proton-Exchange Membrane Fuel Cell by Designing a Suitable Anode,” *ACS Omega*, vol. 5, no. 17, pp. 10 099–10 105, 5 2020.
- [75] T. Joo, L. Hu, B. K. Hong, J. G. Oh, and S. Litster, “On the origin of deactivation of reversal-tolerant fuel cell anodes under voltage reversal conditions,” *Journal of Power Sources*, vol. 472, 10 2020.
- [76] Q. Yuan, C. T. Lin, and K. W. Chee, “All-carbon devices based on sp<sup>2</sup>-on-sp<sup>3</sup> configuration,” *APL Materials*, vol. 7, no. 3, 3 2019.

- [77] E. H. Falcao and F. Wudl, “Carbon allotropes: Beyond graphite and diamond,” pp. 524–531, 6 2007.
- [78] M. Noked, A. Soffer, and D. Arubach, “The electrochemistry of activated carbonaceous materials: Past, present, and future,” pp. 1563–1578, 7 2011.
- [79] T. Soboleva, X. Zhao, K. Malek, Z. Xie, T. Navessin, and S. Holdcroft, “On the micro-, meso-, and macroporous structures of polymer electrolyte membrane fuel cell catalyst layers,” *ACS Applied Materials and Interfaces*, vol. 2, no. 2, pp. 375–384, 2 2010.
- [80] Y. Shao, G. Yin, and Y. Gao, “Understanding and approaches for the durability issues of Pt-based catalysts for PEM fuel cell,” pp. 558–566, 9 2007.
- [81] Z. Zhao, L. Dubau, and F. Maillard, “Evidences of the migration of Pt crystallites on high surface area carbon supports in the presence of reducing molecules,” *Journal of Power Sources*, vol. 217, pp. 449–458, 2012. [Online]. Available: <https://www.sciencedirect.com/science/article/pii/S0378775312010051>
- [82] L. Filipe and R. Castanheira, “PhD Thesis: Corrosion of high surface area carbon supports used in proton-exchange membrane fuel cell electrodes,” Tech. Rep., 2016. [Online]. Available: <https://tel.archives-ouvertes.fr/tel-01303814>
- [83] O. V. Cherstiouk, A. N. Simonov, N. S. Moseva, S. V. Cherepanova, P. A. Simonov, V. I. Zaikovskii, and E. R. Savinova, “Microstructure effects on the electrochemical corrosion of carbon materials and carbon-supported Pt catalysts,” *Electrochimica Acta*, vol. 55, no. 28, pp. 8453–8460, 12 2010.
- [84] F. Forouzandeh, X. Li, D. W. Banham, F. Feng, S. Ye, and V. Birss, “Understanding the Corrosion Resistance of Meso- and Micro-Porous Carbons for Application in PEM Fuel Cells,” *Journal of The Electrochemical Society*, vol. 165, no. 6, pp. F3230–F3240, 2018.
- [85] Y. C. Park, H. Tokiwa, K. Kakinuma, M. Watanabe, and M. Uchida, “Effects of carbon supports on Pt distribution, ionomer coverage and cathode performance for polymer electrolyte fuel cells,” *Journal of Power Sources*, vol. 315, pp. 179–191, 5 2016.
- [86] P. K. Mohanta, F. Regnet, and L. Jörissen, “Graphitized Carbon: A promising stable cathode catalyst support material for long term PEMFC applications,” *Materials*, vol. 11, no. 6, 5 2018.
- [87] D. Pantea, H. Darmstadt, S. Kaliaguine, and C. Roy, “Electrical conductivity of conductive carbon blacks: Influence of surface chemistry and topology,” *Applied Surface Science*, vol. 217, no. 1-4, pp. 181–193, 7 2003.
- [88] M. Kawakami, H. Kanba, K. Sato, T. Takenaka, S. Gupta, R. Chandratilleke, and V. Sahajwalla, “Characterization of Thermal Annealing Effects on the Evolution of Coke Carbon Structure Using Raman Spectroscopy and X-ray Diffraction,” *ISIJ International*, vol. 46, no. 8, pp. 1165–1170, 2006.
- [89] T. Soboleva, K. Malek, Z. Xie, T. Navessin, and S. Holdcroft, “PEMFC catalyst layers: The role of micropores and mesopores on water sorption and fuel cell activity,” *ACS Applied Materials and Interfaces*, vol. 3, no. 6, pp. 1827–1837, 6 2011.
- [90] A. Li, S. H. Chan, and N.-t. Nguyen, “Anti-flooding cathode catalyst layer for high performance PEM fuel cell,” *Electrochemistry Communications*, vol. 11, no. 4, pp. 897–900, 2009. [Online]. Available: <https://www.sciencedirect.com/science/article/pii/S1388248109000800>
- [91] K. Jiao, J. Xuan, Q. Du, Z. Bao, B. Xie, B. Wang, Y. Zhao, L. Fan, H. Wang, Z. Hou, S. Huo, N. P. Brandon, Y. Yin, and M. D. Guiver, “Designing the next generation of proton-exchange membrane fuel cells,” pp. 361–369, 7 2021.
- [92] M. L. Studebaker, E. W. D. Huffman, A. C. Wolfe, and L. G. Nabors, “Oxygen-Containing Groups on the Surface of Carbon Black,” *Industrial & Engineering Chemistry*, vol. 48, no. 1, pp. 162–166, 1956. [Online]. Available: <https://doi.org/10.1021/ie50553a044>

- [93] K. Artyushkova, S. Pylypenko, M. Dowlapalli, and P. Atanassov, "Structure-to-property relationships in fuel cell catalyst supports: Correlation of surface chemistry and morphology with oxidation resistance of carbon blacks," *Journal of Power Sources*, vol. 214, pp. 303–313, 9 2012.
- [94] M. Studebaker and C. Snow, "THE INFLUENCE OF ULTIMATE COMPOSITION UPON THE WETTABILITY OF CARBON BLACKS," Phillipc Chemical Company, Ohio, Tech. Rep., 1955. [Online]. Available: <https://pubs.acs.org/sharingguidelines>
- [95] A. AlRatrou, M. J. Blunt, and B. Bijeljic, "Wettability in complex porous materials, the mixed-wet state, and its relationship to surface roughness," *Proceedings of the National Academy of Sciences*, vol. 115, no. 36, pp. 8901–8906, 2018. [Online]. Available: <https://www.pnas.org/content/115/36/8901>
- [96] R. Cucchiella, G. Falini, M. Ferri, M. Stracquadanio, and C. Trombini, "Mathematical form factor studies on the effect of water on airborne particles morphology using a bi-dimensional TEM image processing," *Journal of Environmental Monitoring*, vol. 11, no. 1, pp. 181–186, 2009.
- [97] E. Fabbri, A. Habereeder, K. Waltar, R. Kötz, and T. J. Schmidt, "Developments and perspectives of oxide-based catalysts for the oxygen evolution reaction," pp. 3800–3821, 11 2014.
- [98] J. Feary and P. Cullinan, "Heavy Metals," in *Encyclopedia of Respiratory Medicine (Second Edition)*, second edition ed., S. M. Janes, Ed. Oxford: Academic Press, 2022, pp. 458–469. [Online]. Available: <https://www.sciencedirect.com/science/article/pii/B9780128012383114965>
- [99] I. Jang, I. Hwang, and Y. Tak, "Attenuated degradation of a PEMFC cathode during fuel starvation by using carbon-supported IrO<sub>2</sub>," *Electrochimica Acta*, vol. 90, pp. 148–156, 2013. [Online]. Available: <https://www.sciencedirect.com/science/article/pii/S0013468612019937>
- [100] P. J. Rheinländer and J. Durst, "Transformation of the OER-Active IrO<sub>x</sub> Species under Transient Operation Conditions in PEM Water Electrolysis," *Journal of the Electrochemical Society*, vol. 168, no. 2, p. 024511, 2 2021.
- [101] M. Fathi Tovini, A. M. Damjanovic, H. A. El-Sayed, J. Speder, C. Eickes, J.-P. Suchsland, A. Ghielmi, and H. A. Gasteiger, "Degradation Mechanism of an IrO<sub>2</sub> Anode Co-Catalyst for Cell Voltage Reversal Mitigation under Transient Operation Conditions of a PEM Fuel Cell," *Journal of The Electrochemical Society*, vol. 168, no. 6, p. 064521, 6 2021.
- [102] T. Nagai, C. Jahn, and H. Jia, "Improved Accelerated Stress Tests for ORR Catalysts Using a Rotating Disk Electrode," *Journal of The Electrochemical Society*, vol. 166, no. 7, pp. F3111–F3115, 2019.
- [103] E. Pizzutilo, S. Geiger, J.-P. Grote, A. Mingers, K. J. J. Mayrhofer, M. Arenz, and S. Cherevko, "On the Need of Improved Accelerated Degradation Protocols (ADPs): Examination of Platinum Dissolution and Carbon Corrosion in Half-Cell Tests," *Journal of The Electrochemical Society*, vol. 163, no. 14, pp. F1510–F1514, 2016.
- [104] J. Schmidt, H. A. Gasteiger, G. D. Stab, P. M. Urban, D. M. Koib, and R. J. Behm<sup>o</sup>, "Characterization of High-Surface-Area Electrocatalysts Using a Rotating Disk Electrode Configuration," Tech. Rep. 7, 1998.
- [105] S. S. Kocha, K. Shinozaki, J. W. Zack, D. J. Myers, N. N. Kariuki, T. Nowicki, V. Stamenkovic, Y. Kang, D. Li, and D. Papageorgopoulos, "Best Practices and Testing Protocols for Benchmarking ORR Activities of Fuel Cell Electrocatalysts Using Rotating Disk Electrode," *Electrocatalysis*, vol. 8, no. 4, pp. 366–374, 7 2017.
- [106] U. A. Paulus, T. J. Schmidt, H. A. Gasteiger, and R. J. Behm, "Oxygen reduction on a high-surface area Pt/Vulcan carbon catalyst: a thin-film rotating ring-disk electrode study," *Journal of Electroanalytical Chemistry*, vol. 495, no. 2, pp. 134–145, 2001. [Online]. Available: <https://www.sciencedirect.com/science/article/pii/S0022072800004071>

- [107] H. A. El-Sayed, A. Weiß, L. F. Olbrich, G. P. Putro, and H. A. Gasteiger, “OER Catalyst Stability Investigation Using RDE Technique: A Stability Measure or an Artifact?” *Journal of The Electrochemical Society*, vol. 166, no. 8, pp. F458–F464, 2019.
- [108] Y. A. Gandomi, D. S. Aaron, J. R. Houser, M. C. Daugherty, J. T. Clement, A. M. Pezeshki, T. Y. Ertugrul, D. P. Moseley, and M. M. Mench, “Critical Review—Experimental Diagnostics and Material Characterization Techniques Used on Redox Flow Batteries,” *Journal of The Electrochemical Society*, vol. 165, no. 5, pp. A970–A1010, 2018.
- [109] S. Li and A. Thomas, “Chapter 12 - Emerged carbon nanomaterials from metal-organic precursors for electrochemical catalysis in energy conversion,” in *Advanced Nanomaterials for Electrochemical-Based Energy Conversion and Storage*, ser. Micro and Nano Technologies, F. Ran and S. Chen, Eds. Elsevier, 2020, pp. 393–423. [Online]. Available: <https://www.sciencedirect.com/science/article/pii/B9780128145586000125>
- [110] K. C. Honeychurch, “13 - Printed thick-film biosensors,” in *Printed Films*, ser. Woodhead Publishing Series in Electronic and Optical Materials, M. Prudenziati and J. Hormadaly, Eds. Woodhead Publishing, 2012, pp. 366–409. [Online]. Available: <https://www.sciencedirect.com/science/article/pii/B9781845699888500138>
- [111] S. K. Butti, J. A. Modestra, and S. V. Mohan, “Chapter 5.5 - Regulating Bioelectrochemical CO<sub>2</sub> Sequestration for Platform Chemicals Production,” in *Microbial Electrochemical Technology*, ser. Biomass, Biofuels and Biochemicals, S. V. Mohan, S. Varjani, and A. Pandey, Eds. Elsevier, 2019, pp. 797–824. [Online]. Available: <https://www.sciencedirect.com/science/article/pii/B9780444640529000339>
- [112] EDAQ, “Hydroflex™ Hydrogen Reference Electrode.” [Online]. Available: <https://www.edaq.com/ET070>
- [113] K.R. Cooper, “In Situ PEM FC Electrochemical Surface Area And Catalyst Utilization Measurement - Scribner Associates,” 2017. [Online]. Available: <http://www.scribner.com/faq/1-in-situ-pem-fc-electrochemical-surface-area-and-catalyst-utilization-measurement/>
- [114] S. A. Sheppard, “Electrochemical and microscopic characterisation of platinum-coated perfluoro-sulfonic (Nafion 117) materials,” in *Analyst*, vol. 123, no. 10. Royal Society of Chemistry, 1998, pp. 1923–1929.
- [115] C. Chaiburi and V. Hacker, “Catalytic activity of various platinum loading in acid electrolyte at 303 K,” in *Energy Procedia*, vol. 138. Elsevier Ltd, 2017, pp. 229–234.
- [116] K. J. Mayrhofer, D. Strmcnik, B. B. Blizanac, V. Stamenkovic, M. Arenz, and N. M. Markovic, “Measurement of oxygen reduction activities via the rotating disc electrode method: From Pt model surfaces to carbon-supported high surface area catalysts,” *Electrochimica Acta*, vol. 53, no. 7, pp. 3181–3188, 2 2008.
- [117] A. Kriston, T. Xie, P. Ganesan, and B. N. Popov, “Analysis of the Effect of Pt Loading on Mass and Specific Activity in PEM Fuel Cells,” *Journal of The Electrochemical Society*, vol. 160, no. 4, pp. F406–F412, 2013.
- [118] R. Eden, “ENTEROBACTERIACEAE, COLIFORMS AND E. COLI — Classical and Modern Methods for Detection and Enumeration,” in *Encyclopedia of Food Microbiology (Second Edition)*, second edition ed., C. A. Batt and M. L. Tortorello, Eds. Oxford: Academic Press, 2014, pp. 667–673. [Online]. Available: <https://www.sciencedirect.com/science/article/pii/B9780123847300000975>
- [119] Gamry Instruments, “Basics of Electrochemical Impedance Spectroscopy.” [Online]. Available: <https://www.gamry.com/application-notes/EIS/basics-of-electrochemical-impedance-spectroscopy/>

- [120] S. Touhami, J. Mainka, J. Dillet, S. A. H. Taleb, and O. Lottin, "Transmission Line Impedance Models Considering Oxygen Transport Limitations in Polymer Electrolyte Membrane Fuel Cells," *Journal of The Electrochemical Society*, vol. 166, no. 15, pp. F1209–F1217, 2019.
- [121] J. Kwon, P. Choi, and K. Eom, "A Comparison Study on the Carbon Corrosion Reaction under Saturated and Low Relative Humidity Conditions via Transmission Line Model-Based Electrochemical Impedance Analysis," *Journal of The Electrochemical Society*, vol. 168, no. 6, p. 064515, 6 2021.
- [122] R. Makharia, M. F. Mathias, and D. R. Baker, "Measurement of Catalyst Layer Electrolyte Resistance in PEFCs Using Electrochemical Impedance Spectroscopy," *Journal of The Electrochemical Society*, vol. 152, no. 5, p. A970, 2005.
- [123] S. U. Rawal and M. M. Patel, "Lipid nanoparticulate systems: Modern versatile drug carriers," in *Lipid Nanocarriers for Drug Targeting*. Elsevier, 1 2018, pp. 49–138.
- [124] Malvern Instruments Limited, "A basic guide to particle characterization," 2015. [Online]. Available: [https://www.cif.iastate.edu/sites/default/files/uploads/Other\\_Inst/Particle%20Size/Particle%20Characterization%20Guide.pdf](https://www.cif.iastate.edu/sites/default/files/uploads/Other_Inst/Particle%20Size/Particle%20Characterization%20Guide.pdf)
- [125] H. G. Merkus, "Laser Diffraction," in *Particle Size Measurements: Fundamentals, Practice, Quality*. Dordrecht: Springer Netherlands, 2009, pp. 259–285. [Online]. Available: [https://doi.org/10.1007/978-1-4020-9016-5\\_10](https://doi.org/10.1007/978-1-4020-9016-5_10)
- [126] G. B. de Boer, C. de Weerd, D. Thoenes, and H. W. Goossens, "Laser Diffraction Spectrometry: Fraunhofer Diffraction Versus Mie Scattering," *Particle & Particle Systems Characterization*, vol. 4, no. 1-4, pp. 14–19, 1987.
- [127] A. Canette and R. Briandet, "MICROSCOPY — Confocal Laser Scanning Microscopy," in *Encyclopedia of Food Microbiology (Second Edition)*, second edition ed., C. A. Batt and M. L. Tortorello, Eds. Oxford: Academic Press, 2014, pp. 676–683. [Online]. Available: <https://www.sciencedirect.com/science/article/pii/B9780123847300002147>
- [128] Keyence, "Non-contact Surface Roughness/Profile Measuring Instruments," *Introduction to Roughness*. [Online]. Available: [https://www.keyence.eu/ss/products/microscope/roughness/equipment/line\\_02.jsp](https://www.keyence.eu/ss/products/microscope/roughness/equipment/line_02.jsp)
- [129] Keyence., "What is Surface Roughness?" [Online]. Available: <https://www.keyence.com/ss/products/microscope/roughness/line/>
- [130] V. S. Kulkarni and C. Shaw, "Chapter 11 - Miscellaneous Physical, Chemical, and Microbiological Test Methods," in *Essential Chemistry for Formulators of Semisolid and Liquid Dosages*, V. S. Kulkarni and C. Shaw, Eds. Boston: Academic Press, 2016, pp. 193–221. [Online]. Available: <https://www.sciencedirect.com/science/article/pii/B978012801024200011X>
- [131] O. J. Guy and K.-A. D. Walker, "Chapter 4 - Graphene Functionalization for Biosensor Applications," in *Silicon Carbide Biotechnology (Second Edition)*, second edition ed., S. E. Sadow, Ed. Elsevier, 2016, pp. 85–141. [Online]. Available: <https://www.sciencedirect.com/science/article/pii/B9780128029930000046>
- [132] J. F. Moulder, F. Stickle, William, E. Sobol, Peter, and D. Bomben, Kenneth, *Handbook of X-Ray Photoelectron Spectroscopy*, J. Chastain, Ed. Eden Prairie: Perkin-Elmer Corporation, 10 1992.
- [133] D. G. Brandon and W. D. Kaplan, *Microstructural characterization of materials*. John Wiley, 2008.
- [134] A. G. Fitzgerald, B. E. Storey, and D. Fabian, *Quantitative microbeam analysis*, P. Osborne, Ed. Dundee: The Scottish Universities Summer School in Physics, 1993.
- [135] A. Agrawal and G.-C. Yi, "Chapter Two - Sample pretreatment with graphene materials," in *Analytical Applications of Graphene for Comprehensive Analytical Chemistry*, ser. Comprehensive Analytical Chemistry, C. M. Hussain, Ed. Elsevier, 2020, vol. 91, pp. 21–47. [Online]. Available: <https://www.sciencedirect.com/science/article/pii/S0166526X20300878>

- [136] G. N. Kamau, "Review SURFACE PREPARATION OF GLASSY CARBON ELECTRODES," Tech. Rep., 1988.
- [137] Pine Research, "E5TQ Change Disk RDE Tip." [Online]. Available: <https://pineresearch.com/shop/products/electrodes/rde/e5tq-changedisk/>
- [138] P. Mandal, "Investigation and Mitigation of Degradation in Hydrogen Fuel Cells," Tech. Rep., 2016.
- [139] T. Reier, M. Oezaslan, and P. Strasser, "Electrocatalytic oxygen evolution reaction (OER) on Ru, Ir, and Pt catalysts: A comparative study of nanoparticles and bulk materials," *ACS Catalysis*, vol. 2, no. 8, pp. 1765–1772, 8 2012.
- [140] R. Frydendal, E. A. Paoli, B. P. Knudsen, B. Wickman, P. Malacrida, I. E. Stephens, and I. Chorkendorff, "Benchmarking the Stability of Oxygen Evolution Reaction Catalysts: The Importance of Monitoring Mass Losses," *ChemElectroChem*, vol. 1, no. 12, pp. 2075–2081, 12 2014.
- [141] M. J. Kristo, "Chapter 21 - Nuclear Forensics," in *Handbook of Radioactivity Analysis (Third Edition)*, third edition ed., M. F. L'Annunziata, Ed. Amsterdam: Academic Press, 2012, pp. 1281–1304. [Online]. Available: <https://www.sciencedirect.com/science/article/pii/B9780123848734000219>
- [142] T. Suzuki, S. Okada, and S. Tsushima, "Analysis of Ionomer Distribution and Pt/C Agglomerate Size in Catalyst Layers by Two-Stage Ion-Beam Processing," *Journal of The Electrochemical Society*, vol. 167, no. 12, p. 124513, 1 2020. [Online]. Available: <https://doi.org/10.1149/1945-7111/abad6a>
- [143] K. Malek, T. Mashio, and M. Eikerling, "Microstructure of Catalyst Layers in PEM Fuel Cells Redefined: A Computational Approach," *Electrocatalysis*, vol. 2, no. 2, pp. 141–157, 6 2011.
- [144] T. Mashio, A. Ohma, and T. Tokumasu, "Molecular Dynamics Study of Ionomer Adsorption at a Carbon Surface in Catalyst Ink," *Electrochimica Acta*, vol. 202, pp. 14–23, 2016. [Online]. Available: <https://www.sciencedirect.com/science/article/pii/S0013468616307927>
- [145] K. Malek, M. Eikerling, Q. Wang, T. Navessin, and Z. Liu, "Self-organization in catalyst layers of polymer electrolyte fuel cells," *Journal of Physical Chemistry C*, vol. 111, no. 36, pp. 13 627–13 634, 9 2007.
- [146] G. Wilberg, "The development of a state-of-the-art experimental setup demonstrated by the investigation of fuel cell reactions in alkaline electrolyte," Ph.D. dissertation, TU München, München, 8 2010. [Online]. Available: <https://d-nb.info/1008188883/34>
- [147] D. A. J. Rand and R. Woods, "CYCLIC VOLTAMMETRIC STUDIES ON IRIIDIUM ELECTRODES IN SULPHURIC ACID SOLUTIONS NATURE OF OXYGEN LAYER AND METAL DISSOLUTION," Tech. Rep., 1974.
- [148] R. Sharma, Y. Wang, F. Li, J. Chamier, and S. M. Andersen, "Particle Size-Controlled Growth of Carbon-Supported Platinum Nanoparticles (Pt/C) through Water-Assisted Polyol Synthesis," *ACS Omega*, vol. 4, no. 13, pp. 15 711–15 720, 9 2019.
- [149] J. C. Meier, C. Galeano, I. Katsounaros, A. A. Topalov, A. Kostka, F. Schüth, and K. J. Mayrhofer, "Degradation mechanisms of Pt/C fuel cell catalysts under simulated start-stop conditions," *ACS Catalysis*, vol. 2, no. 5, pp. 832–843, 5 2012.
- [150] Y. V. Yakovlev, Y. V. Lobko, M. Vorokhta, J. Nováková, M. Mazur, I. Matolínová, and V. Matolín, "Ionomer content effect on charge and gas transport in the cathode catalyst layer of proton-exchange membrane fuel cells," *Journal of Power Sources*, vol. 490, p. 229531, 2021. [Online]. Available: <https://www.sciencedirect.com/science/article/pii/S0378775321000793>

- [151] A. D. Modestov, A. V. Kapustin, V. B. Avakov, I. K. Landgraf, and M. R. Tarasevich, “Cathode catalyst layers with ionomer to carbon mass ratios in the range 0–2 studied by electrochemical impedance spectroscopy, cyclic voltammetry, and performance measurements,” *Journal of Power Sources*, vol. 272, pp. 735–742, 2014. [Online]. Available: <https://www.sciencedirect.com/science/article/pii/S0378775314013780>
- [152] V. Parry, G. Berthomé, J.-C. Joud, O. Lemaire, and A. A. Franco, “XPS investigations of the proton exchange membrane fuel cell active layers aging: Characterization of the mitigating role of an anodic CO contamination on cathode degradation,” *Journal of Power Sources*, vol. 196, no. 5, pp. 2530–2538, 2011. [Online]. Available: <https://www.sciencedirect.com/science/article/pii/S0378775310019336>
- [153] G. Beamson and D. R. Briggs, “High Resolution XPS of Organic Polymers: The Scienta ESCA300 Database,” 1992.
- [154] E. N. El Sawy and V. I. Birss, “Nanoengineered Ircore@Ptshell Nanoparticles with Controlled Pt Shell Coverages for Direct Methanol Electro-Oxidation,” *ACS Applied Materials and Interfaces*, vol. 10, no. 4, pp. 3459–3469, 1 2018.
- [155] A. P. Young, J. Stumper, S. Knights, and E. Gyenge, “Ionomer Degradation in Polymer Electrolyte Membrane Fuel Cells,” *Journal of The Electrochemical Society*, vol. 157, no. 3, p. B425, 2010.
- [156] M. K. Kadirov, A. Bosnjakovic, and S. Schlick, “Membrane-derived fluorinated radicals detected by electron spin resonance in UV-irradiated nion and Dow ionomers: Effect of counterions and H<sub>2</sub>O<sub>2</sub>,” *Journal of Physical Chemistry B*, vol. 109, no. 16, pp. 7664–7670, 4 2005.
- [157] P. TengvaJl, I. LundstrCim, L. Sjaqvist, H. Eilwing, and L. Magnus Bjursten, “Titanium-hydrogen peroxide interaction: model studies of the influence of the inflammatory response on titanium implants,” Tech. Rep., 1989.
- [158] C. Walling, “Fenton’s reagent revisited,” *Accounts of Chemical Research*, vol. 8, no. 4, pp. 125–131, 1975. [Online]. Available: <https://doi.org/10.1021/ar50088a003>
- [159] L. Giordano, B. Han, M. Risch, W. T. Hong, R. R. Rao, K. A. Stoerzinger, and Y. Shao-Horn, “pH dependence of OER activity of oxides: Current and future perspectives,” *Catalysis Today*, vol. 262, pp. 2–10, 2016. [Online]. Available: <https://www.sciencedirect.com/science/article/pii/S0920586115006227>
- [160] J. Knöppel, M. Möckl, D. Escalera-López, K. Stojanovski, M. Bierling, T. Böhm, S. Thiele, M. Rzepka, and S. Cherevko, “On the limitations in assessing stability of oxygen evolution catalysts using aqueous model electrochemical cells,” *Nature Communications*, vol. 12, no. 1, 12 2021.
- [161] P. Jovanovič, N. Hodnik, F. Ruiz-Zepeda, I. Arčon, B. Jozinović, M. Zorko, M. Bele, M. Šala, V. S. Šelih, S. Hočevar, and M. Gaberšček, “Electrochemical Dissolution of Iridium and Iridium Oxide Particles in Acidic Media: Transmission Electron Microscopy, Electrochemical Flow Cell Coupled to Inductively Coupled Plasma Mass Spectrometry, and X-ray Absorption Spectroscopy Study,” *Journal of the American Chemical Society*, vol. 139, no. 36, pp. 12 837–12 846, 9 2017.
- [162] T. Kadyk, D. Bruce, and M. Eikerling, “How to Enhance Gas Removal from Porous Electrodes?” *Scientific Reports*, vol. 6, 12 2016.